The transformation behaviour and hot strength of 3CR12 during the continuous casting process

_____

by

Charles Witness Siyasiya

Submitted in partial fulfilment of the requirements for the degree

MASTER OF SCIENCE (METALLURGY)

in the

Faculty of Engineering, Built Environment and Information Technology

University of Pretoria

1 November 2004

University of Pretoria – Siyasiya C. W. (2004)

SUMMARY

THE TRANSFORMATION BEHAVIOUR AND HOT STRENGTH OF 3CR12 DURING THE CONTINUOUS CASTING PROCESS

_____

Charles Siyasiya

Supervisor: Professor Waldo. E. Stumpf

Department: Materials Science and Metallurgical Engineering

University: University of Pretoria

Degree: Master of Science (Metallurgy)

Extensive research has been done over the years and has contributed quite a lot to the development of 3CR12 stainless steel. Nevertheless, there is still much to be understood about the behaviour of this steel during its production. One of the problems that are occasionally encountered is the side bulging effect i.e. the unconstrained narrow faces of the strand plastically bulge due to ferrostatic pressure from the liquid core of the strand at high temperatures. In general, this problem is prevalent in ferritic stainless steels as they exhibit a weaker hot strength than austenitic stainless steels. Coupled with side bulging, there is also strand width variation at high temperatures i.e. when the steel is in the ferrite-austenite dual phase region. Both of these dimensional changes to the slab profile create some processing problems in subsequent hot rolling operations when unacceptable width variations are encountered.

This work was, therefore, motivated by the requirement to quantify the role that the metallurgical behaviour of this steel plays with regard to the above width variation problem. The research work involved studies of the δ-ferrite to austenite phase change during continuous cooling (simulating cooling during continuous casting) and the establishment of CCT diagrams, the influence of

University of Pretoria – Siyasiya C. W. (2004)

chemical composition on the austenite start temperature and the hot ductility and hot strength vis-à-vis the side bulging effect.

The casting conditions in the mould are crucial to ensure that the solidification shell is thick enough to withstand the ferrostatic pressure exerted on the unconstrained narrow sides of the strand as it exits from the mould. Therefore, part of the solution lies in the study of the optimisation of the cooling rate, mould flux properties, casting speed, mould taper angle and the chemical composition of this steel, among other factors. Additions of austenite formers, within the specification range of 3CR12, should be favourable for a stronger solidification shell since austenite exhibits superior hot strength to δ-ferrite. The good hot ductility observed in 3CR12 may also provide a leeway for increasing the secondary cooling rate in order to form a thicker solidification shell soon after emerging from the mould. This may reduce the side bulging effect. This can be achieved without a risk of transverse cracking if the cooling is adjusted carefully.

As long as the δ-ferrite to austenite phase ratio keeps fluctuating due to variations in (i) the chemical composition within the specification range and (ii) the cooling rate in the dual phase region from cast to cast, the strand width variation effect will persist. This is simply because of the effect these have on the ferrite to austenite phase ratios through the differences between the lattice structures of these two phases. Ferrite being less dense than austenite, occupies more volume than austenite, thereby affecting the slab width. The remedy to this problem is to control within stricter chemical composition limits in order to reduce or completely avert this width variation effect.

Key words: side bulging, width variation effect, resistance bending moment, applied bending moment, ferrostatic pressure.

ACKNOWLEDGEMENT
_____

Firstly, I would like to thank God for affording me the opportunity to study for this degree.

I would like to express my sincere gratitude to Professor Waldo E. Stumpf for his dedication and enthusiasm in supervising this project. I valued his words of encouragement when the going got tough.

I would like also to extend my appreciation for the valuable contribution from Professor Gerrit T. van Rooyen. His vast experience made life easier in setting up the experiments.

I would like to acknowledge the cooperation, sponsorship, provision of materials and relevant data from Columbus Stainless.

I would like to extend my gratitude to the IMMRI staff, in particular Mr Francois Verdoorn, for the training and guidance during laboratory work.

Finally I would like to thank the University of Pretoria, in particular the Materials Science and Metallurgical Engineering Department for the provision of facilities that made it possible for me to complete my studies successfully.

University of Pretoria – Siyasiya C. W. (2004)

TABLE OF CONTENTS
_____

University of Pretoria – Siyasiya C. W. (2004)
TABLE OF CONTENTS
_____

University of Pretoria – Siyasiya C. W. (2004)
TABLE OF CONTENTS
_____

Chapter 1

The phase changes in 3CR12 and the measuring techniques

_____

1   The high temperature phase change of 3CR12 steel

1.1 Introduction

The 3CR12 steel is a corrosion resistant martensite-ferrite dual phase steel. The dual martensite-ferrite microstructure is achieved through the correct balance between austenite-forming and ferrite-forming elements. The actual proportion of ferrite to martensite is dependent on the chemical composition and the heat treatment. The fine grain size is achieved through the impediment to growth of one phase by the other, thus, unlike in fully ferritic or austenitic steels where one phase is maintained throughout the heat treatment. Hence, 3CR12 has good mechanical properties at room temperature, both in terms of yield strength and Charpy toughness i.e. 376 MPa and 85 J respectively.

There are two variants of 3CR12 steel, the low Ti (0.03% maximum) and the high Ti (0.6% maximum) stabilised variant designated type 412. The titanium stabilisation is intended for improvement in weldability. This study focuses on the low titanium 3CR12 steel.

3CR12 steel serves as a cost-effective alternative to mild steel in certain applications because of its better corrosion resistance yet it is cheaper than fully austenitic stainless steels. Hence, it has successfully been applied in autoclave trolleys in the brick making industry, electrical transmission masts and in abrasive-corrosive low-stress applications in the mining and mineral processing industry. Therefore, its importance need not be emphasised.

3CR12 is included in the international specifications and is designated as DIN type 1.4003, ASTM/ASME 41003, and EN 10088/EN 10028.

1.2 The Phase Transformation of δ-ferrite to austenite in 3CR12 steel

To begin with, the Fe-Cr phase diagram is given in figure 1.1 below. From this phase diagram, it is evident that the 11-12%Cr steels exist in the ferrite-austenite dual phase area at temperatures between 850°C and 1200°C.

University of Pretoria – Siyasiya C. W. (2004)
The phase changes in 3CR12 and the measuring techniques
_____
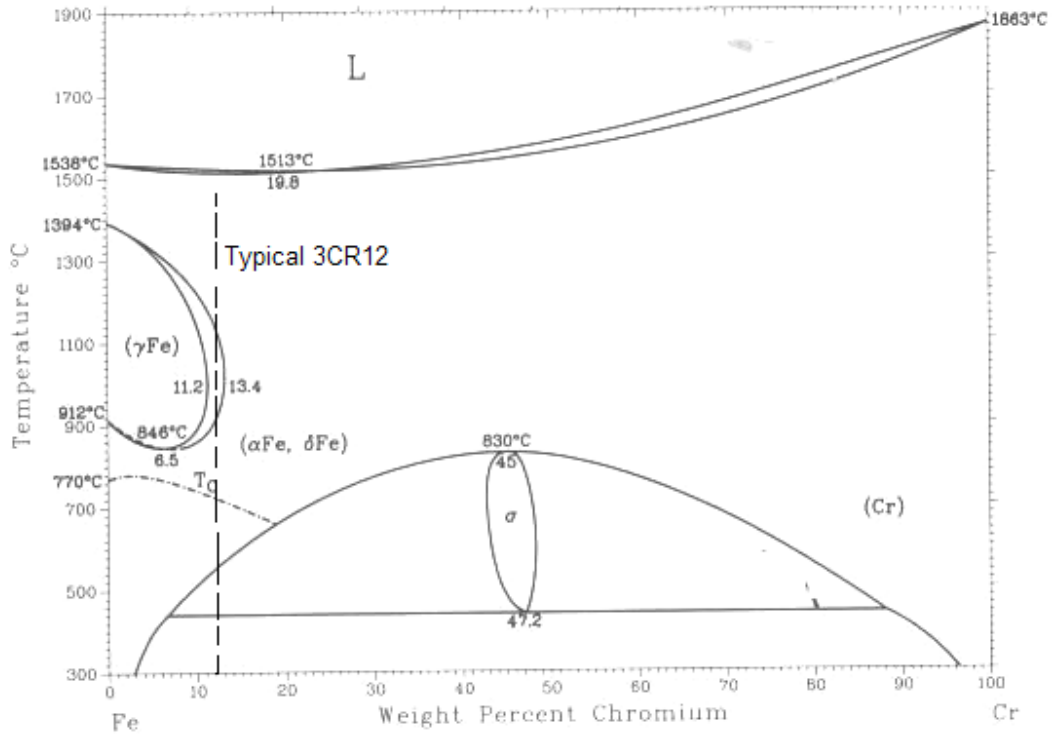
Figure 1.1 - The Fe-Cr binary phase diagram[1]

The addition of austenite formers particularly C, N, Mn and Ni enlarge the γ-loop, raise the δ-ferrite to austenite transformation temperature and extend the (δ+γ) dual phase area to higher chromium levels as shown in figure 1.2 below.

The chemical composition of 3CR12 falls within the range of 11-12%Cr and, therefore, it exists in the ferrite-austenite dual phase area at temperatures between 850°C and 1200°C and the ferrite-martensite area at room temperature. The proportion of ferrite to martensite present at room temperature is dependent on the cooling rate and chemical composition during the decomposition of austenite. The chemical composition specification for 3CR12 steel is given in table 1 below.

University of Pretoria – Siyasiya C. W. (2004)
The phase changes in 3CR12 and the measuring techniques

_____
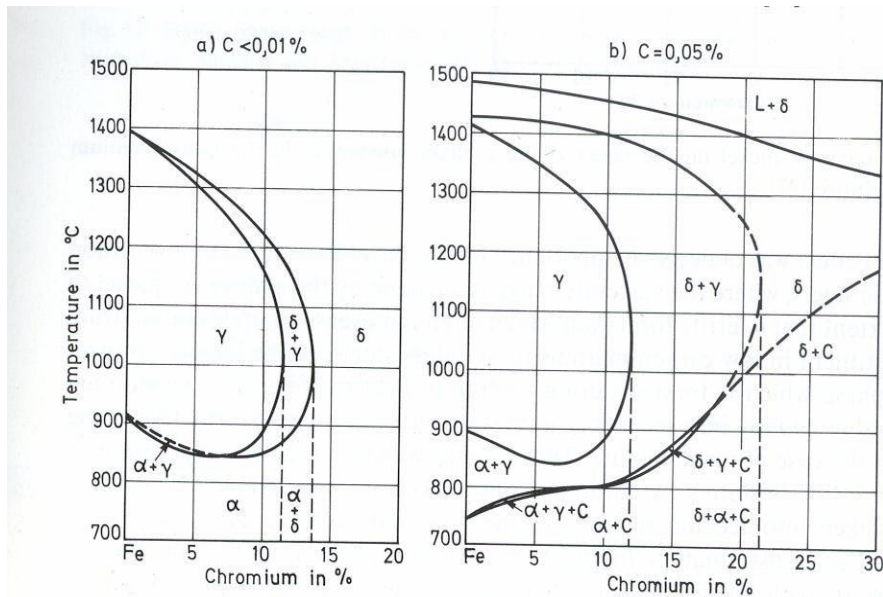
Figure 1.2 - Shifting of the $(\delta+\gamma)/\ \delta$ boundary in the Fe-Cr system through increasing additions of carbon[2]

C	N	Ni	Mn	Cr	Si	Ti	S	P
0.03 max	0.03 max	0.3-1.0	1.50 max	10.5-12.5	1.0 max	0.6 max	0.015 max	0.04 max

Table 1.1 - The chemical composition specification for 3CR12 steel[3]

In a study on the decomposition of austenite in 3CR12 steel[4], it was observed that if the cooling rate is typically as slow as 1 ˚C/min or less, the austenite transforms fully to ferrite plus carbides, without any martensite. At cooling rates greater than 60 °C/min, the austenite transforms fully to martensite. At intermediate cooling rates (greater than 1 ˚C/min and less than 60 ˚C/min), the austenite transforms to martensite and ferrite plus carbides. The ratio of ferrite to martensite depends on the cooling rate. A typical CCT diagram for the austenite decomposition is shown in figure 1.3 below.

_____
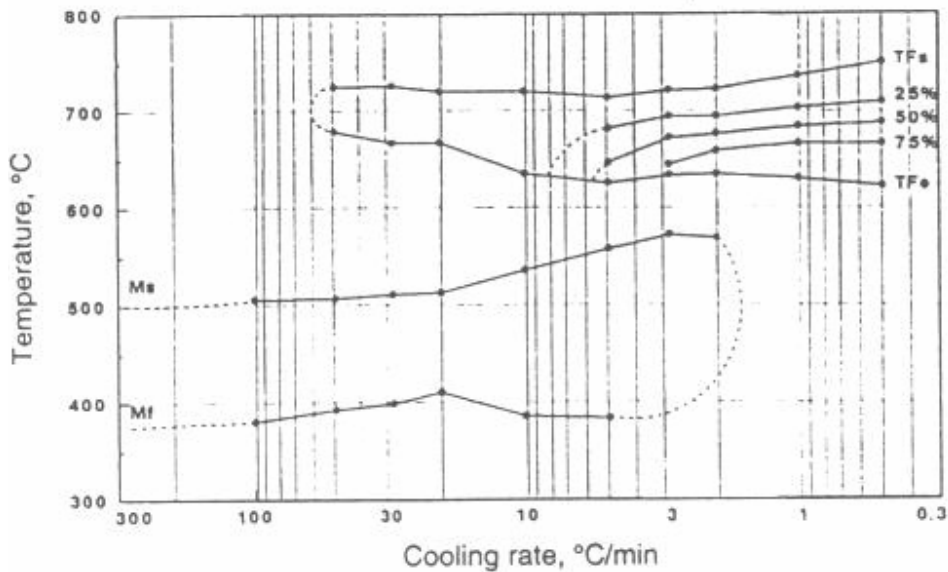
Figure1.3 - The CCT diagram for the austenite decomposition of 3CR12, the top set: austenite to ferrite and the bottom: austenite to martensite[4]

In a similar study on the titanium stabilised 3CR12 with the following chemical composition: Fe-0.024%C-0.53%Si-1.19%Mn-11.12%Cr-0.67%Ni-0.011%N-0.31%Ti-0.015%S, Ball et al[5] observed that for temperatures below 700°C during isothermal transformation, austenite transformed fully to ferrite plus carbides at longer times i.e. for times greater than 14 hours and the ferrite grew epitaxially on the pre-existing δ-ferrite. At intermediate isothermal transformation times, the final microstructure was martensite and ferrite plus inter-phase precipitation of carbides and the volume fraction of ferrite increased with time. No isothermal transformation was observed between 800°C and 1100°C, irrespective of the time the specimen was held at this temperature range, i.e. the proportion of ferrite to austenite only varied with temperature. It was also observed that at equilibrium, the maximum volume fraction of austenite, which is 0.92, occurs at 1050 °C in this steel. Above and below 1050 ˚C, the amount of δ-ferrite and α-ferrite increased with an increase and decrease in temperature respectively. Figure 1.4 below summarises the isothermal decomposition of austenite to martensite and ferrite plus carbides in 3CR12 steel.

University of Pretoria – Siyasiya C. W. (2004)
The phase changes in 3CR12 and the measuring techniques
_____
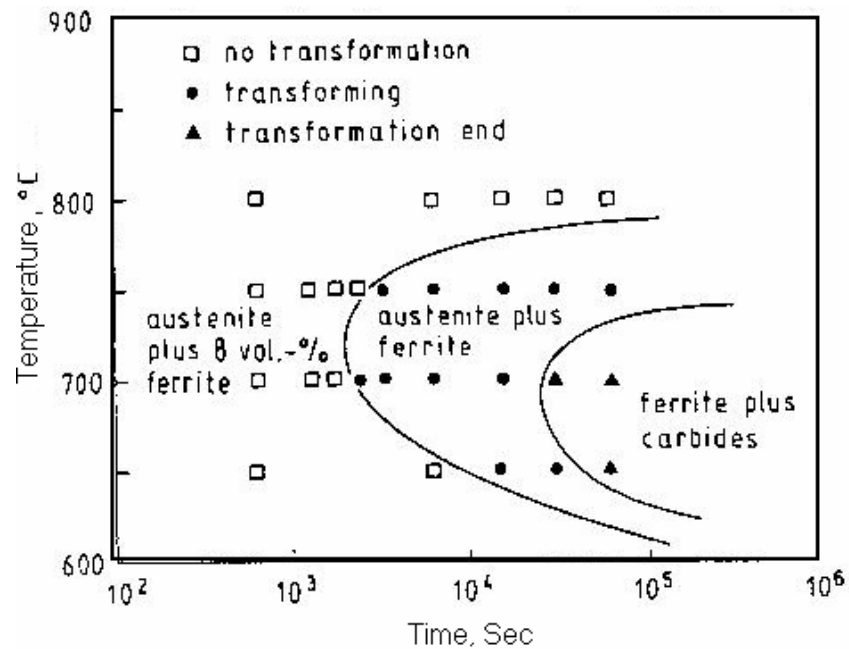
Figure1.4 - Isothermal transformation for the decomposition of austenite to ferrite plus carbides in 3CR12 steel[5]

It was also observed that the α-ferrite growth was identified by a planar migration of the δ-ferrite/austenite interface into the austenite phase. Direct nucleation of the new α-ferrite phase on austenite-austenite grain boundaries was not observed. Pistorius et al[6] observed the nucleation and nascent growth of α-ferrite during an isothermal decomposition of austenite in low titanium 3CR12 steels, whereas in the titanium-stabilised 3CR12, the dominant mechanism was the growth of α-ferrite from pre-existing δ-ferrite. This was ascribed to the higher volume fraction of the δ-ferrite in the titanium-stabilised 3CR12 than in the low titanium steels, due to titanium being a ferrite stabiliser. The growth of α-ferrite from pre-existing δ-ferrite is explained by the classical nucleation theory that a greater driving force is required to homogeneously nucleate a new grain than through heterogeneous nucleation on the existing one epitaxially i.e. the nascent α-ferrite grows heterogeneously from the pre-existing δ-ferrite.

In a study on the influence of compositional banding on grain anisotropy in 3CR12 steel, Knutsen[7] observed that continuous furnace cooling from a 1380 °C solution treatment down

University of Pretoria – Siyasiya C. W. (2004)
The phase changes in 3CR12 and the measuring techniques
_____

to 25 °C, led to partial regression of the austenite to α-ferrite. It was also found that the main ferrite former chromium, partitioned to the δ-ferrite, i.e. the first δ-ferrite to solidify was rich in chromium and, therefore, remained stable all the way to ambient temperature during the heat treatment. Using energy dispersive spectroscopy (EDS) in a scanning electron microscope (SEM), Prozzi[9] found the chromium content to be 2% higher in the δ-ferrite than in the austenite i.e. 13.5%   and 11.5% (±0.5%) respectively. The austenite forming elements (nickel and manganese) partitioned to the transformed austenite, which formed from the δ-ferrite with a nominal composition of chromium.

In a similar study done by Jungbacke[8] on the same 3CR12, it was proven that pre-existing δ-ferrite accelerates the α-ferrite transformation i.e. the new ferrite grows epitaxially from the pre-existing δ-ferrite into the austenite. The study revealed that an increase of 1% in the volume fraction of δ-ferrite results in an increase of 5% in the final ferrite content at constant cooling rate. This suggests that the volume fraction of the pre-existing δ-ferrite influences the final (room temperature) microstructure (martensite to ferrite ratio) of 3CR12 steel.

Previous work in the study of 3CR12 steels concentrated on the decomposition of austenite as well as the δ-ferrite to austenite phase transformation in welding processes. The transformation kinetics in welding are different from continuous casting due to the faster cooling rates (shorter heat cycles) involved in welding than in continuous casting. Therefore, the main purpose of this work was to study the high temperature δ-ferrite to austenite transformation in simulated continuous casting conditions vis-à-vis the:

- Effect of cooling rate (CCT diagrams)
- Influence of the alloying elements (chemical composition) on the δ-ferrite to austenite transformation
- Influence of the δ-ferrite to austenite phase change on the side bulging and width variation problem during continuous casting.

University of Pretoria – Siyasiya C. W. (2004)
The phase changes in 3CR12 and the measuring techniques
_____

1.3 Techniques for measuring the ferrite-austenite phase change

1.3.1 Dilatometry

The fundamental principle behind dilatometry is derived from the interaction of neighbouring atoms in a crystalline solid. The relationship between the total energy of an atom U with respect to the inter-atomic spacing r is of the form:

$$U = -\left[\frac{A}{r^m} + \frac{B}{r^n}\right]$$
(1.3.1.1)

The atoms oscillate about the equilibrium position and the inter-atomic spacing varies with temperature. Figure 1.5 below is a schematic illustration of the variation of the total energy U with inter-atomic spacing r.
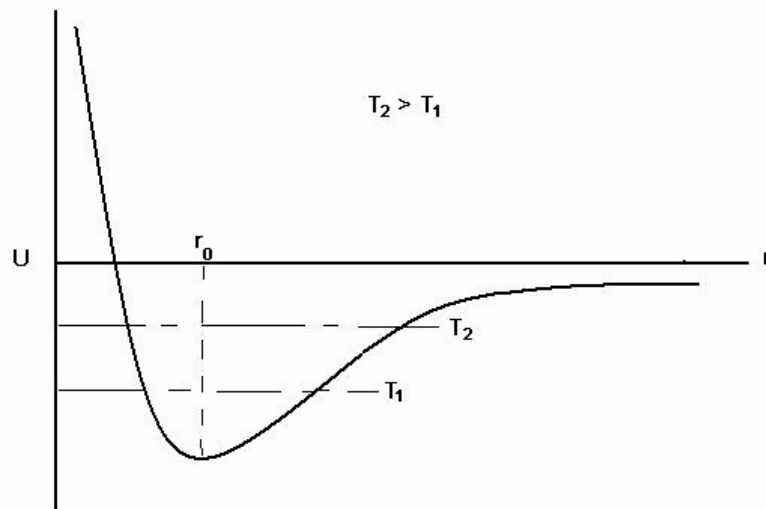
Figure 1.5 - Variation of the total energy of an atom U with inter-atomic spacing r

The inter-atomic spacing is greater at a higher temperature T_2 than at a lower temperature T_1 and due to the asymmetry of the curve, the solid expands. The mean coefficient of thermal expansion is given by:

$$\beta_m = \left[\frac{(a_t - a_o)}{a_o}\right] \times \left[\frac{1}{T}\right]$$
(1.3.1.2)

- 14 -

University of Pretoria – Siyasiya C. W. (2004)
The phase changes in 3CR12 and the measuring techniques
_____

where β_m is the mean coefficient of thermal expansion, a_t is the lattice parameter at temperature T and a_0 is the lattice parameter at 0 K.

The atoms oscillate more as the thermal energy increases. Hence, it is a common phenomenon that steel expands volumetrically with increasing temperature. It has also been demonstrated that the thermal coefficient of expansion of austenite is approximately constant up to 1200 °C and that of ferrite is constant above 300 ˚C. The linear dependence of the lattice parameter on temperature holds even when alloying elements are added[10,11]. Therefore, any phase change between 300 °C and 1200 °C can be observed through the change in the coefficient of expansion or contraction of the steel so long as the specimen is not constrained. The difference in linear differential expansion coefficients of α-ferrite and austenite are due to the differences in densities as ferrite is "loosely packed" (BCC) compared to the "closely packed" austenite (FCC) and the ranges are 10 to12 x 10^{-6} K^{-1} and 15 to18 x 10^{-6} K^{-1} respectively[12]. Figure 1.6 below summarises the temperature dependence of the density for pure iron.
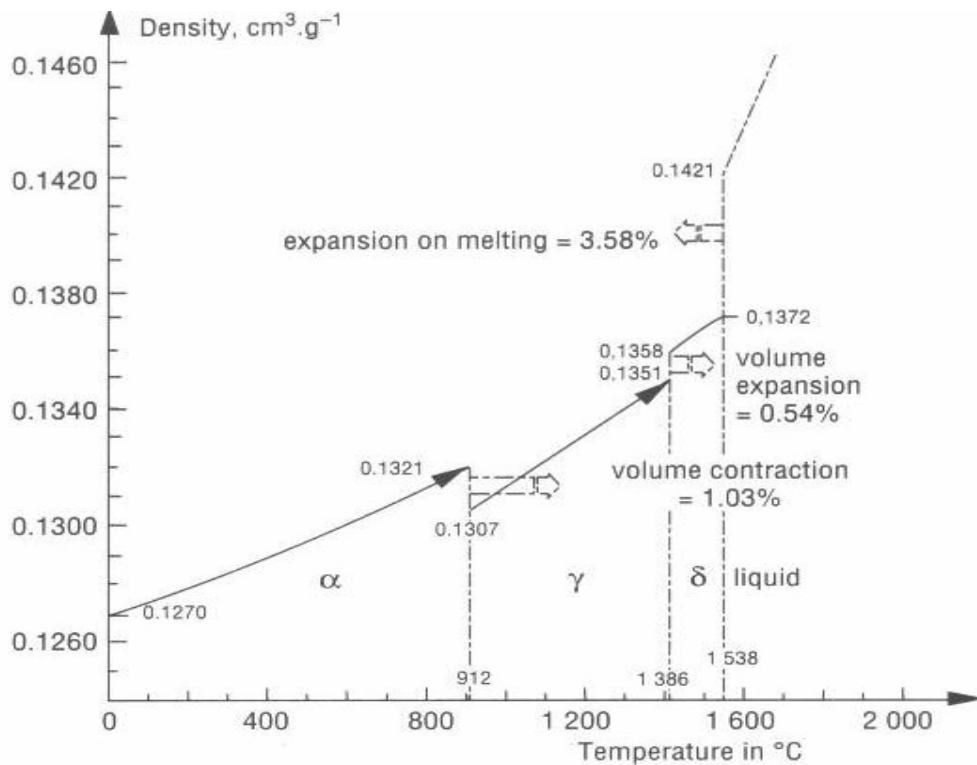
Figure 1.6 - The temperature dependence of iron density[13]

University of Pretoria – Siyasiya C. W. (2004)
The phase changes in 3CR12 and the measuring techniques

_____

From this figure 1.6, the volume change at 912 ˚C of α-ferrite to austenite of 1.03% reduces to only 0.54% at 1368 ˚C for the austenite to δ-ferrite phase change. This makes it more difficult to measure the high temperature δ-ferrite to austenite phase change by conventional dilatometry, as opposed to the lower temperature phase transformation of austenite to α-ferrite.

1.3.2 Electrical Resistance

This technique works on the same principle of a change in physical property as a phase transformation takes place. Instead of measuring the change in volume or strain, the change in resistivity is measured in order to monitor the phase change. Electrical resistance increases with an increase in temperature due to thermal oscillations of the atoms in the crystal lattice. A change in slope of the resistivity curve is attributed to the change in either crystal structure (phase change) or magnetic ordering, as in the case of iron. The loosely packed ferrite has a higher resistivity than the closely packed austenite and this makes it possible to measure the ferrite to austenite phase transformation. The current that is used to heat the specimen may also be used to measure the resistance. A schematic arrangement is shown in figure 1.7 below.

From the basic Ohm's law, the current in the conductor and specimen is the same and therefore:

$$I = \left[\frac{V_1}{R_1}\right] = \left[\frac{V_2}{R_2}\right] \qquad\qquad (1.3.2.1)$$

And since the resistance of the conductor is assumed constant i.e. R_2 is constant:

$$R_1 \propto \frac{V_1}{V_2} \qquad\qquad (1.3.2.2)$$

Therefore by measuring this ratio, it determines the change in resistivity of the specimen during the thermal cycle.

_____
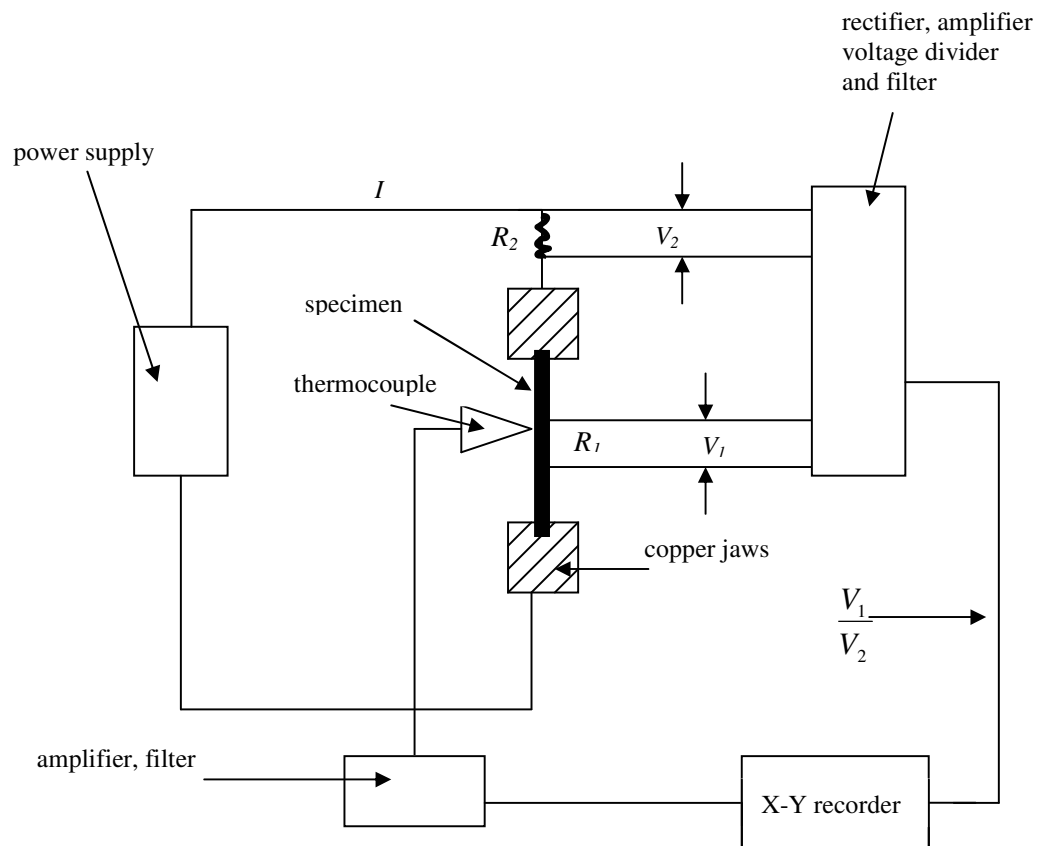
Figure 1.7 - The schematic arrangement of the resistance method for measuring the phase change[32]

The resistance of any current carrying lead as a function of temperature is given by:

$$R_{(T)} = \rho \left[\frac{L}{A} \right]_{(T)} \qquad (1.3.2.3a)$$

where $R_{(T)}$ is the resistance of the material at temperature T, ρ is the resistivity, L is the length and A is the cross-sectional area of the material.

For the dual phase steel,

$$R_{(\delta+\gamma)} = \left[\frac{\rho L}{A} \right]_{(\delta+\gamma)} \qquad (1.3.2.3b)$$

The phase changes in 3CR12 and the measuring techniques
_____

The advantage of using this technique is that there is no temperature limit, i.e. the specimen can be heated up to very close to the melting temperature, making it possible to measure any phase transformation close to the melting point.

1.3.3 Continuous Cooling Compression Test (CCC)

The principle employed in this technique is that there is stress relaxation accompanying the austenite to ferrite phase change in a compressed specimen deformed at a constant strain rate. The measured compressive stress increases smoothly in response to the decrease in temperature, provided the microstructure does not change because the modulus of elasticity increases at a regular rate with the decrease in temperature. Therefore, any deviation from this behaviour is an indication of a phase change. Any sudden change in stress relaxation is due to the increase in volume fraction of the softer ferrite as the phase change progresses. This technique is convenient in instances where bulging of the specimen due to the compressive deformation, interferes with the Linear Variable Differential Transducer (LVDT) of a dilatometer that is placed cross-wise over the diameter of the cylindrical specimen.

1.3.4 Metallography

The specimen is heated or cooled to the transformation temperature where it is held for equilibrium conditions to prevail and thereafter it is quenched to room temperature with the intention of freezing the high temperature equilibrium condition. This is effectively achieved when very thin specimens are used with an effective quench medium such as brine. If thick specimens are used, some transformation (especially at the centre of the specimen), may take place during the quenching which is undesirable.

There are basically three methods by which the volume fraction of the second phase can be determined in opaque objects through a two dimensional cross section of the sample namely:

 (a) The area fraction A_a that the second phase occupies is equated to its volume fraction V_v, i.e.

_____

$$A_a = V_v \qquad\qquad (1.3.4.1)$$

(b) A random line L is drawn through the two-dimensional cross section and the line fraction L_l that the second phase occupies on this line, is equated to the volume fraction V_v in the three dimensional body of the sample.

$$L_l = V_v \qquad\qquad (1.3.4.2)$$

(c) Randomly placed set of points (25) on the two-dimensional cross section are used and those that fall on the second phase, expressed as a fraction of the total set of points P_p, are equated to the volume fraction V_v, i.e.

$$P_p = V_v \qquad\qquad (1.3.4.3)$$

There are statistical and experimental errors in all of these techniques. Experimental errors are associated with sample preparation (depth of etching which must be kept to a minimum) and the measuring technique (resolution capability of the microscope).

Chapter 2

Continuous casting of ferritic stainless steels at Columbus Stainless
_____

2.1 Continuous casting

Columbus Stainless uses the bow type of caster and the average casting speed for the ferritic steels is 1.01 m/min. Figure 2.1 below is the schematic presentation of the caster, showing the major dimensions. In the continuous slab casting process, the molten steel flows from a ladle, through a tundish into the mould. The molten steel is protected from exposure to air by a slag cover over each vessel and by ceramic nozzles between vessels. Once in the mould, the molten steel freezes against the water-cooled copper mould walls to form a solid shell.
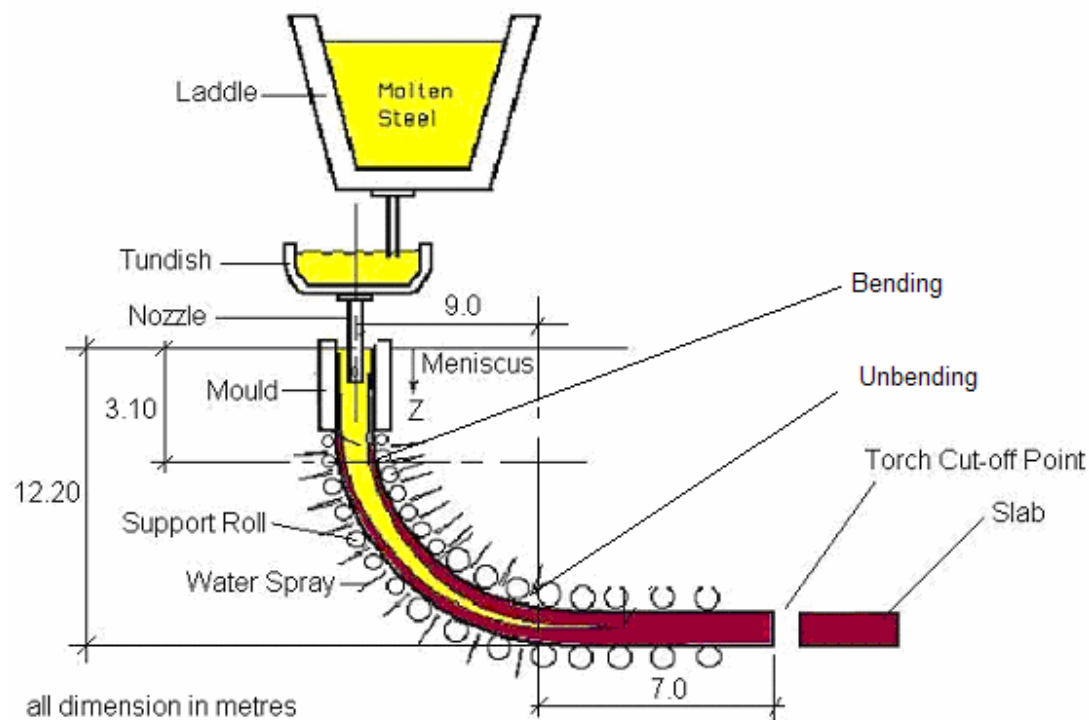
Figure 2.1 - The schematic diagram of the bow-type continuous caster showing the major dimensions

The nominal slab size is 1210 millimetres wide and 200 millimetres thick.

2.2 Modelling of the surface and centre temperature profiles of the strand

In general the temperature profile for all ferritic stainless steels as they cool down after exiting from the mould is the same. Some of the grades of ferritic stainless steels produced

University of Pretoria – Siyasiya C. W. (2004)
Continuous casting of ferritic stainless steels at Columbus Stainless

_____

(a)

A = Mould exit [0.78 m]   B = Straightening start [14.667 m]
C = Straigthening finish [18.721 m]
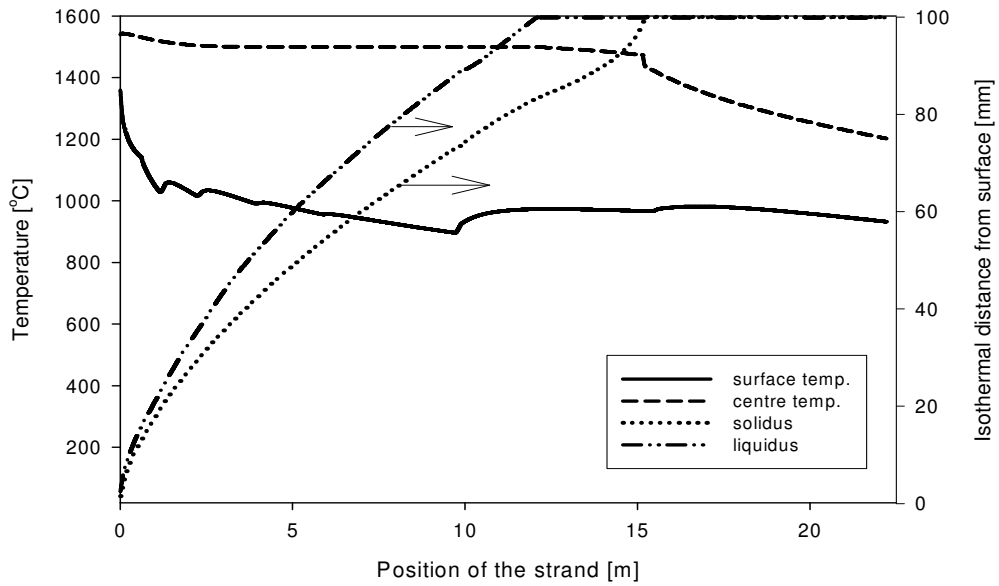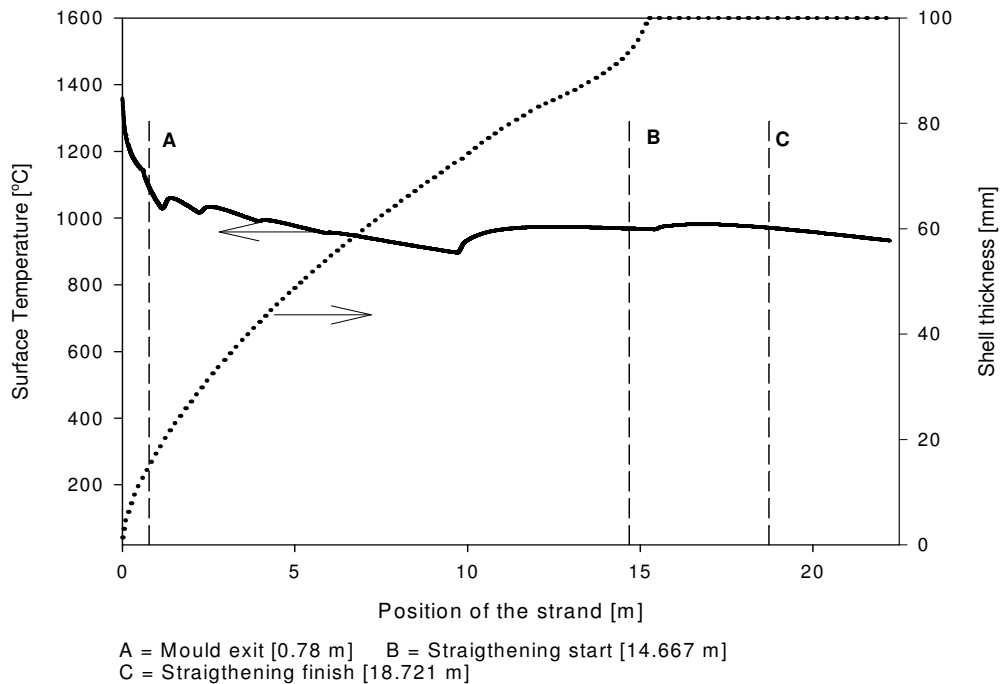
(b)

Figure 2.2 - (a) The typical modelled temperature profiles for type 412 strand obtained from
the on-line data acquisition at Columbus Stainless' continuous caster as well as the shell
thickness (solidus); (b) positions of mould exit and the straightening region

- 21 -

University of Pretoria – Siyasiya C. W. (2004)
Continuous casting of ferritic stainless steels at Columbus Stainless
_____

at Columbus are 409, 412, 430, 3CR12, 410 and 420. Typical surface and centre temperature profiles for type 412 (a high titanium variant of 3CR12) are given in figure 2.2. The solidification shell thickness is also shown in figure 2.2 (labelled solidus). As expected, due to slow cooling, the centre temperature remains almost constant until after 15.0 metres away from the meniscus. The position of the strand referred to in figure 2.2 is along the strand in the casting direction.

The modelled solidus is the temperature at which the metal is fully solid, i.e. forms a shell, whereas the modelled liquidus is the temperature at which the nucleation of solid particles starts, and in between the two, there is a mushy zone. The heat transfer takes place in two regions, namely, in the mould (thus, primary cooling) and after exiting from the mould, thus, secondary cooling.

During primary cooling, water is circulated through the chambers of the mould and it, therefore, is essentially a heat exchanger. In the secondary cooling region radiation, conduction and water spray are used to cool the strand.

Due to the complexity of the industrial continuous casting operation, it is practically impossible to measure the surface temperatures continuously during the continuous casting process. The temperature profile is, therefore, modelled using an energy balance approach that is based on the heat transfer equations. This is done using on-line process control computers that are installed with proprietary software packages that are specially designed for this purpose.

2.2.1 Surface temperature modelling

There are basically three forms of heat transfer that take place on the surface of the strand as it exits the mould, namely radiation, convection and conduction. Heat transfer through radiation is predominant in the upper part of the secondary cooling section and is described by the equation:

$$Q = \varepsilon \mathrm{EA} \left[T_s^4 - T_a^4 \right] \hspace{3cm} (2.2.1.1)$$

University of Pretoria – Siyasiya C. W. (2004)
Continuous casting of ferritic stainless steels at Columbus Stainless

---

where Q is the rate of heat flow (J/s), ε is the Stefan-Boltzmann constant (5.7×10^{-8} $Wm^{-2}K^{-4}$), E is the emissivity constant, typically 0.8 (a measure of the body's ability to emit heat relative to a black body or perfect radiator), A is the surface area m^{-2}, and T_s and T_a are the steel surface and ambient temperatures respectively.

The heat transfer mechanism in convection occurs through the moving spray of water or mist from the spray nozzles and is described by Newton's law of cooling:

$$Q = hA\left[T_s - T_w\right] \qquad\qquad (2.2.1.2)$$

where the coefficient of heat transfer, h (a constant), is determined experimentally for selected water flow rates, nozzle type, water pressure or air pressure if mist is used, T_w is the sprayed water temperature and A and T_s are as defined above.

The heat transfer between the steel surface and the rolls is by conduction and is described by Fourier's law at steady state:

$$Q = kA\left[T_s - T_r\right] \qquad\qquad (2.2.1.3)$$

where k is the thermal conductivity of the containment rolls and T_r is the temperature of the water flowing inside the roll, and A and T_s are as defined above.

2.2.2 Half thickness (centre) temperature
The heat transfer between the centre and the surface (perpendicular to the casting direction) is predominantly by conduction and it is therefore described by a one-dimensional function, the Fourier's law of heat transfer:

$$Q = kA\left[T_s - T_a\right] \qquad\qquad (2.2.1.4)$$

where k is the thermal conductivity of the steel.

University of Pretoria – Siyasiya C. W. (2004)
Continuous casting of ferritic stainless steels at Columbus Stainless
_____

It is assumed that thermal conductivity in the casting direction is negligible and that the energy transfer in the casting direction is dominated by convection due to the casting speed.

The complexity of the matter is that equations 2.2.1.1 to 2.2.1.4 are applicable to a specific point along the strand with known variables. Unfortunately, these variables keep changing with temperature as the strand progresses down the caster. For instance, the thermal conductivity at any point will depend on the existing phase distribution at that point that in turn is dependent on the temperature at any given point. In order to circumvent this problem, finite element modelling and other computer packages that estimate the polynomial function of the temperature are employed in the proprietary program to model the surface and the centre temperature profiles using the basic heat transfer equations cited above.

2.3 Estimation of the average cooling profile from the modelled temperature
The strand is discretised into small slices that move through the casting machine at the casting speed, see figure 2.3.
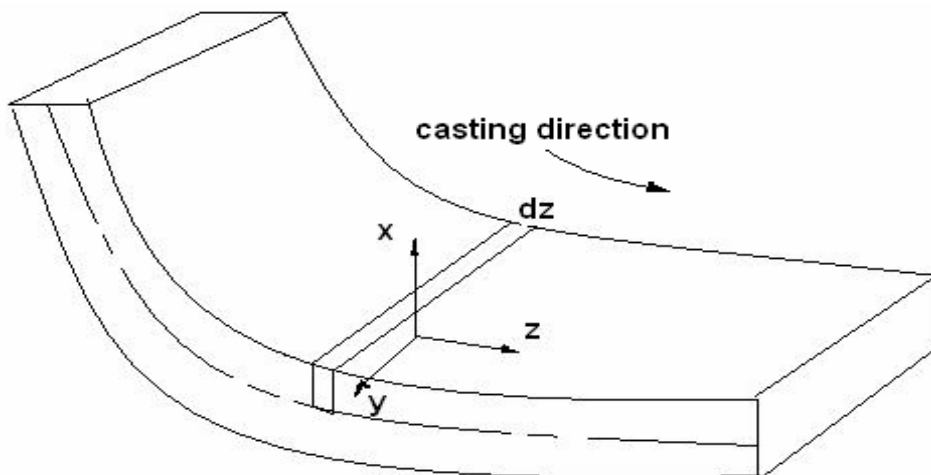

Figure 2.3 - Discretisation of half thickness of the strand in the casting direction z

The average temperature drop with time (average cooling) from one slice to the next along the strand can be estimated as follows:

University of Pretoria – Siyasiya C. W. (2004)
Continuous casting of ferritic stainless steels at Columbus Stainless
_____

$$C = \Delta T \left[\frac{v}{dz} \right] \qquad\qquad (2.3.1a)$$

where dz is the slice thickness in m, ΔT is the temperature change over a slice of the strand dz in the casting direction in °C, v is the casting speed in m/min and C is the average cooling rate in °C/min.

Consider dicsretising the strand into 50 mm slices. At a position 255 mm away from the mould exit point, the surface temperature is 1192 °C and at 305 mm it is 1181 °C, see figure 2.2. Applying equation 2.3.1 above, the average cooling rate over this slice is:

$$C = 101 \left[\frac{1192 - 1181}{0.05} \right] = 222.2 \,^{\circ}C / \min \qquad\qquad (2.3.1b)$$

Applying equation 2.3.1 over the entire strand length generates the surface cooling profile given in figure 2.4 below. From this model the following may be learnt:

- The cooling rate of the strand in the mould (primary cooling rate) is extremely high, ranging from 200 °C/ min at mould exit to 1500 °C/ min at the meniscus.
- The average cooling rate in the secondary cooling region is about 200-300 °C/min.
- The solidification shell grows thicker as the cooling progresses.
- Once the strand enters the unbending zone, water is sprayed from the top only (that is by design) and this introduces a non-uniform cooling rate between the top and the bottom of the strand.
- The cooling is controlled in order to maintain the unbending temperature within the range of 900-1000 °C. This is evidenced by the negative cooling rate, points a, b and c, that signify reheating in figure 2.4.

In brief, this provides a window, in terms of cooling rates, within which the simulated CCT experiments must be carried out if plant conditions are to be simulated.

University of Pretoria – Siyasiya C. W. (2004)
Continuous casting of ferritic stainless steels at Columbus Stainless

_____
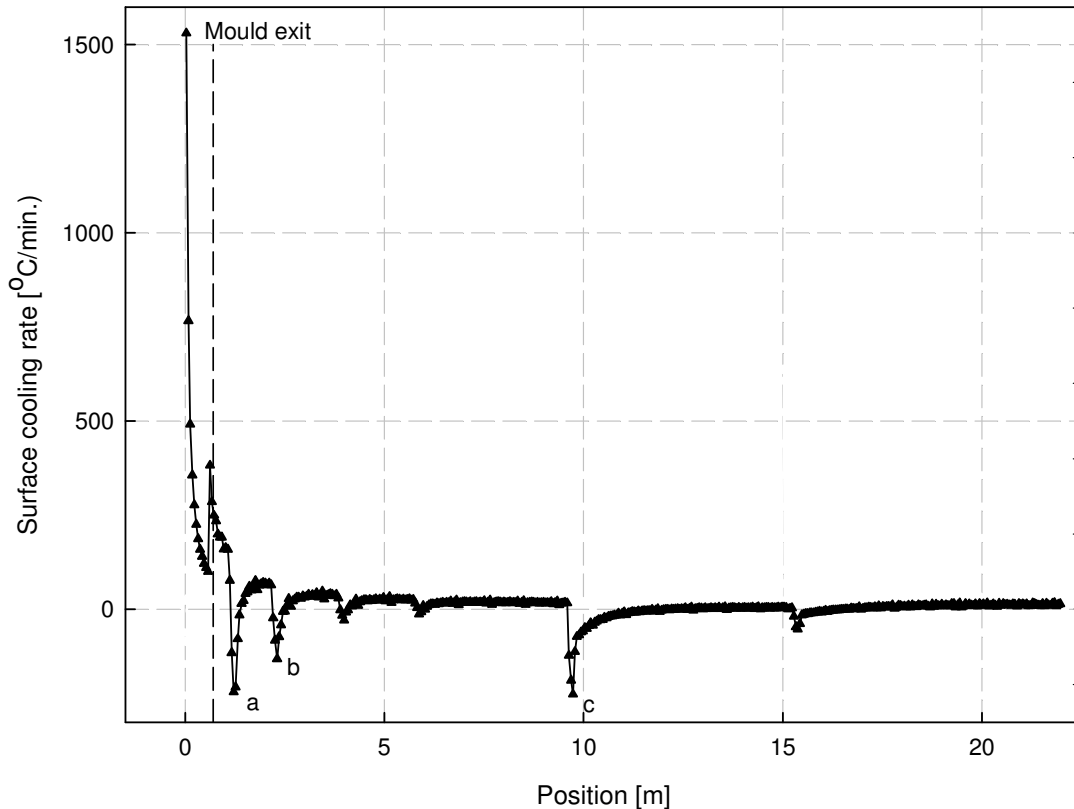
Figure 2.4 - The modelled average cooling rate profile for the strand surface for a typical ferritic stainless steel type-412 (which is identical to all ferritic stainless steels at Columbus Stainless)

2.4 Side bulging and off-corner depression

One of the problems that are encountered during continuous casting of 3CR12 stainless steel is side bulging that sometimes is accompanied with an off-corner depression. Side bulging is a casting defect that results in the bulging of the unconstrained side walls of the strand during continuous casting and occurs particularly in ferritic stainless steels, figure 2.5. Off-corner depression occurs as a form of a gutter, up to about 3 mm deep, adjacent to the top or bottom corner of the slab. Side bulging effect is carried over to subsequent hot rolling processes down the production line and is a problem when unacceptable slab width variations are encountered.

University of Pretoria – Siyasiya C. W. (2004)
Continuous casting of ferritic stainless steels at Columbus Stainless
_____
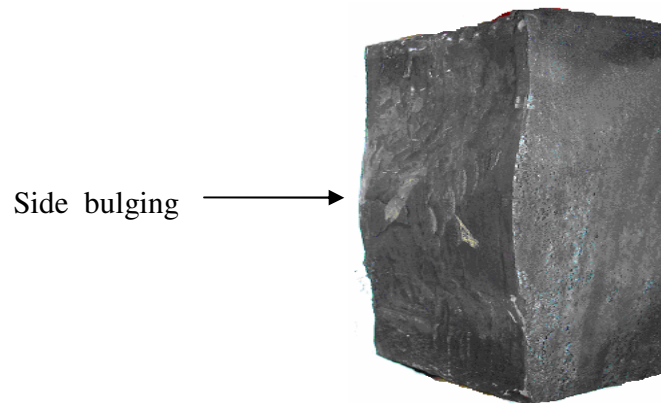
Figures 2.7 - Section of a slab showing side bulging

In general, the literature addresses top and bottom surface bulging between two successive rollers with little regard to side bulging. However, in a study on the improvement of surface quality of austenitic stainless steel, Okimori et al[14] observed that the side bulging is related to the taper of the mould and the viscosity of the mould powder. The philosophy is that with low viscosity mould powder, the thickness of the molten powder film between the mould and the solidification shell is large (i.e. low viscosity powder flows easily into the gap between the mould and the solid shell). As a result, the heat transfer through the mould is low, the cooling of the strand is slow, the shell thickness is small, the temperature of the solidification shell is high, and, therefore, the shell strength is decreased. The situation becomes worse when air gaps exist between the mould and the solidification shell because the heat transfer is hindered even further due to poor thermal conductivity of air. Coupled with this, when the taper of a mould on the narrow face is not sufficient (if it is smaller), the cooling of the strand through the mould becomes insufficient too, due to ineffective contact between the mould and the strand. Consequently, the solidification shell does not have enough strength to withstand the ferrostatic pressure from the liquid column and thermal stresses arise and, therefore, side bulging takes place. Although Okimori and co-worker's observation was on an austenitic stainless steel, it can also be relevant to ferritic stainless steels that are even more vulnerable to side bulging than the former (due to the δ-ferrite solidification mode). In view of the foregoing, it would, therefore, be worthwhile to investigate the influence of the austenite start temperature vis-à-vis the chemical composition, knowing that austenite has a higher hot strength than δ-ferrite[15].

Chapter 3

The hot ductility of the 3CR12 steel

_____

3.1 Introduction

In a bow type caster, figure 2.1, the strand is initially withdrawn in the vertical plane and as it progresses it is guided through a prescribed arc into the horizontal plane. During this bending process, the outer radius of the strand is placed under tension and the inner radius in compression. After passing through the prescribed bending arc, the strand is unbent or straightened to return it to a flat condition in the horizontal plane. The straightening reverses the strains, i.e. the inner radius experiences tensile strain and the outer compressive strain. Since in both elastic and plastic bending the strain is proportional to the distance from the neutral axis, it is therefore the outer (or bottom) surface that is most vulnerable to transverse cracking during bending and other strain-related surface defects whereas during unbending, it will be the inner (or top) surface that is most vulnerable.

The bending is done at a higher temperature than the straightening and this is generally outside the region within which the steel experiences poor high temperature ductility (also known as a ductility trough). Hence, it is not crucial for quality control of the strain-related surface defects. However, the straightening, which is done in the temperature range of 800 °C to 1200 °C within which the ductility trough often exists in some steels, is very crucial for the quality control of the surface defects, particularly transverse cracking. It is, therefore, necessary that the ductility trough should be avoided at all cost through optimised cooling and casting speed in order to avert these defects.

According to the theory of bending, the strain increases with a decreasing radius of curvature. The tensile engineering strain on the outer surface e_a is assumed to be equal to the compressive strain on the inner surface e_b, i.e.

$$e_a = e_b = \left[\frac{1}{\left(\frac{2R}{b} + 1 \right)} \right] \qquad (3.1)$$

University of Pretoria – Siyasiya C. W. (2004)
The hot ductility of the 3CR12 steel

_____

where R is the radius of curvature (the mid-line radius of the slab) and b is the strand thickness. For large values of R/b equation 3.1 reduces to:

$$e_a = e_b = \left[\frac{b}{2R}\right] \qquad\qquad (3.2a)$$

or in terms of the true strain:

$$\varepsilon = \ln\left[1+\frac{b}{2R}\right] \qquad\qquad (3.2b)$$

However if the strand is not fully solid, i.e. the liquid or mushy zone is still existing in the strand, equation 3.2 is modified accordingly[16]:

$$e = \left[\frac{b-2t}{2R}\right] \qquad\qquad (3.3a)$$

where t is the thickness of the solid shell.

Therefore, the true strain becomes:

$$\varepsilon = \ln\left[1+\frac{b-2t}{2R}\right] \qquad\qquad (3.3b)$$

Therefore the average strain rate over the entire unbending length is given by:

$$\dot{e} = \left[\frac{eV}{L}\right] \qquad\qquad (3.4a)$$

or in terms of the true strain rate:

University of Pretoria – Siyasiya C. W. (2004)
The hot ductility of the 3CR12 steel

_____

$$\dot{\varepsilon} = \ln\left[1 + \frac{eV}{L}\right] \qquad\qquad (3.4b)$$

where V is the casting speed (ms^{-1}) and L is the length of the unbending zone in meters.

3.2 Hot ductility during continuous casting of steels

As mentioned earlier, during continuous casting of ferritic and austenitic steels, there is often a temperature range within which poor high temperature ductility occurs in some steels. This behaviour is measured by examining the percentage reduction in area of the fractured surface at a particular temperature after a high temperature tensile test at the appropriate strain rate[17]. Figure 3.1 shows a schematic diagram of the hot ductility trough. The 50% reduction in area is regarded as the limit below which the ductility is considered poor.
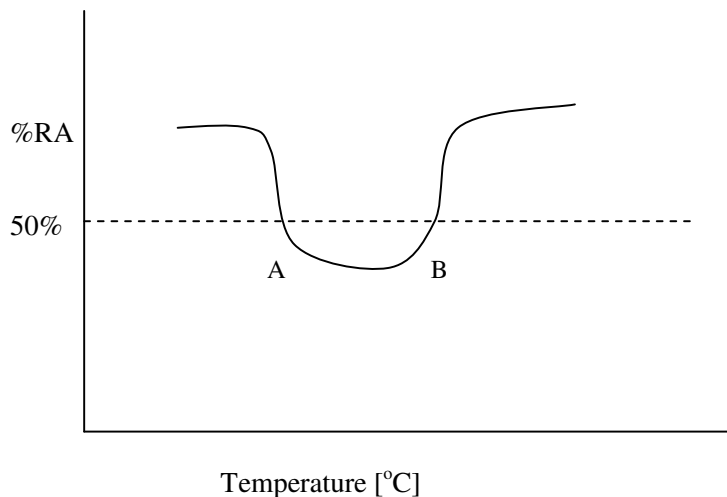
Figure 3.1 - The schematic presentation of the hot ductility characteristic curve

It has been suggested that there are two mechanisms that account for the poor hot ductility in some of the austenitic steels, namely, grain boundary sliding in the austenite grain boundaries and the presence of softer ferrite films surrounding the austenite grains, which allow strain concentration to occur preferentially on the grain boundaries. The hot ductility improves (particularly in HSLA steels) when there is a large amount of ferrite since ferrite exhibits excellent hot ductility properties[18]. During straightening, 3CR12 is in the ferrite-austenite dual phase region at about 1000 °C and, therefore, its hot ductility characteristics may depend on the austenite to ferrite phase volume ratio.

University of Pretoria – Siyasiya C. W. (2004)
The hot ductility of the 3CR12 steel
_____

Suzuki et al[19] observed no ductility trough for the temperature range 1200 °C to 700 °C for a low carbon 0.002%(C+N)-16%Cr ferritic steel when tested at strain rates from 10^{-7} to 10^{-3} s^{-1}. Contrary to Suzuki's observation, Mintz and coworkers[20] observed ductility troughs in a low carbon steel, 0.013%(C+N)-0.28%Ti-18.5%Cr ferritic steel. The ductility troughs were attributed to the presence of precipitates and inclusions, and failure was by intragranular micro-void coalescence and not by grain boundary sliding (cleavage failure). The SEM analysis revealed that the presence of the coarse TiN particles was the major cause of the ductile failure. Since the failure mode in ferritic steels is one of ductile micro-void coalescence, the hot ductility is controlled by the volume fraction of the inclusions and the rate of recovery.

In austenitic steels, the hot ductility is exacerbated with slow strain rates (10^{-4}s^{-1}) whereas in ferritic steels it is the opposite with high strain rates (10^{-1}s^{-1}) detrimental to the hot ductility[20]. Increasing the strain rate increases the rate of dislocation density increase and work hardening and consequently the ductility decreases if recrystallisation does not occur. The difference in the hot ductility characteristics of austenitic and ferritic steels is attributable to the difference in the failure mechanisms: one is by grain boundary sliding while the other one is by ductile micro-void coalescence respectively.

Apart from the presence of tensile strain on the top surface of the strand during the unbending process, the surface of the strand is subjected to high cooling rates that lead to the nucleation of finer particles in the austenite grain boundaries that are detrimental to the hot ductility. Fine particles are effective in pinning the grain boundaries, thereby preventing or delaying the dynamic recrystallisation and in the process, promoting grain boundary sliding. There is also evidence that fine particles on a grain boundary, anchor the boundary and prevent sliding. Work done by Comineli et al[21] in C-Mn-Nb-Al steels has shown that increasing the cooling rate always results in worse ductility since finer precipitate and inclusion distributions are found on the austenite grain boundaries. This might not be the case with 3CR12 since it does not contain niobium and significant amounts of aluminium.

University of Pretoria – Siyasiya C. W. (2004)
The hot ductility of the 3CR12 steel
_____

The work done by Mintz[22] and Maehara[23] proposed that the presence of columnar grains may exacerbate intergranular cracking. Columnar grains can penetrate deeply to the centre of the slab, providing a continuous path for the crack propagation. Hence severe transverse cracking is often associated with columnar grains.

In general for most austenitic and dual phase steels, at the lower temperature end of the trough A (figure 3.1), the recovery is due to the formation of large amounts of ferrite as the temperature drops and the ductility recovery at the upper temperature end of the trough B is due to dynamic recrystallisation (DRX). It is also worth noting that additions of alloying elements like Ti, Nb and V to the steel that form fine carbonitride particles, give a high activation energy for DRX, i.e. high driving force is required to overcome the Zener drag effect of the fine particles for DRX to set in. Therefore, DRX takes place at higher temperatures.

Chapter 4

Experimental procedures

_____

4.1 Effect of cooling rate and chemical composition on the high temperature δ-ferrite to austenite phase change

4.1.1 The Weld Simulator

In this study, two methods of measuring the δ-ferrite to austenite phase change were used, namely the resistivity technique and metallographic analysis. The metallographic analysis was intended to augment the former.

Dilatometer equipment is usually used to study phase transformations during continuous cooling transformation. The maximum working temperature for the Theta Dilatometer that was available was 1250 °C and, therefore, the δ-ferrite to austenite phase change could not be investigated using that equipment since the δ-ferrite single phase exists above 1250 °C. In view of this, a weld simulator was used. Secondly, as already stated in figure 1.6, the smaller volume change of the δ-ferrite to austenite phase change may make this technique less sensitive than at lower temperature austenite to α-ferrite phase transformation.   The schematic experimental arrangement is given in figures 4.1. High temperature experiments are usually carried out in an inert atmosphere in order to avoid severe oxidation. Oxidation does not only interfere with the effectiveness of the quenching process but also the electrical contacts between the specimen and the thermocouple as well as on resistivity electrodes (potential drop terminals). However in this experimental arrangement, it was not feasible to shield the specimen from the atmosphere by the supply of an inert gas like argon. Therefore, in order to ensure proper contact between the specimen and the thermocouple and with the resistivity electrodes, 1.5 mm diameter and 3 mm deep holes were drilled in the test zone of the samples. The 0.384 mm diameter R-Type (Pt/Pt-13%Rh) thermocouple and the resistivity electrodes of Pt-13%Rh wire, were spot-welded into the bottom of these holes.

University of Pretoria – Siyasiya C. W. (2004)
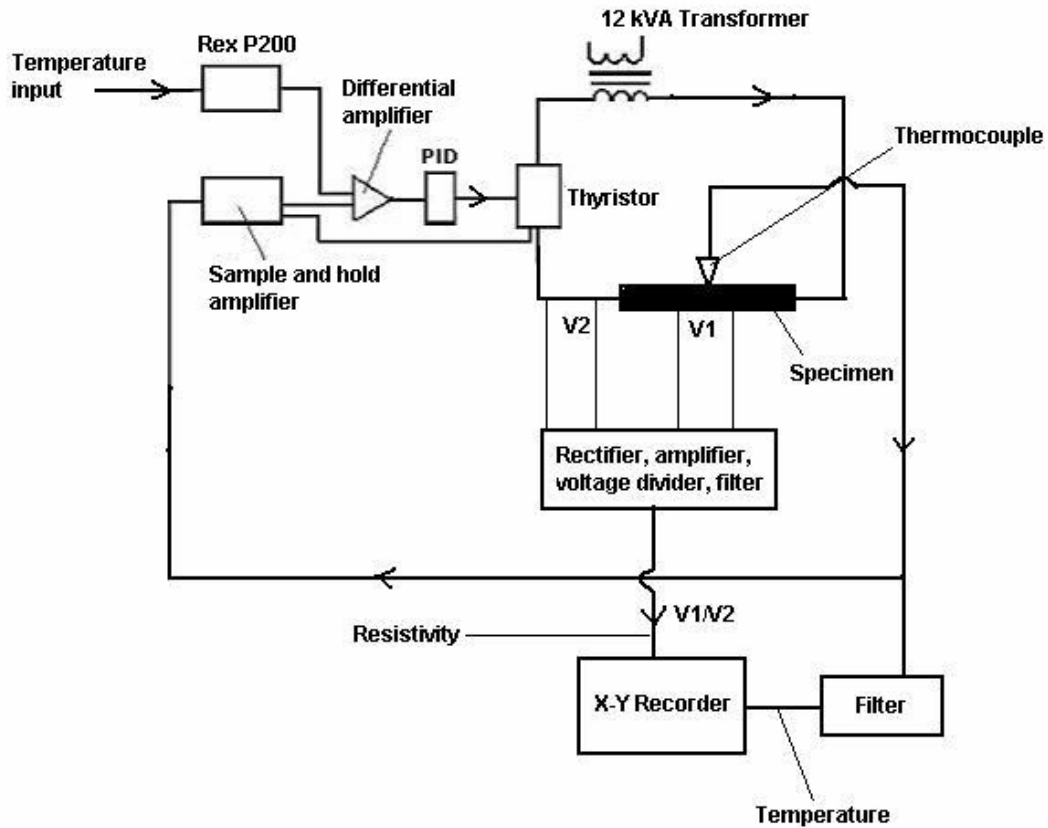**Experimental procedures**

_____

Figure 4.1 - The schematic diagram of the Weld Simulator with its temperature control system and the resistivity measurement technique[32]

The holes were then filled with a paste of alumina with phosphoric acid. Apart from shielding the joints from the atmosphere, the dry alumina enhanced the mechanical strength on the thermocouple contact point. It was imperative that good contact was maintained between the thermocouple and the specimen otherwise the credibility of the transformation temperatures would have been compromised.

4.1.2 Material preparation

Thin specimens (110x3x3 mm) were used in the quench experiments to ensure effective quenching, see figure 4.2 below.
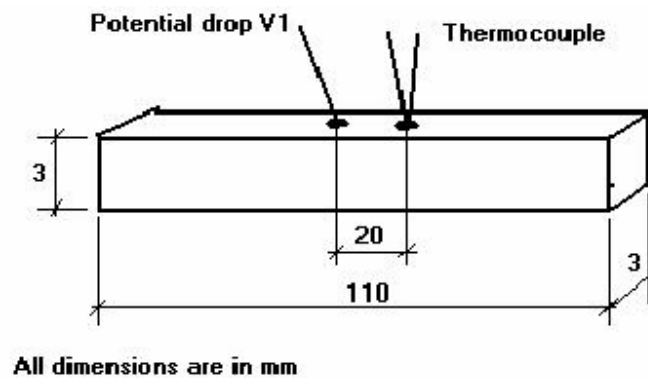
_____

Figure 4.2 - The specimen for the CCT experiment on the Weld Simulator

4.1.3 Temperature distribution along the specimen length

The specimen was clamped between two water-cooled copper jaws; one was fixed while the other one was suspended in order to allow it to move freely, see figure 4.3. This allowed the specimen to expand and contract freely during the thermal cycle. Hence, there was not any constraint on the specimen during the heating and cooling cycle, thereby, minimizing the interference of any change in volume of the test zone with the resistivity measurement. Resistivity is inversely proportional to the cross-sectional area of the specimen and, therefore, it is sensitive to volumetric strain.

As expected, the specimen was cooler at both clamped ends than in the middle of the free span due to the high thermal conductivity of the water-cooled copper jaws. Consequently, this produced a temperature profile along the specimen length. Hence, it was important to ensure that the temperature was measured from the middle of the free span, otherwise, the region that experienced the maximum temperature would melt off before the temperature under investigation was reached.

University of Pretoria – Siyasiy C. W. (2004)
Experimental procedures

_____

Figure 4.3 - Mounting of the specimen, note that the right hand jaw is suspended to allow free expansion and contraction of the specimen

In order to determine the size of the test zone, two thermocouples, one at the centre and the other one off-set by 20 mm from the centre were spot welded to the specimen. The specimen was thereafter heated up to 1000 °C and held for 5 minutes to allow the temperature measurement to stabilize. The intention was to determine the length of the region without significant thermal gradient. The size of the test zone would depend on the length of the free span, the shape and material of the jaws and the temperature. The temperature pattern was generated by a programmable Rex P200 temperature controller. The plot of temperature versus time on the X-Y recorder is shown in figure 4.4 for the two thermocouples. The eventual reading for the two thermocouples was the same and this meant that there was no temperature difference between the two points over a ±20 mm test zone from the centre. Since the size of the test zone increases with temperature, it was concluded that for the 3CR12 specimen whose sizes were 110x3x3 mm, the test zone at all temperatures above 1000 °C would be greater than 40 mm.

University of Pretoria – Siyasiya C. W. (2004)
Experimental procedures
_____
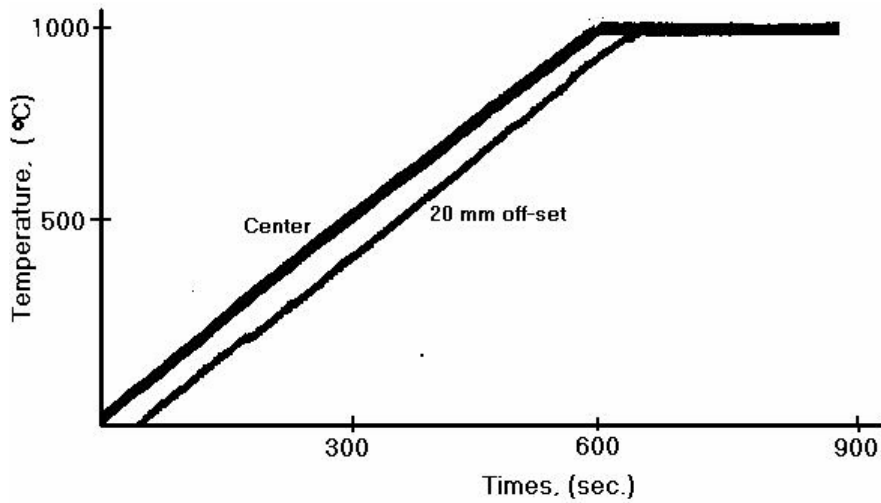
Figure 4.4 - The temperature versus time graph for the two thermocouples that were spot welded in the test zone of the 3CR12 sample

4.1.4 Heating and cooling cycle on the Weld Simulator

Figure 4.5 shows the schematic heating and cooling cycles during the CCT experiments on the Weld Simulator. As has been mentioned earlier in chapter 2, these cooling rates are a simulation of the cooling rates during continuous casting at various positions of the strand.

Figure 4.5 - The typical heating and cooling cycles for the CCT experiments

- 37 -

University of Pretoria – Siyasiya C. W. (2004)
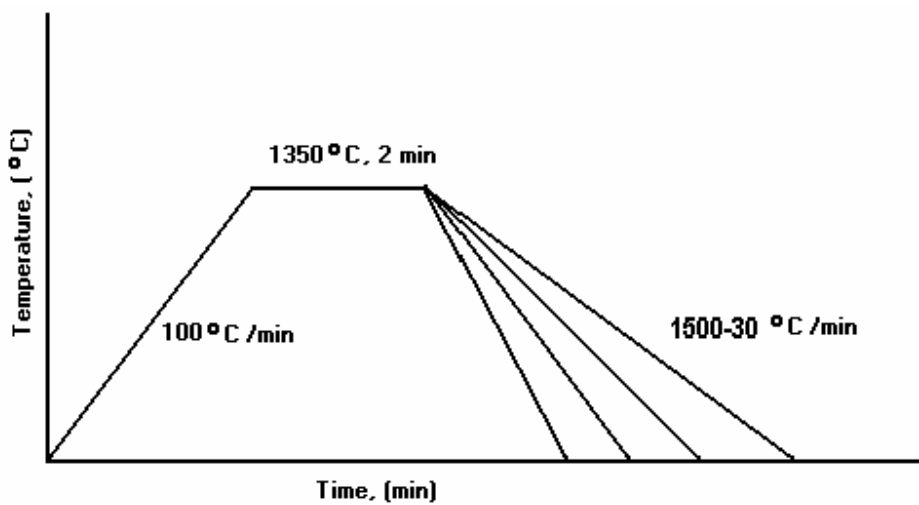**Experimental procedures**

_____

4.1.5 Using a resistivity technique to measure the phase changes in 3CR12

A typical result from the experimental arrangement given in figure 4.1 above is shown in figure 4.6. There are two parts to the curve, one for the heating cycle and the other one for the cooling cycle. The A_{r5} temperature is the δ-ferrite to austenite start temperature and A_{r4} temperature is the δ-ferrite to austenite finish temperature. These phase changes are accompanied by the first and second change in slope of the temperature versus resistivity curve respectively in figure 4.6 as the temperature decreases. The A_{r3} temperature is the α-ferrite start temperature and A_{r1} is the α-ferrite finish temperature. Depending on the cooling rate, not all of the austenite transforms to α-ferrite and this partial regression of austenite to ferrite in 3CR12 steel was also observed by Knutsen[7].

The change in slope during resistivity measurements is sensitive to the cooling rate and chemical composition that determine the δ-ferrite to austenite volume fraction ratio. For instance, a sufficient quantity of austenite formers would stabilize the δ+γ up to the melting
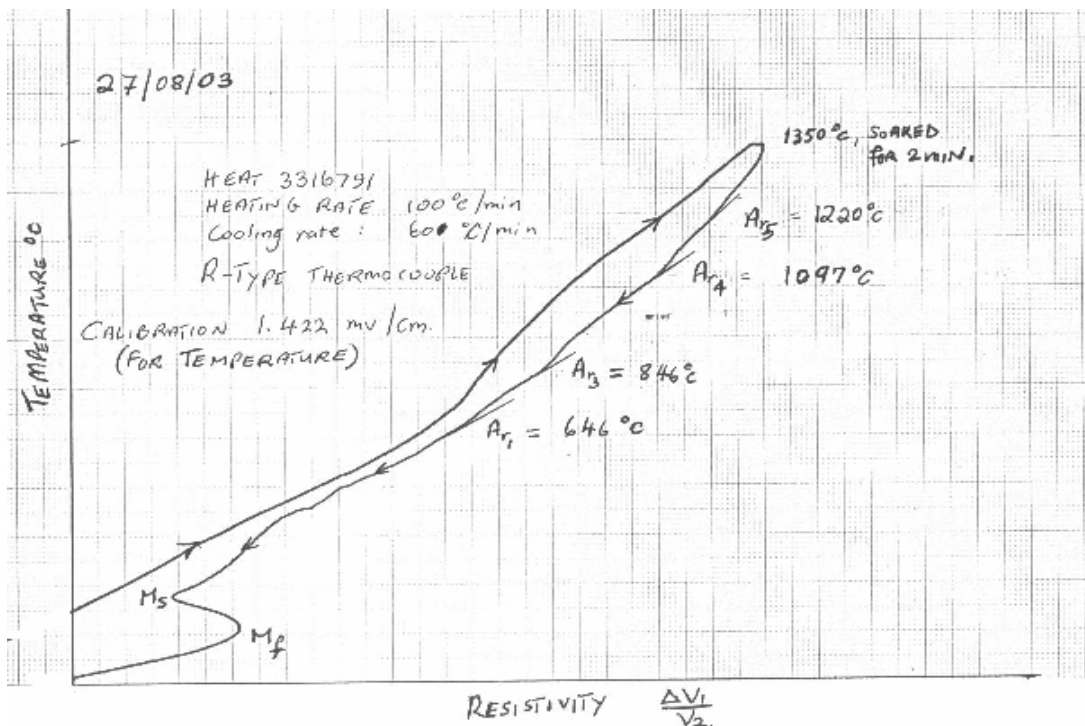

Figure 4.6. The typical temperature versus resistivity curve for 3CR12, showing the change in slope as the phase change takes place. Heat number 3316791, ferrite factor of 11.5

University of Pretoria – Siyasiya C. W. (2004)
Experimental procedures

_____

temperature[24] and, therefore, no distinct change in slope can be observed to mark the δ-ferrite to austenite transformation start temperature. The austenite volume fraction will keep increasing as the temperature continues to decrease until the maximum volume fraction that depends on the chemical composition and cooling rate is reached, then, the austenite starts regressing to α-ferrite at the A_{r3} temperature as it drops further during continuous cooling. The resistivity curve is never linear in the δ-ferrite-austenite dual phase region since the austenite to ferrite ratio keeps changing with the change in temperature and time.

As was mentioned earlier, the focus of this work is to study the δ-ferrite to austenite phase transformation during continuous casting of 3CR12. The study on the decomposition of austenite to α-ferrite in 12%Cr steels has been done extensively by other workers[5,6] and therefore it was not the focus of this study.

4.1.6   Microstructural analysis to check the validity of the perceived transformation temperature in the resistivity technique

Specimens (from the same heat that was used in the resistivity technique) were heated to 1350 °C and soaked for 2 minutes and then cooled to just 10 ˚C above and below the perceived transformation temperature according to the resistivity technique. As may be seen in figure 4.3 above, the specimen was unclamped while at this temperature and drop-quenched into brine. The specimen was polished and etched in modified Kalling's solution: 5g Copper Chloride, 16 ml distilled water, 18 ml Hydrochloric acid and 50 ml Methanol. The microstructures are given in figures 4.7 and 4.9 (a) and (b) below. Metallographic analysis confirmed that single phase δ-ferrite exits at 1350 °C and above, shown in figure 4.7 below. Microanalysis using the energy dispersive X-ray spectroscopy (EDS) in a scanning electron microscope (SEM) also showed that at 1350 °C, only TiN remained in precipitate form while the rest of the carbides were in solution. Some inclusions (alumina inclusions) were also observed in the microanalysis. Figure 4.8 (a) below is a SEM micrograph showing the TiN precipitate and figure 4.8 (b) is the spectroscopic analysis.

University of Pretoria – Siyasiya C. W. (2004)
Experimental procedures
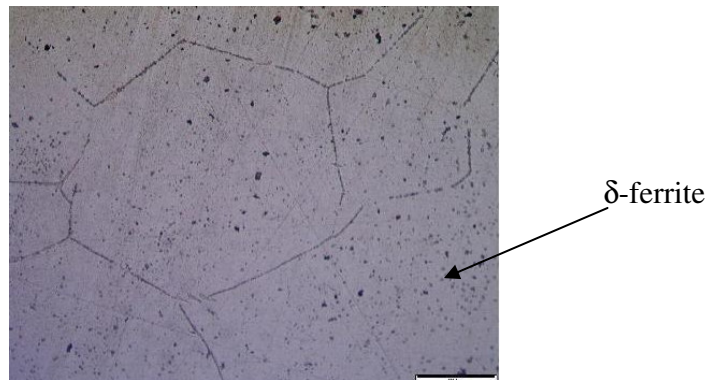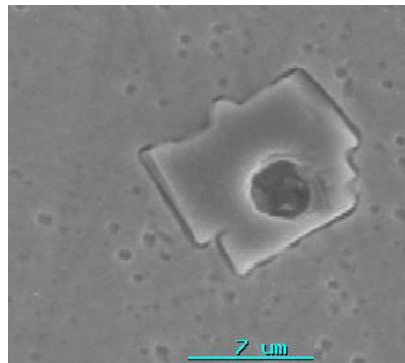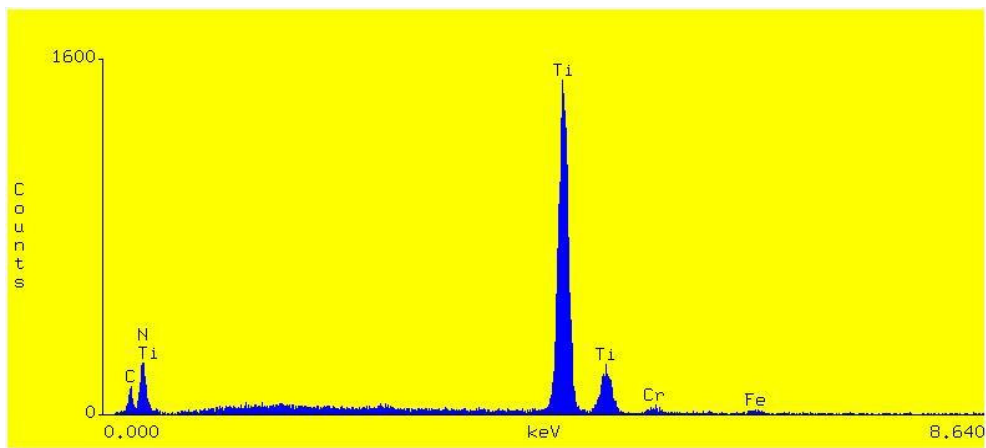
_____

δ-ferrite

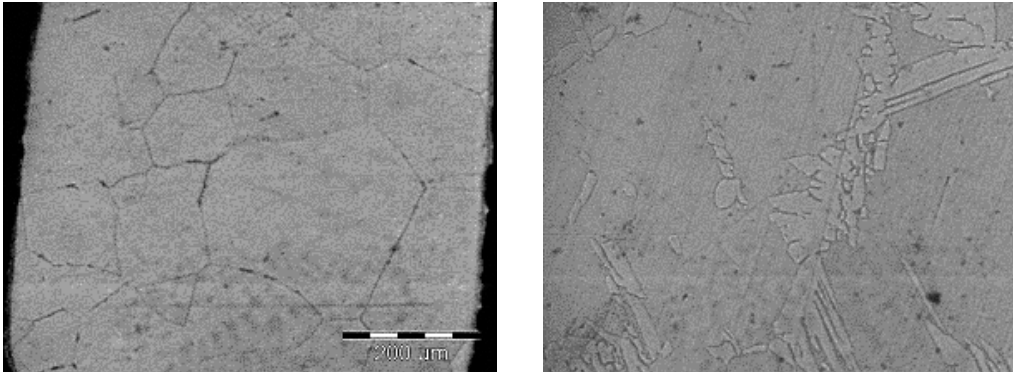Figure 4.7 - The micrograph for the sample that was quenched from 1350 °C, x10

(a)

(b)

Figure 4.8 - (a) A TiN precipitate at 1350 °C as seen on the SEM, (b) EDS spectroscopic analysis

University of Pretoria – Siyasiya C. W. (2004)
Experimental procedures
_____

(a)   (b)

Figure 4.9 - Micrographs for 3CR12 cooled at 60 °C/min. (a) quenched from 1235 °C, (b) quenched from 1200 °C, note the austenite (martensite) transformation along the δ-ferrite grain boundaries. Magnification x5

The micrographs in figures 4.9 (a) and (b) above, confirm the validity of the transformation temperature of 1220 °C at the cooling rate of 60 °C/min as measured by the resistivity technique i.e. single δ-ferrite phase was observed at 1235 °C and ferrite-austenite dual phase at 1200 °C.

4.1.7 Experimental arrangement for the furnace cooling and quench tests

The quenching experiment could either be done using the Weld Simulator or a high temperature furnace. However, there are limitations with each one of these techniques. On the one hand, it is not practical to provide a shielding atmosphere of argon on the Weld Simulator and, therefore, oxidation severely attacks the specimen during the experiment. The oxide layer interferes with the quenching especially when the sample is soaked for a long time and thereafter cooled slowly to the test temperature. The oxides also affect the temperature recording due to poor contact between the thermocouple and the specimen. On the other hand, while it is easy to provide a shielding atmosphere in a furnace, it is practically impossible to achieve high cooling rates (higher

University of Pretoria – Siyasiya C. W. (2004)
Experimental procedures

_____

than air cooling) prior to quenching. Hence, in this study, the Weld Simulator was used for fast cooling rates while a high temperature furnace was used for the slow cooling rates.

Figure 4.10 shows a schematic arrangement of a tube furnace and a basin containing water for the quenching below it. The specimen was suspended at the hottest region of the furnace and in order to measure the accurate temperature of the specimen, the thermocouple was suspended close to the specimen as shown in figure 4.10. Argon gas was used to create an inert atmosphere in order to prevent severe oxidation during the heat treatment.
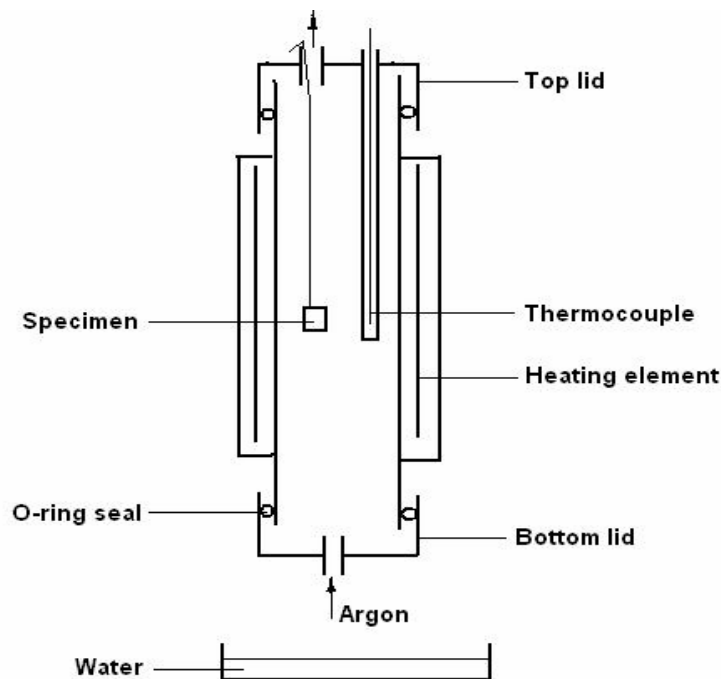
Figure 4.10. The furnace-quench experimental arrangement

Figure 4.11 below summarises the entire heating, cooling and quenching process. Since the δ-ferrite to austenite phase change occurs at very a high temperature, the wire used to suspend the sample was creep resistant Nichrome wire. The as-cast 3CR12 samples obtained from Columbus Stainless were not used in the δ-ferrite to austenite phase change experiments as the chemical composition of the samples would not necessarily be

- 42 -

_____

homogeneous due to segregation during solidification and could vary from sample to sample. Instead, heat treated samples from 3 and 4 mm plate of 3CR12 were used.
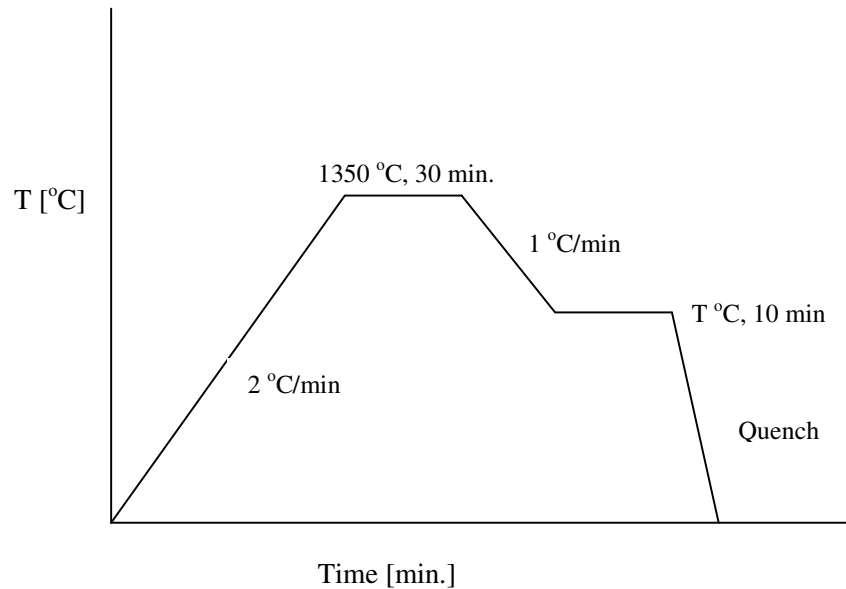
Figure 4.11. The furnace heat treatment cycle

4.1.8 Etching of specimens for microstructural analysis

The specimens were drop quenched in water, mounted and polished for etching. The modified Kalling's solution was used to etch the steel. The specimens were immersed in the solution for 10 to 15 seconds then rinsed in ethanol to neutralise the acid. The ferrite was etched more than the martensite and under the optical microscope, the ferrite appeared light and the austenite dark. The two phases were identified by a micro-hardness test and, as expected, the ferrite was softer than the martensite. The chemical compositions for the 3CR12 steels that were used in the study of phase changes are given in table 4.1 below and all the compositions are in wt-%.

4.1.9 Determination of the volume fraction of the phases and their distribution

In this work, an electronic quantitative software program (analySIS), coupled to an optical

University of Pretoria – Siyasiya C. W. (2004)
Experimental procedures

_____

microscope, was used for the volume fraction measurement. This software program calculates the projected surface area of the second phase directly, provided sufficient contrast between the phases exists. For each measurement of the second phase, over twenty measurements were taken from which the mean and standard deviation were calculated. Therefore, the value for the phase under investigation is the mean from the measurements and the error bars represent the standard deviation.

Heat No.	C	Mn	Ni	N	Cr	Si	Ti	V	P	S	Mo	Co	FF
3387232	0.018	0.56	0.33	0.021	11.61	0.7	0.032	0.11	0.025	0.003	0.01	0.02	**12.1**
330011	0.012	0.49	0.55	0.018	11.57	0.38	0.014	0.11	0.027	0.003	0.01	0.02	**9.64**
3316791	0.021	0.51	0.39	0.018	11.18	0.69	0.033	0.10	0.027	0.002	0.01	0.03	**11.5**
3373793	0.02	0.60	0.40	0.018	11.30	0.66	0.02	0.09	0.03	.0005	0.03	0.02	**11.04**
3373803	0.02	0.54	0.40	0.015	11.20	0.65	0.04	0.08	0.03	.0033	0.03	0.02	**11.71**

Table 4.1 - The chemical composition for the 3CR12 steels that were used in the study. FF stands for Kaltenhauser ferrite factor and the heat number is from Columbus's designation.

The Kaltenhauser ferrite factor (FF) is an empirical equation that is used to predict the microstructure (ferrite volume fraction) at 1000 ˚C, generally in weld metal and it is given by[37]:

$$FF = Cr + 6Si + 8Ti + 4Mo + 2Al + 40(C + N) - 2Mn - 4Ni \qquad (4.1)$$

This equation should therefore be applied with caution at slower cooling rates than those encountered during welding. Pistorius et al[6] concluded that the Kaltenhauser ferrite factor can not be used to predict the high temperature microstructure of the 12%Cr steels because the correlation of the measured ferrite volume fraction and the empirically predicted value resulted in a high degree of scatter.

University of Pretoria – Siyasiya C. W. (2004)
Experimental procedures

_____

4.2 The hot ductility and hot strength experiments

4.2.1 Sample preparation
The samples for the hot ductility test were cut from the top surface along the casting direction of the strand, i.e. 15 mm deep as shown in figure 4.12.

all dimension in mm
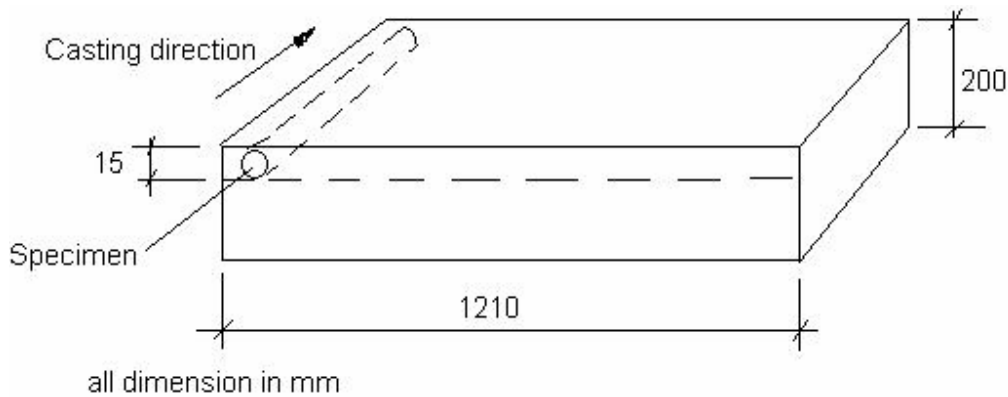
Figure 4.12 - Cutting of the specimens from the top-side of the 3CR12 as-cast slab

The hot ductility test samples were cut from the top side and along the casting direction of the as-cast slab because:

- The top side is subjected to tensile strain during unbending and, therefore, it is more susceptible to transverse cracking.
- A high temperature tensile test perpendicular to the columnar grains would reveal most likely any transverse cracking during unbending.

The specimens for the high temperature tensile tests on the Gleeble 1500 were machined as shown in figure 4.13.

all dimensions in mm

Figure 4.13 - The high temperature tensile test specimen for the Gleeble 1500[TM] machine

University of Pretoria – Siyasiya C. W. (2004)
Experimental procedures
_____

4.2.2 Cooling rate simulation on the Gleeble 1500^{TM} machine
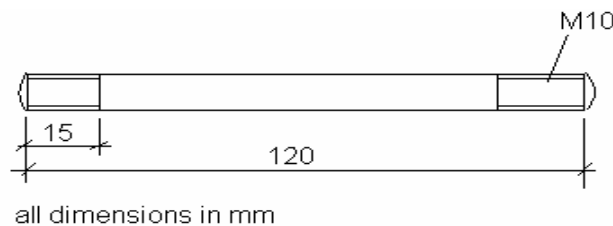
The Gleeble cooling rate was modelled in comparison to the continuous caster modelled surface temperature as shown in figure 4.14. The curve in solid line is the modelled surface temperature obtained from the continuous caster while the rest are simulated cooling rates (dashed lines). Deformation (simulating straightening of the slab), therefore, commenced fifteen minutes after first soaking the sample at 1360 ˚C for 10 minutes and cooling to the test temperature. After deformation to fracture, the sample was quenched to room temperature by compressed helium gas. The test temperature is shown for each simulation with its cooling rate profile in figure 4.14. As mentioned earlier in section 2.2, the cooling profile for all ferritic stainless steels (at Columbus Stainless) is identical and, therefore the cooling profile in figure 4.14 below, which is for type 412, is also applicable to 3CR12 (type 412 steel is titanium stabilised 3CR12)[26]. The entire heat treatment cycle on the Gleeble 1500 is shown in a schematic figure 4.15.
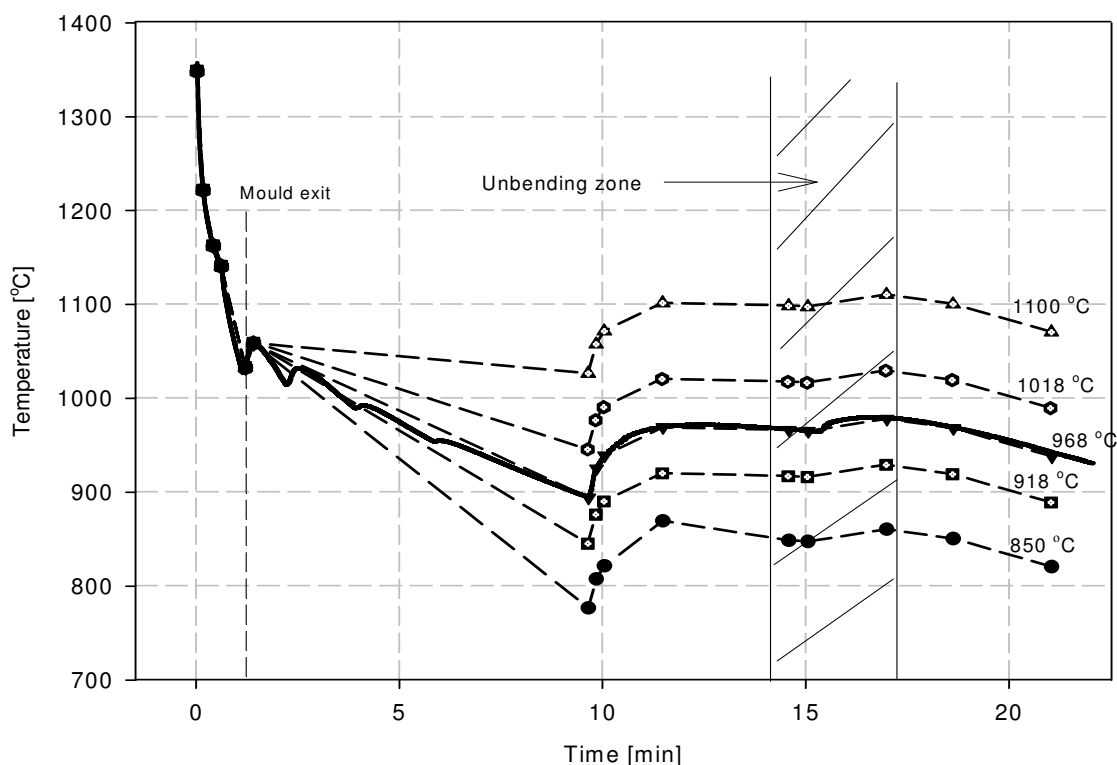
Figure 4.14 - Simulation of modelled strand temperature along the bow-type caster for type 412 steel. The modelled surface temperature is in solid line while the simulated Gleeble cooling curves are in dashed lines.

University of Pretoria – Siyasiya C. W. (2004)
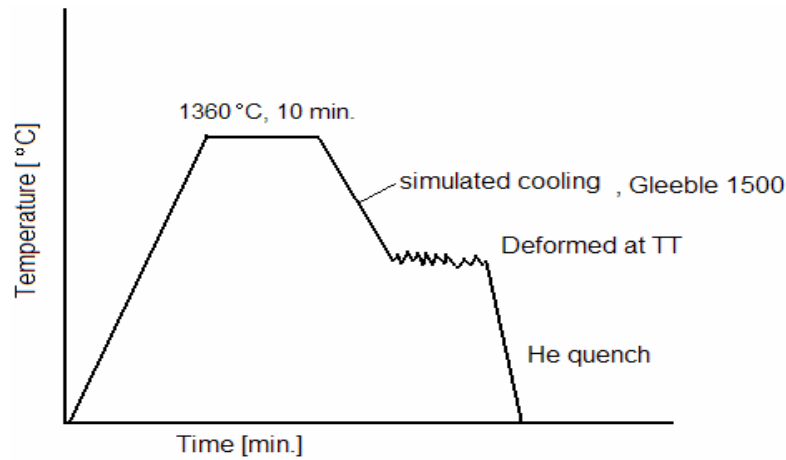**Experimental procedures**

_____

Figure 4.15 - The heat treatment cycle for the Gleeble 1500 and, TT stands for test temperature

While one set of samples was deformed to fracture (to test hot ductility), the other was deformed to just before necking and up to a strain equal to the deformation experienced during straightening, thus, 11.1 x10^{-3} (as calculated below in section 4.2.3). The metallographic results from the samples that were deformed to a strain of 11.1 x10^{-3} were used to assess the influence of deformation on the δ-ferrite to austenite phase transformation by comparing the results with the deformation-free specimens that were given a furnace treatment.

4.2.3 Estimation of the strain rate during straightening

Equations 3.2(a) and 3.4(a) in section 3.1 were applied in the estimation of the strain rate experienced during the straightening process. Details of the continuous caster are as follows: the average casting speed V is 1.01 m/min (0.0168 m/s), the radius of curvature R is 9.01177 m, the strand thickness b is 0.2 m, unbending starts at 14.677 m and ends at 18.721 m.

Hence the unbending strain is given by:

$$e = \left[\frac{0.2}{2 \times 9.01177}\right] = 11.1 \times 10^{-3} \qquad (4.2)$$

_____

And therefore using equation 3.4, the strain rate becomes:

$$\overset{\bullet}{e} = \left[\frac{11.1\times10^{-3}\times0.0168}{(18.721-14.677)}\right] = \mathbf{4.62\times10^{-5}\,s^{-1}} \qquad (4.3)$$

and, therefore, applying equation 3.4(b), the true strain rate during unbending is practically the same:

$$\overset{\bullet}{\varepsilon} = \ln\left[1 + 4.62\times10^{-5}\right] = \mathbf{4.62\times10^{-5}\,s^{-1}} \qquad (4.4)$$

The strain rate that was applied in the hot ductility experiments was an order of magnitude higher (2.1 x10^{-4} s^{-1}), otherwise, the time to deform the specimen to fracture in the Gleeble would have been unrealistically long and, therefore, not a reflection of the straightening process that lasts for an average of four minutes in the continuous caster.

4.2.4 Estimation of the strain rate during side bulging

It has been assumed that side wall bulging takes place at high temperatures where the solidified shell is still thin, implying that it takes place one to two metres after the strand has exited from the mould. From the detailed analysis in appendix 3, an average strain rate of 1.68 x10^{-4} s^{-1} has been estimated for the strain rate during side bulging. This is about four times faster than the unbending strain rate and almost the same order of magnitude as the Gleeble strain rate (2.1 x10^{-4} s^{-1}).

University of Pretoria – Siyasiya C. W. (2004)

Chapter 5

Results and Discussion

_____

5.1 The phase distribution in an as-cast 3CR12 slab

At room temperature, 3CR12 is a dual phase martensite-ferrite stainless steel. The ratio of ferrite to martensite is dependent on the cooling rate and chemical composition. Figures 5.1 (a) and (b), are micrographs for two specimens, one taken from the surface and the other from the centre of the as-cast slab respectively. As may be seen, the surface areas of the as-cast slab have a higher volume fraction of martensite than the centre. This is simply because the surface cools faster than the centre and, therefore, austenite is not given enough time to transform to ferrite. As will be seen from the CCT diagram in figure 5.3 below, the faster cooling rates produce more undercooling and, as a result, there is a higher driving force for the nucleation of austenite from the δ-ferrite. Previous studies revealed that if the cooling rate is slow enough, the austenite transforms completely to α-ferrite plus carbides[4].

(a)   (b)
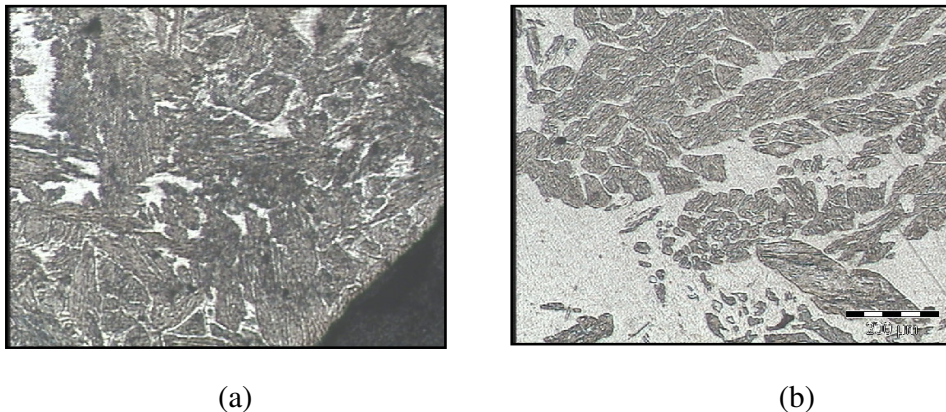
Figure 5.1 - The as-cast microstructure for a slab of 3CR12 (a) at the surface and (b) in the interior (centre). The dark phase is martensite and the light phase is ferrite

As observed in previous work[8], the transformation of austenite to α-ferrite is not only influenced by cooling rate but also by the pre-existing δ-ferrite. The retention of a higher volume fraction of δ-ferrite (particularly at the centre of the slab) also increases the room temperature α-ferrite volume fraction in the steel. It is with this regard that the δ-ferrite to austenite phase transformation influences the room temperature microstructure.

The phase analysis, traversing the entire width of the as-cast slab, revealed that there is a phase distribution profile from the left side to the right side of the slab, figure 5.2 (a). This is

University of Pretoria – Siyasiya C. W. (2004)
Results and Discussion

_____

not surprising because the phase distribution is dependent on the cooling rate which in-turn is dependent on the rate of heat transfer both during primary and secondary cooling (in the mould and after exiting from the mould respectively). Uneven heat transfer is caused by non-uniform mould powder infiltration, blocked water spray nozzles, variations in casting speed and mould taper angle[25], among other reasons.
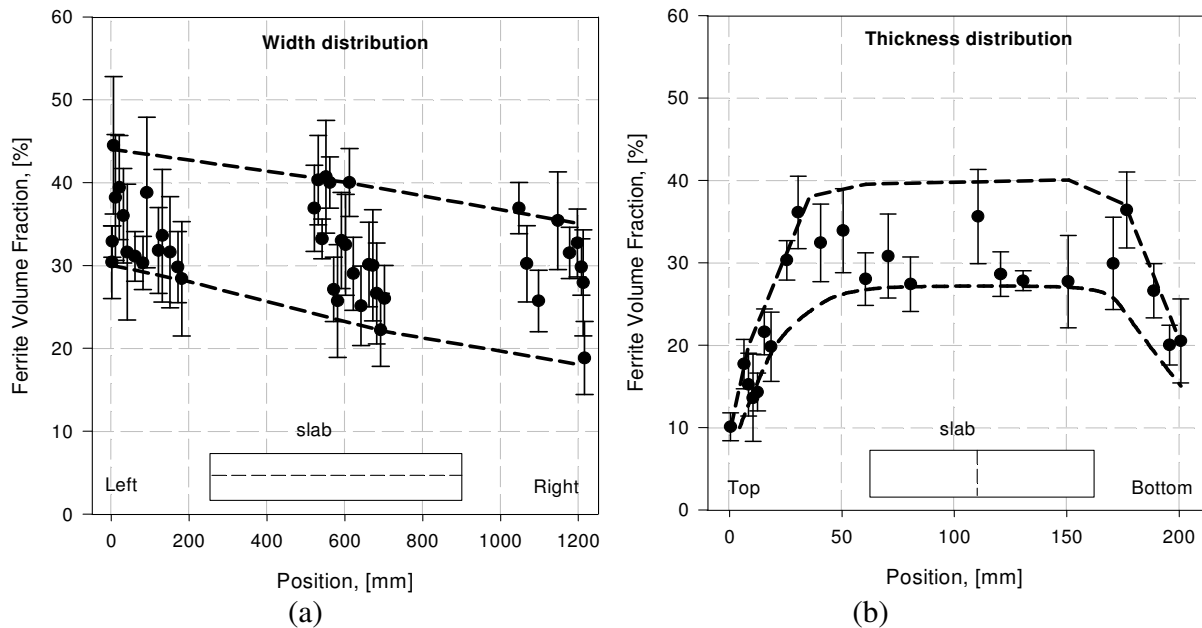

Figure 5.2 - (a) As-cast ferrite volume fraction measured across the width at half-thickness and (b) measured across the thickness and at half-width of the slab for heat number 3373793. Ferrite factor = 11.04

Figure 5.2 (a) shows a higher volume fraction of ferrite on the left hand side of the slab than on the right. The dimensions for the side bulging and gutters are presented in table 5.1 for the three slabs of 3CR12 from Columbus. Side bulging occurred more on the left of the thickness face i.e. the side with a higher volume fraction of ferrite. This observation must be interpreted with caution because the room temperature microstructure of the as-cast slab is also dependent on the decomposition of austenite to α-ferrite and martensite rather than only the high temperature transformation of δ-ferrite to austenite. The slab exits from the caster at a temperature range of 800-900 ˚C and, therefore, the austenite to α-ferrite and martensite phase transformation occurs through air cooling. Depending on how high the slabs are stacked, it may take 16 to 24 hours for the slabs to cool down to room temperature[26].

University of Pretoria – Siyasiya C. W. (2004)
Results and Discussion
_____

Heat No.	Side bulge, left (mm)	Side bulge, right (mm)	Top gutter (mm), left	Bottom gutter (mm), left
3373803	1.1	-	0	1.25
3412413	7.0	1.0	1.5	0
3412423	6.5	1.0	1.25	0
3373793	4.3	1.0	0	0

Table 5.1 - The side bulge and off-corner depression measurement taken from the as-cast slabs received from Columbus

Side bulging is discussed in detail in sections 5.7 to 5.11 below.

Unlike the top and bottom of the slab, figure 5.2 (b), the ferrite volume fraction of the thickness faces in figure 5.2 (a) is not different from that of the centre of the slab. This is attributed to the cooling pattern during secondary cooling because the water is sprayed onto both the top and bottom of the wider faces of the strand during the early part of the process but none onto the thickness faces. Furthermore, there is also heat transfer through conduction between the guide rolls on both the top and bottom of the slab. Hence, there is more heat extraction on the wider faces than on the thickness faces. This may explain the reason why there is a lower volume fraction of ferrite on the top and bottom of the slab than on the thickness faces. In-other-words, the thickness faces of the strand are cooled slowly and, therefore, there is less driving force for the nucleation of austenite due to less undercooling and the slow cooling rate allows more regression of austenite to ferrite. Consequently, there is more ferrite on the surface of the thickness faces than in the top and bottom surfaces of the slab. Figure 5.2 (b) above, shows that there is less ferrite on the top surface than the bottom surface of the slab. This is because once the strand enters the unbending zone, water is only sprayed from the top and, therefore, there is a temperature difference with the bottom surface

University of Pretoria – Siyasiya C. W. (2004)
Results and Discussion
_____

being at a higher temperature than the top. Unfortunately, there is no device installed to measure the temperature difference between the top and bottom surfaces of the strand. Nevertheless, it can be deduced from the higher volume fraction of ferrite on the bottom surface that more δ-ferrite is retained from the higher bottom temperature than on the top surface. This may explain the reason why there is a difference in ferrite volume fraction between the top and bottom surfaces of the strand.

The influence of constitutional supercooling (when the solid freezes with a composition different from that of the liquid from which it forms) on the high temperature δ-ferrite to austenite phase change was also examined. According to the iron-chromium phase diagram in figure 1.1 in section 1.2, the solidus and liquidus temperatures at 11 to 12%Cr, are almost the same, i.e. the partition coefficient k is almost one, where k is defined as the ratio of the solute concentration in the freezing solid, C_S, to that in the main body of the liquid, C_L. Figure 5.3 shows a spectroscopy analysis from the SEM of the distribution of chromium and other alloying elements from the edge of the slab extending inwards for 700 μm. As may be seen, the chromium is almost uniformly distributed from the surface (side wall edge) into the interior of the as-cast slab. This signifies that the first material to solidify was not depleted in chromium, i.e. the partition coefficient is almost one. This suggests that there is not significant constitutional supercooling during the solidification of 3CR12. It may, therefore, be concluded that the δ-ferrite to austenite in the first material to solidify is mainly influenced by the macro chemical composition of the strand and the cooling rate rather than any localised effects arising from constitutional supercooling.

Once again, it is important to note that the room temperature microstructure is dependent on the cooling rate during the subsequent decomposition of the austenite and the pre-existing δ-ferrite in the steel. It is also worth noting that the as-cast microstructure is merely an intermediate stage during steel production and, therefore, it may not have a significant bearing on the final microstructure after hot rolling and annealing.
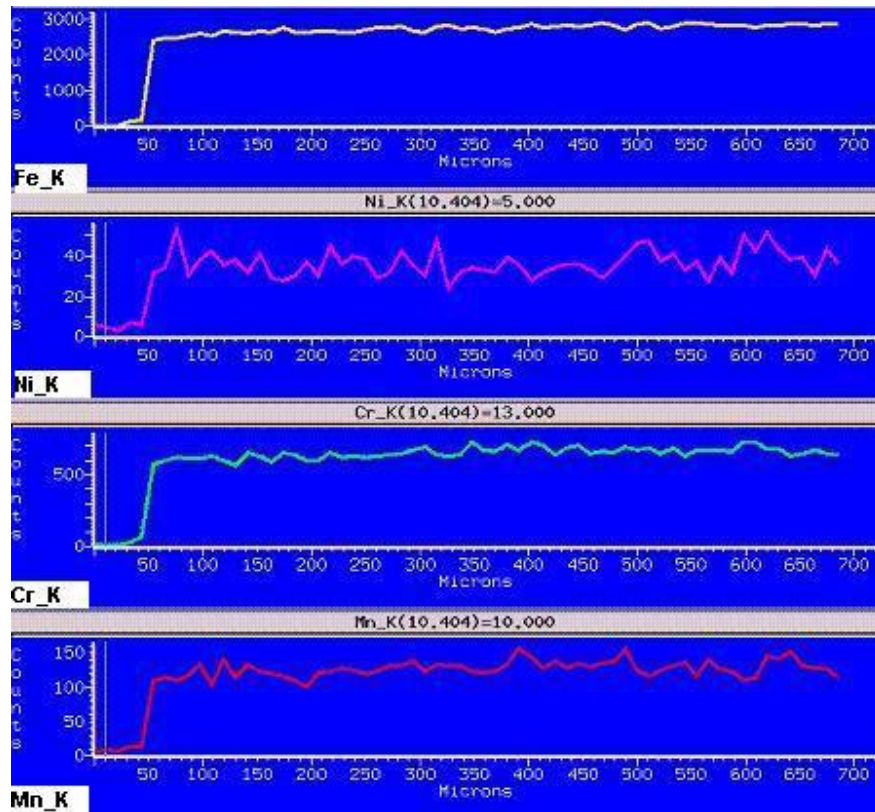
University of Pretoria – Siyasiya C. W. (2004)
Results and Discussion
_____

Figure 5.3 - Spectroscopy analysis showing the distribution of the major alloying elements from the surface (side wall edge) into the interior of the as-cast slab taken at half-thickness


5.2 Width variation during continuous casting of 3CR12

During continuous casting, the strand width measurement is done when the strand is exiting from the continuous caster in the temperature range of 800-950 ˚C, figure 5 (a). A ferrite-austenite dual phase steel is expected within this temperature range. Therefore, the width variation from slab to slab may be ascribed to the ratio of ferrite to austenite that varies with chemical composition and cooling rate, see table 1 in appendix1. This is simply because of the differences in lattice structure between the two i.e. the "loosely packed" ferrite (BCC) occupies more volume than the "closely packed" austenite (FCC). As may be seen from figure 1.6 in section 1.3.1, the difference in density between BCC-iron and FCC-iron is the highest within this temperature range. As expected, a higher volume fraction of ferrite would be accompanied with a wider strand width at the exit from the caster. The remedy to this problem would be a stricter control of chemical composition within the limits.

University of Pretoria – Siyasiya C. W. (2004)
Results and Discussion
_____
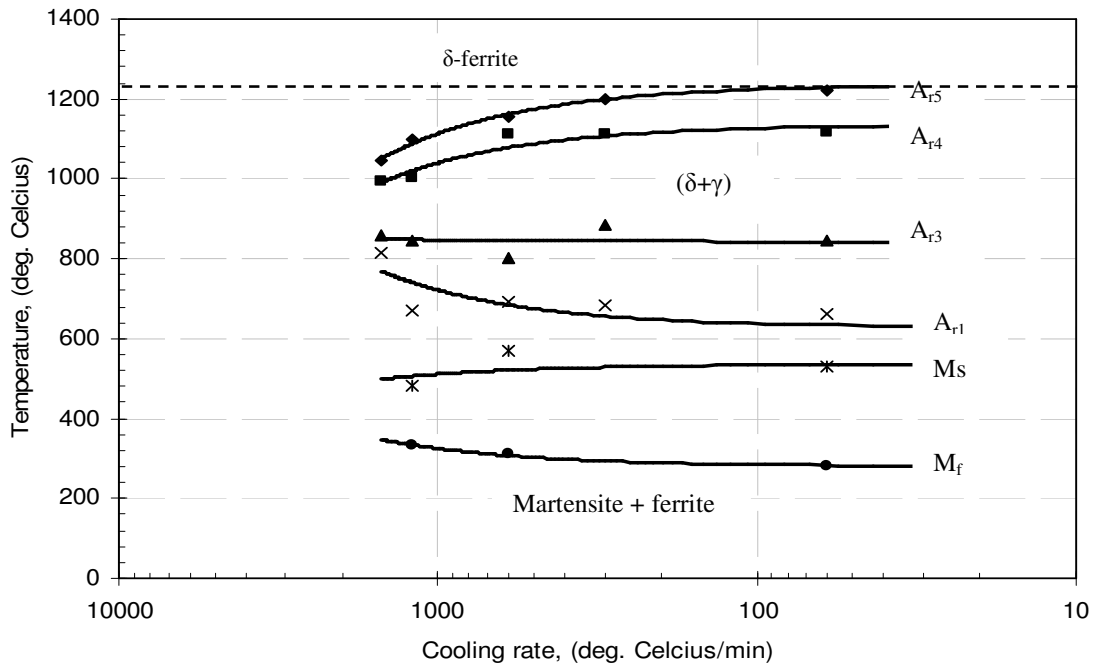
(a)
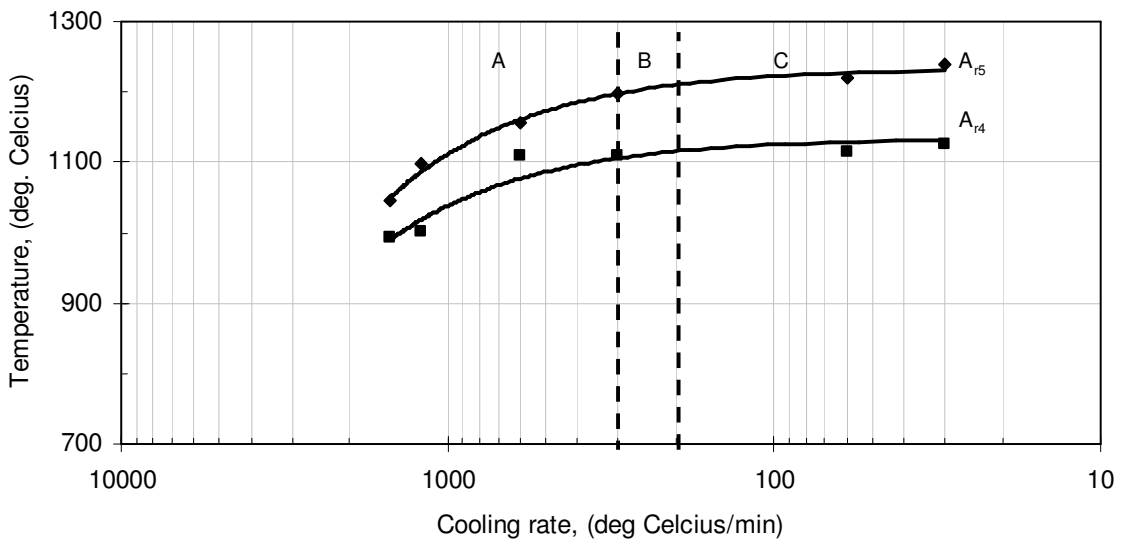
(b)

Figure 5.4 - (a) Continuous cooling transformation diagram for 3CR12, heat (3287232). (b) Typical surface cooling rates: A = primary cooling, B = secondary cooling. Region C is for interior of the slab.

University of Pretoria – Siyasiya C. W. (2004)
Results and Discussion

_____

5.3 Continuous cooling and isothermal phase transformation of δ-ferrite to austenite

Figure 5.4 (a) shows the experimentally determined continuous cooling transformation (CCT) diagram. It is evident that at cooling rates greater than 60 ˚C/min, the δ-ferrite to austenite phase transformation becomes more sensitive to cooling rate. This suggests that during continuous casting of 3CR12, the δ-ferrite to austenite transformation start temperature is lower on the surface of the strand than at the centre of the strand. According to the modelled surface temperature, the strand exits from the mould at a surface temperature of about 1100 ˚C. Therefore, at a cooling rate of 200 to 300 ˚C/min (which is typical for the secondary cooling rate), the δ-ferrite would have already started transforming to austenite i.e. the outer part of the solidified shell would be δ-ferrite plus austenite while the inner part next to the mushy zone would be completely δ-ferrite due to the existence of the temperature gradient across the solidification shell thickness.

As mentioned earlier, the surface of the strand cools faster than the centre. However, through controlled secondary cooling, the surface temperature is maintained within the temperature range of 900-1000 ˚C until completion of straightening. During this time, the δ-ferrite transforms isothermally to austenite. When the slab exits form the caster, the austenite that is on the surface fully transforms to martensite through air cooling. In brief, the higher volume fraction of martensite in the surface region is attributed to:

- Higher undercooling and, therefore higher driving force for the nucleation of austenite.

- The isothermal transformation of δ-ferrite to austenite allows more δ-ferrite to transform to austenite.

- Faster cooling rates that lead to austenite fully transforming to martensite.

Unlike the surface, the centre cools slowly, there is less driving force for the nucleation of austenite and, therefore, more δ-ferrite is retained which in-turn accelerates the austenite to α-ferrite phase transformation. Furthermore, the slow cooling rate means there is more time for the austenite to regress to ferrite. This may explain why there is a higher volume fraction of ferrite at the centre of the slab at room temperature.

University of Pretoria – Siyasiya C. W. (2004)
Results and Discussion

_____

5.4 Effect of chemical composition on the austenite start temperature A_{r5}

Three chemical compositions of 3CR12 with ferrite factors 9.6, 11.5 and 12.1 (see table 4.1 above) were examined for the austenite start temperature during continuous cooling within a cooling rate range of 1500 to 30 ˚C/min and the results are given in figure 5.5.

From figure 5.5, it appears that there is a trend that austenite transformation from the δ-ferrite starts at earlier times as the ferrite factor decreases i.e. as the quantity of austenite formers in the steel's composition increases. In fact, the austenite formers do not only shift the transformation temperature to earlier times but raise it as well.
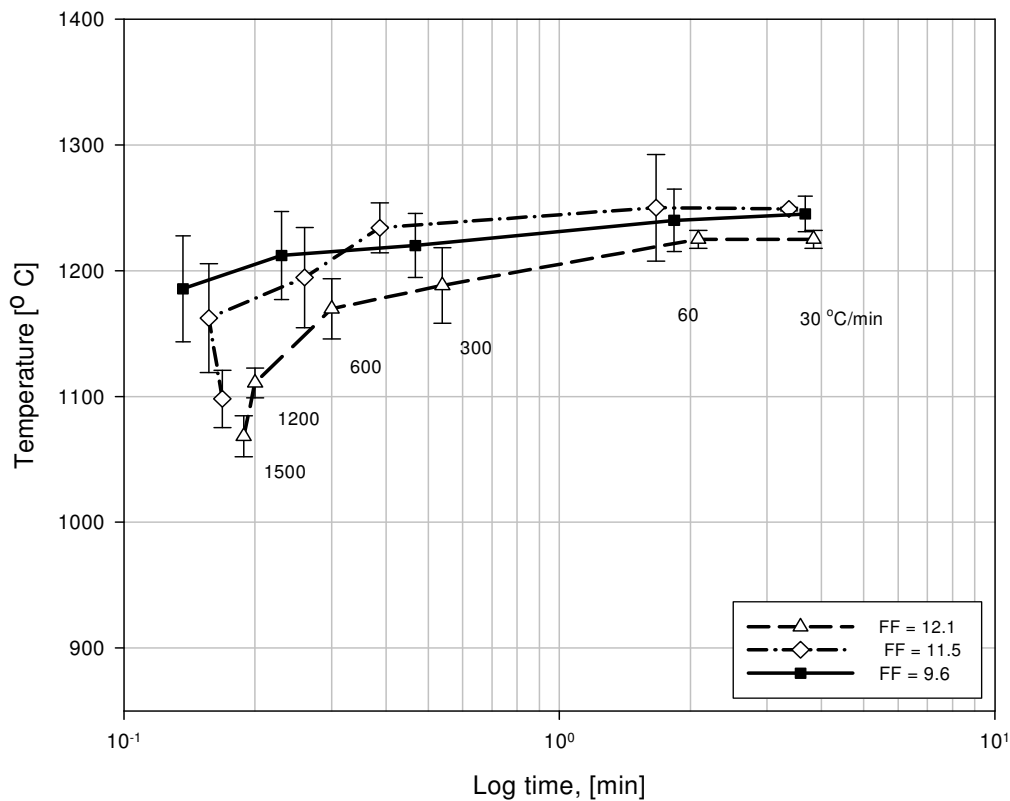
Figure 5.5 - Influence of chemical composition on the measured austenite start temperature A_{r5} for 3CR12 steels with ferrite factors of 12.1, 11.5, and 9.6

Previous studies on the influence of carbon and nitrogen on the γ-loop of the iron-chromium equilibrium phase diagram, showed that austenite formers have a tendency to raise the austenite start temperature[2]. Therefore, the results in figure 5.5 support this observation.

- 56 -

University of Pretoria – Siyasiya C. W. (2004)
Results and Discussion

_____

Figure 5.6 has been derived from figure 5.5 above by plotting the austenite start temperature against the ferrite factor at the fastest (1500 ˚C/min) and slowest (30 ˚C/min) cooling rates. It is clearly evident that for both cooling rates the austenite-start temperature increases with increasing austenite formers i.e. with decreasing ferrite factor. The difference between the two curves in figure 5.6 below is that from the CCT diagram in figure 5.5, the faster cooling rate produces higher under-cooling for the austenite to α-ferrite transformation. Hence, the austenite start temperature for the surface of the strand is lower than that of the centre.

One limitation with the weld simulator is that at slower cooling rates, less than 60˚C/min, oxidation interferes with the resistivity measurement and therefore renders the results suspect. Hence, it was essential that these results, particularly for slower cooling rates, should be verified through metallographic analysis. This was achieved by controlled furnace cooling. Figures 5.7 and 5.8 below show the microstructure of the two chemical compositions with ferrite factors of 9.6 and 12.1 after cooling at 1 ˚C/min to 1230 ˚C and quenched into water.
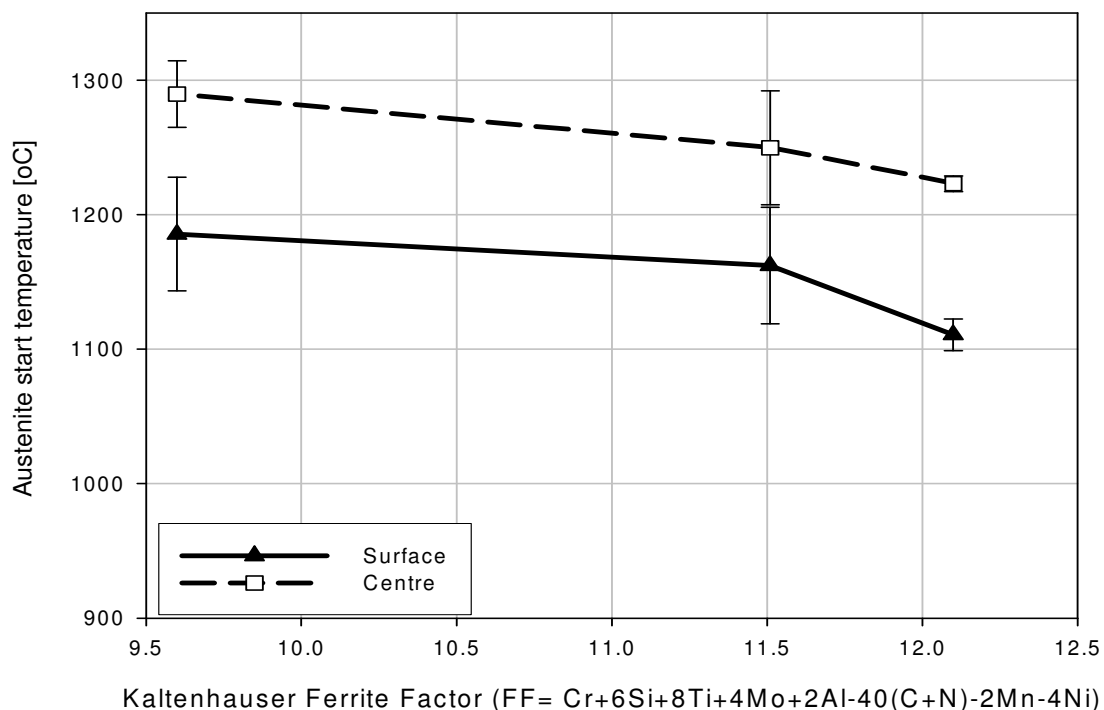

Figure 5.6 - The variation of austenite start temperature with chemical composition, expressed as a Kaltenhauser ferrite factor

University of Pretoria – Siyasiya C. W. (2004)
Results and Discussion
_____

The set of microstructure in figure 5.7 show that at 1230 ˚C, the steel with the lower ferrite factor of 9.64 in micrograph (a) had already started to transform from δ-ferrite to austenite as opposed to one with higher ferrite factor of 12.1 in micrograph (b).

(a)   (b)
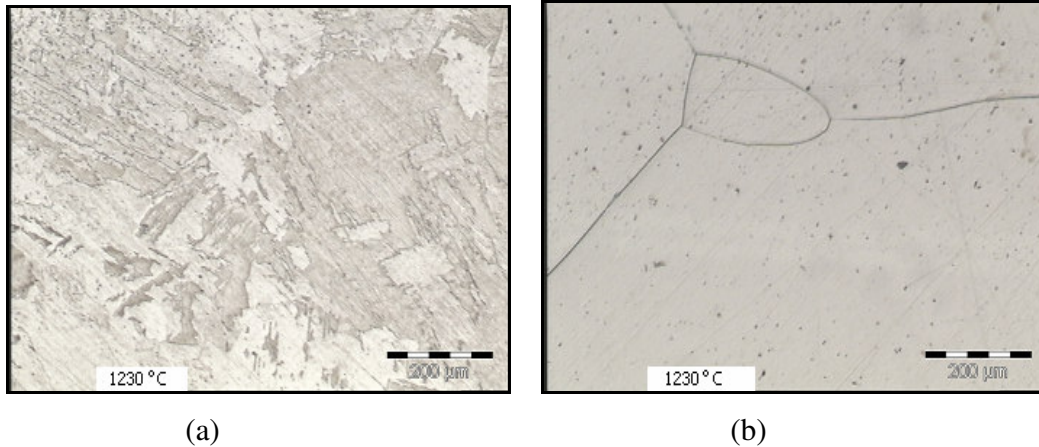
Figure 5.7 - Micrographs for furnace heat treated samples (a) FF=9.64, (b) FF=12.1, solution treated at 1350 °C, soaked for 30minutes, cooled at 1°C/minute and quenched in water from 1230 °C. Magnification x5

(a)   (b)
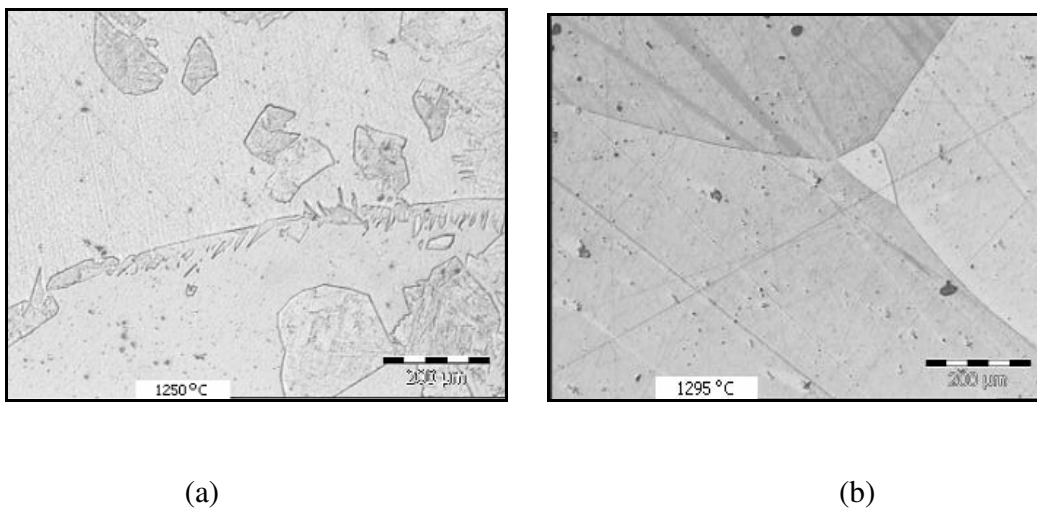
Figure 5.8 - Micrographs for furnace heat treated samples, FF=9.64, solution treated at 1350 °C, soaked for 30 minutes, cooled at 1°C/minute and quenched (a) from 1250 °C, (b) from 1295 °C. Magnification x5

The samples with a lower ferrite factor were heated to 1350˚C, cooled at 1˚C/min and one was quenched from 1250 ˚C while the other from 1295 ˚C. The results are shown in figures 5.8 (a) and (b) above. As may be seen, at 1250 ˚C, widmanstätten austenite nucleated

- 58 -

University of Pretoria – Siyasiya C. W. (2004)
Results and Discussion

_____

and grew from the δ-ferrite grain boundaries in figure 5.8 (a) while at 1295 ˚C, the steel was fully ferritic and no δ-ferrite had started transforming to austenite.
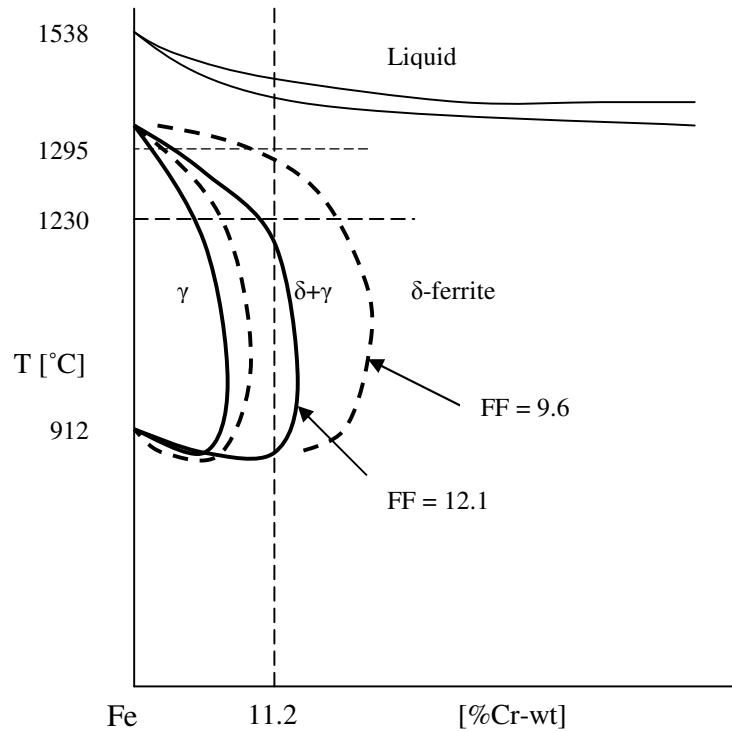
Figure 5.9 - Schematic presentation of the influence of chemical composition, particularly austenite formers (C, N, Ni and Mn), on the austenite start temperature in 3CR12

This suggests that the austenite start-temperature for this chemical composition with relatively low ferrite factor of 9.64 is somewhere between 1250 ˚C and 1295 ˚C, i.e. somewhat higher than that of the sample in figure 5.7 (b) with a ferrite factor of 12.1. This observation is in agreement with the theory that ferrite formers stabilize the high temperature δ-ferrite. Figure 5.9 is the schematic presentation of the influence of chemical composition on the austenite start temperature at equilibrium.

5.5 The hot ductility behaviour of 3CR12

The as-cast 3CR12 with the following chemical composition Fe-0.014C-0.0155N-0.4Ni-0.65Mn-11.28Cr-0.65Si-0.025Ti-0.08V and a ferrite factor of 11.36 was reheated to 1360 ˚C

University of Pretoria – Siyasiya C. W. (2004)
Results and Discussion

_____

and soaked for 10 minutes before being cooled to the tensile test temperature in the Gleeble, simulating the cooling profile during straightening in the continuous caster. The hot ductility characteristic curves for this steel under these conditions are given in figure 5.10.
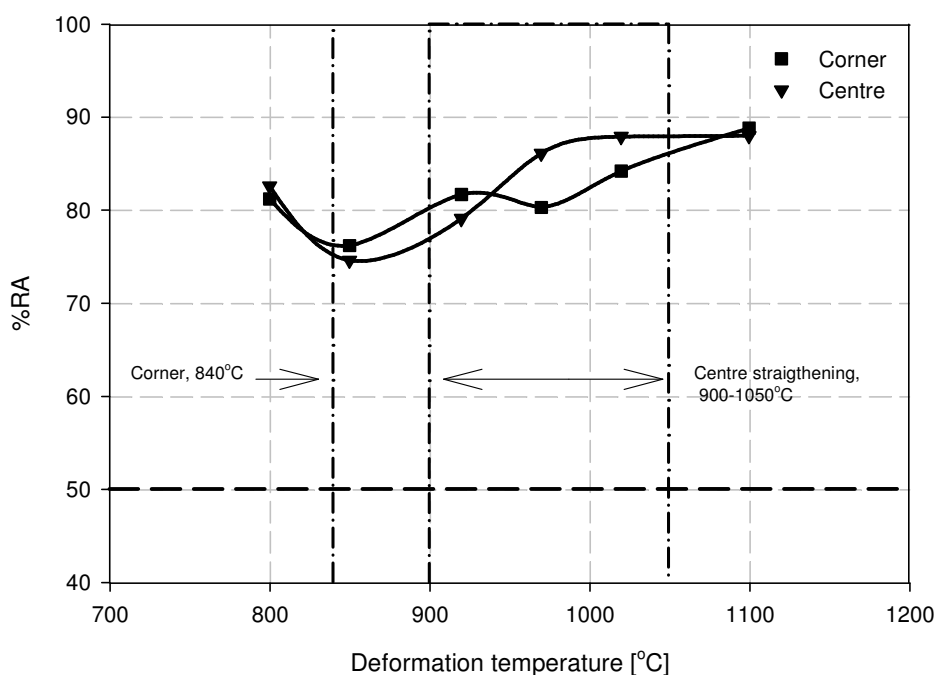
Figure 5.10 - The hot ductility characteristic curves for 3CR12, heat number 3412423, ferrite factor of 11.36

The results show that 3CR12 has good hot ductility with a minimum percentage reduction in area (%RA) of 75% at all of the deformation temperatures tested. Figure 5.11 below is a photograph of the fractured samples exhibiting a typical ductile fracture in all cases. There is no transverse cracking problem experienced during the continuous casting of 3CR12 and this may be attributed to its good hot ductility, with the ductility trough lying well above the 50% reduction in area limit. Figures 5.12 (a) and (b) are the optical micrographs of the necking region, sectioned along the tensile stress axis, showing elongated ferrite phase (light phase).

5.6 Strain and strain rate in the necking region
As already indicated earlier in section 4.2.3, the average engineering strain and strain rate during straightening in the continuous casting of 3CR12, are 11.1 x10^{-3} and 4.62 x10^{-5} s^{-1}

University of Pretoria – Siyasiya C. W. (2004)
Results and Discussion
_____
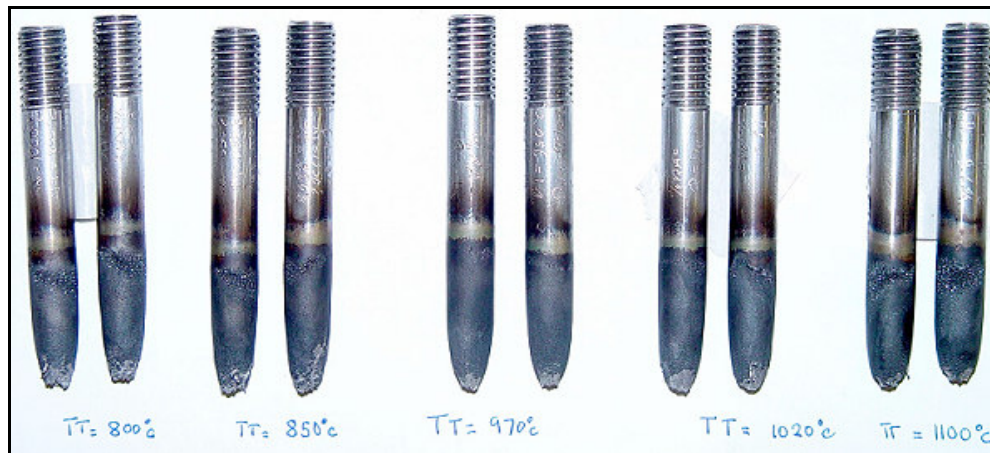
Figure 5.11 - Ductile fracture of the test samples for 3CR12, FF = 11.362

(a)   (b)
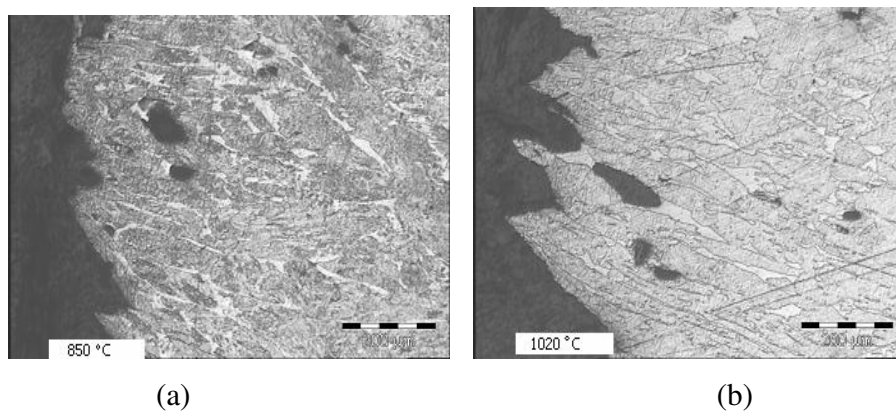
Figure 5.12 - Typical ductile fracture surfaces (a) at 850 °C and (b) at 1020 °C, for heat 3412324, x5 magnification

respectively. The actual strain rate that was used in the experiment was an order of magnitude higher, i.e. 2.1 $x10^{-4}$ s^{-1}. The experiment would otherwise have been unrealistically long during deformation to fracture which is not a realistic simulation of the straightening process during the continuous casting process that lasts only for an average of four minutes in the case of 3CR12 and other ferritic steels. The difference here, of course, lies in the large strain to fracture in the Gleeble compared to only a limited strain within the continuous caster.

University of Pretoria – Siyasiya C. W. (2004)
Results and Discussion

_____

The percentage reduction in area (%RA) has been found to be extremely useful in assessing the hot ductility characteristics of a material during continuous casting[17]. However, if the strain and strain rate are not constant when necking commences, it is noteworthy to interpret the results with caution since the strain and strain rate may be some magnitude higher than the set strain rate. Figures 5.13 (a) and (b) is the average necking strain and strain rate estimated from the hot ductility results respectively. The average necking strain ε_n has been computed from:

$$\varepsilon_n = \ln\left[\frac{A_u}{A_f}\right] \qquad\qquad (5.1)$$

where A_u and A_f are the uniform and fractured cross sectional areas.

Figure 5.13 (a) shows how the average necking strain varies with temperature. In a way, the necking strain is another measure of hot ductility since ε_n is a function of the inverse of the fractured cross sectional area A_f.
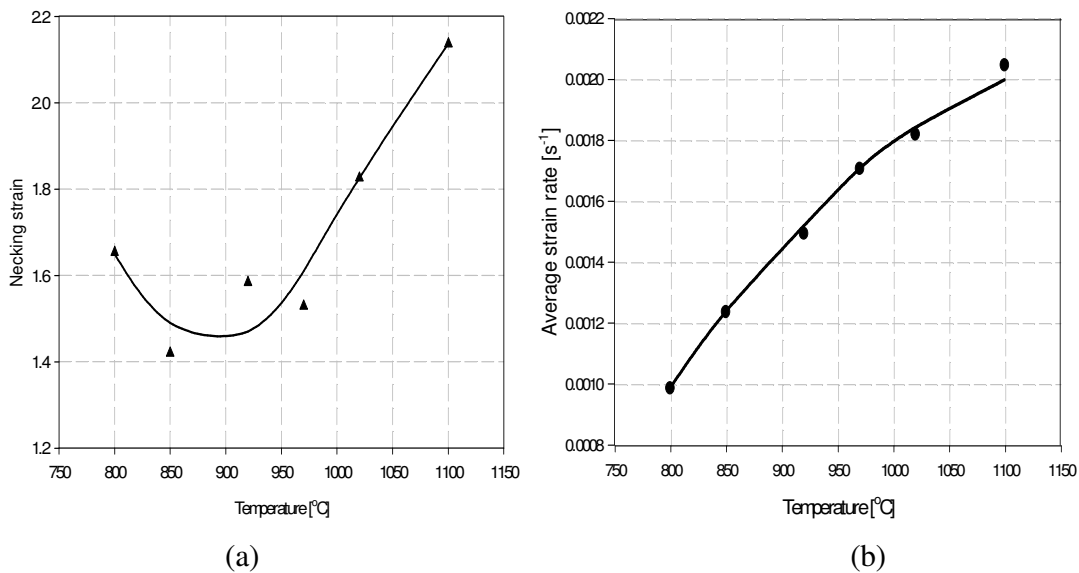

(a)   (b)

Figure 5.13 - (a) The average necking strain, (b) the average strain rate in the necking region during deformation at high temperature. The set strain rate was 2.1×10^{-4} s^{-1}.

When necking commences, a constant strain rate can only be achieved as deformation progresses by monitoring the thinning cross sectional area of the sample through a closed

University of Pretoria – Siyasiya C. W. (2004)
Results and Discussion

_____

loop system of the Gleeble. A previous study by Prozzi[9] revealed that both the strain (up to 0.9) and strain rate (> 0.1 s^{-1}) do not influence the austenite to ferrite transformation of the dual phase 3CR12 significantly and, therefore, for this study, it was not necessary to control the strain rate since the applied strain rate in the Gleeble was well below 0.1 s^{-1} by three orders of magnitude (2.1 x10^{-4} s^{-1}). However, it was worthwhile estimating the magnitude of the strain rate involved during necking. G'Sell et al[27] found that for a constant strain rate $\dot{\varepsilon}_n$:

$$\dot{\varepsilon}_n = -\ln\left[\frac{A}{A_o}\right] \times \left[\frac{1}{t}\right] \qquad\qquad (5.2)$$

where A_o and A are the original and instantaneous cross sectional areas of the sample respectively and t is the time in seconds to deform the sample from A_o to A.

Figure 5.13 (b) above shows that the average necking strain rate increases with an increase in temperature and, at fracture, it is a magnitude higher than the set strain rate of 2.1 x10^{-4} s^{-1}. It can, therefore, be concluded that both the strain and strain rate in the necking region, were below the range that would influence the kinetics of the austenite to ferrite transformation during the isothermal deformation of 3CR12 at high temperature[9].

5.7 Microstructure of the undeformed and deformed samples

The microstructure of the same steel that was used to study the hot ductility was examined metallographically after furnace heat treatment (deformation free) and hot deformation (on the Gleeble). The results are given in figures 5.14 and 5.15 below. The austenite volume fraction was analysed from the martensite present using the software program (analySIS) and the results are plotted as austenite volume fraction versus temperature in figure 5.16 below.

Both figures 5.14 and 5.15 show that the austenite volume fraction increases as the temperature decreases from 1200˚C and 1180˚C respectively reaching a maximum volume fraction at 1020˚C. This is a typical behaviour of 11-12%Cr steels. They transform from a fully δ-ferritic steel at high temperature to a δ-ferrite-austenite dual phase steel as the temperature decreases below the austenite start temperature.

University of Pretoria – Siyasiya C. W. (2004)
Results and Discussion

_____
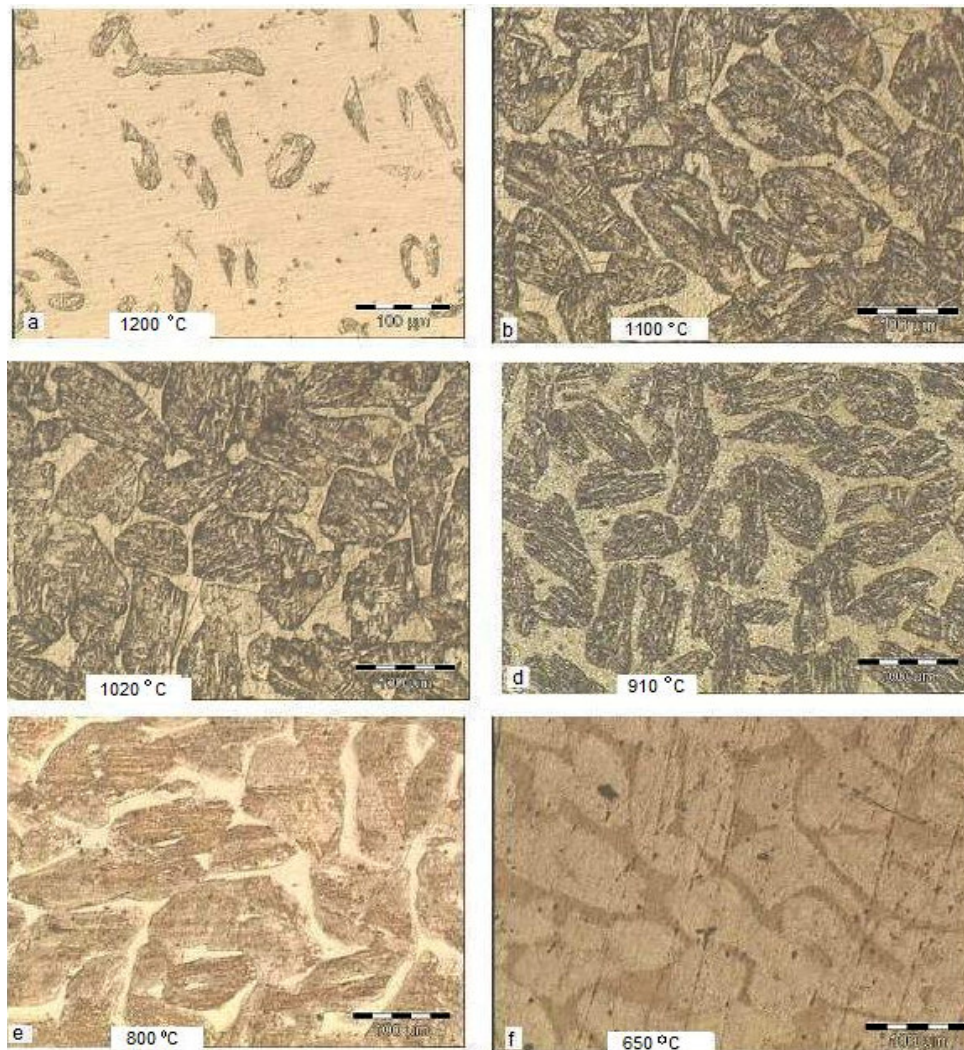
Figure 5.14 - Micrograph for heat 3412423, deformation-free specimens, furnace cooled from 1350 ˚C at 1 ˚C/min and water quenched from 1200, 1100, 1020, 910, 800 and 650˚C. For (a) to (e), the dark phase is martensite and the light phase ferrite, and (f) is δ-ferrite plus α-ferrite at 650˚C (the lighter phase). Magnification x10.

- 64 -

University of Pretoria – Siyasiya C. W. (2004)
Results and Discussion
_____
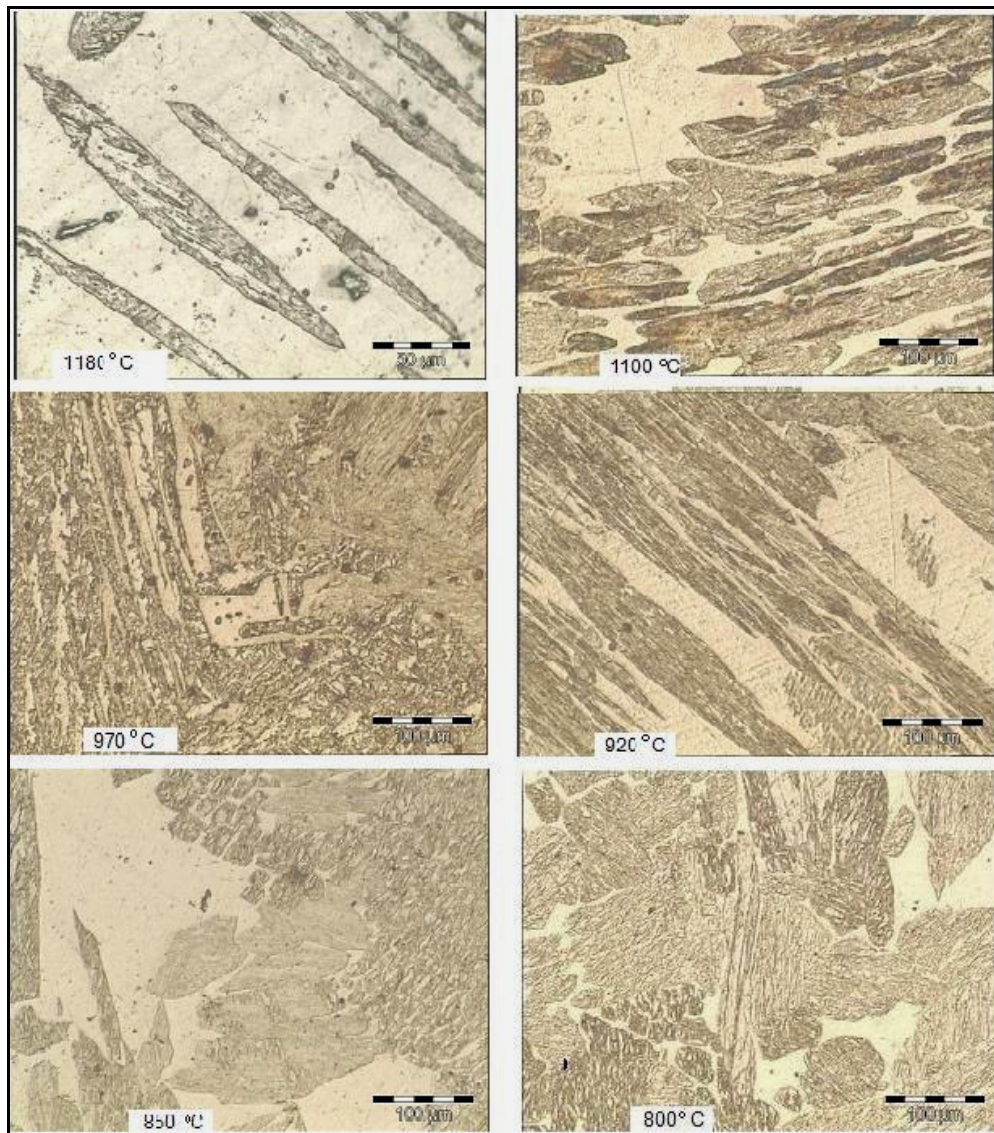
Figure 5.15 - Micrograph for heat 3412423, Gleeble cooled from 1360 ˚C simulating continuous casting, deformed to necking at 1180, 1100, 970, 920, 850 and 800˚C. The dark phase is martensite and the light phase is ferrite. Magnification x10.
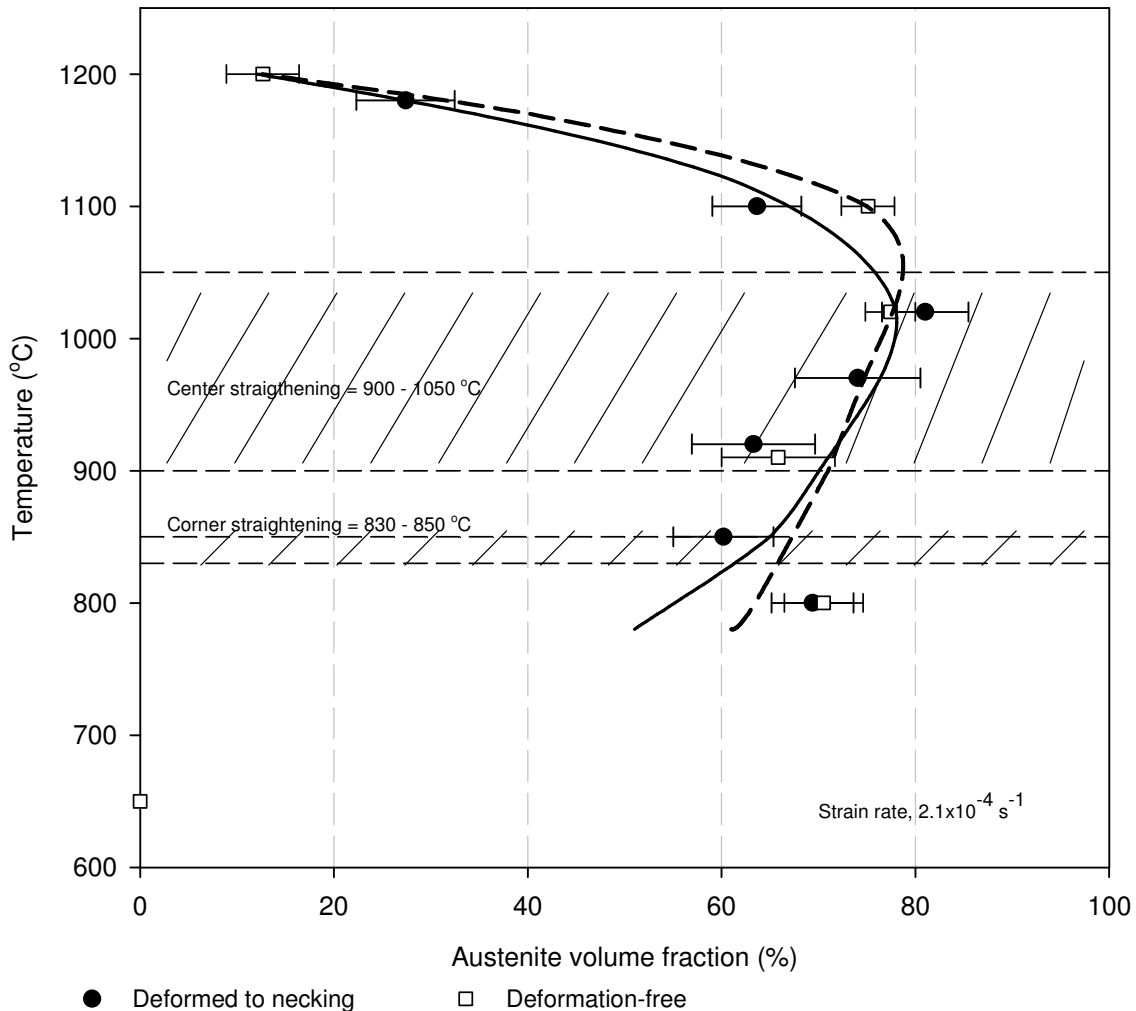
Figure 5.16. The austenite volume fraction for the deformed and deformation-free samples, heat 3412423, ferrite factor of 11.362

The two curves in figure 5.16 above are almost identical and, therefore, this suggests that hot deformation does not influence either the δ-ferrite to austenite or the austenite to α-ferrite phase transformation. In-other-words, the observation that hot deformation does not influence the kinetics of the lower temperature austenite to α-ferrite phase change[9] also holds for the higher temperature δ-ferrite to austenite phase change in 3CR12. These results imply that deformation (in this case straightening) does not cause the formation of deformation-induced ferrite during the continuous casting of 3CR12.

University of Pretoria – Siyasiya C. W. (2004)
Results and Discussion
_____

Extrapolation of the two curves in figure 5.16 to zero austenite volume fraction at the upper end, gives an austenite start temperature of 1230 ˚C and this agrees well with the results in figure 5.6. For a ferrite factor of 11.36, the austenite start temperature on the surface would be about 1160˚C and at the centre at the slowest cooling rates, 1250˚C. As the temperature drops further the austenite volume fraction keeps on increasing until it reaches a maximum of about 80% at 1050 ˚C and, thereafter, it starts decreasing with a further decrease in temperature as the austenite transforms to α-ferrite. This behaviour is in agreement with what was observed in previous studies in 11-12Cr% steels[7,28].

5.8 Influence of microstructure on the hot ductility of 3CR12

The good hot ductility characteristics of 3CR12 can be understood properly through the examination of the microstructure of the deformed and undeformed samples. The ferrite volume fraction within the straightening temperature region at Columbus Stainless is within the range of 20 to 40%, figure 5.16 above. In general (in both the austenitic and ferritic stainless steels), ferrite has good hot ductility properties and is only detrimental when it forms in small amounts as thin films surrounding the austenite grains[20]. The higher volume fraction of ferrite rather than a mere film along the austenite grain boundaries is responsible for the good hot ductility of 3CR12 during continuous casting i.e. there is no strain concentration in the ferrite to cause ductile intergranular failure since the strain is uniformly distributed in the ferrite. Ferrite recovers readily and forms serrated grain boundaries and this, therefore, prevents grain boundary sliding[29]. Cardoso et al[18] observed that for hot ductility to improve significantly in a dual phase steel, the ferrite volume fraction has to approach 40% and 3CR12 seems to meet this condition, at least during the straightening operation in the continuous caster.

Although the results in figure 5.16 suggest a plausible explanation for the good hot ductility of 3CR12, it is worth noting that reheating the as-cast specimens to a high temperature (in this case 1360 ˚C and soaking for 10 minutes) to redissolve the microalloying additions and form a coarse grain structure, destroys and replaces the large columnar grains of an as-cast slab with a finer equiaxed grain structure. Since this problem is not easy to surmount in the laboratory, the hot ductility results should be interpreted with caution. Large columnar grains

University of Pretoria – Siyasiya C. W. (2004)
Results and Discussion

_____

in the thickness direction of the strand are detrimental as the straightening stresses are perpendicular to the longitudinal axis of the columnar grains and this promotes crack propagation[21]. Grain refinement leads to an improvement in hot ductility for both ferritic and austenitic steels since fine grains limit crack propagation, reduce crack aspect ratio and also decrease the precipitate density on the grain boundaries[20]. However, since it was confirmed at the plant (Columbus Stainless) that there are not any transverse cracking problems with 3CR12, it can be concluded that the substantial ($\delta+\alpha$)-ferrite volume fraction (20 to 40%) is responsible for the good hot ductility during continuous casting of this steel.

The highest volume fraction of austenite (about 80%) exists between the temperatures 920 to 1020 ˚C and it appears that the steel undergoes considerable dynamic recrystallisation within this temperature range as the strain hardening (figure 5.17 below) is followed by softening for the 920 and 1020 ˚C curves. This is one of the possible reasons for even better hot ductility within this temperature range despite the lesser volume fraction of ferrite. Since 3CR12 exhibits good hot ductility characteristics it was felt not necessary to study the precipitation of carbides and carbonitrides in detail in this steel.

The hot strength of 3CR12 has been derived from the flow stress curves in figure 5.17 and the peak strength (steady state flow stress) as a function of temperature is plotted in figure 5.18. The peak strength gives an indication of the hot strength of the solidification shell in the side walls (narrow faces) of the strand at a given temperature and, as expected, the strength of the solidification shell increases as the temperature drops.

5.9 The hot strength of 3CR12

Figure 5.17 shows the flow stress curves obtained from the hot ductility tests. This strengthens the argument that side wall bulging is a high temperature phenomenon, i.e. the strand is most vulnerable to side bulging when it is not only thinnest but also weakest in terms of the solidification shell's ability to withstand the ferrostatic pressure from the liquid column of the steel.

University of Pretoria – Siyasiya C. W. (2004)
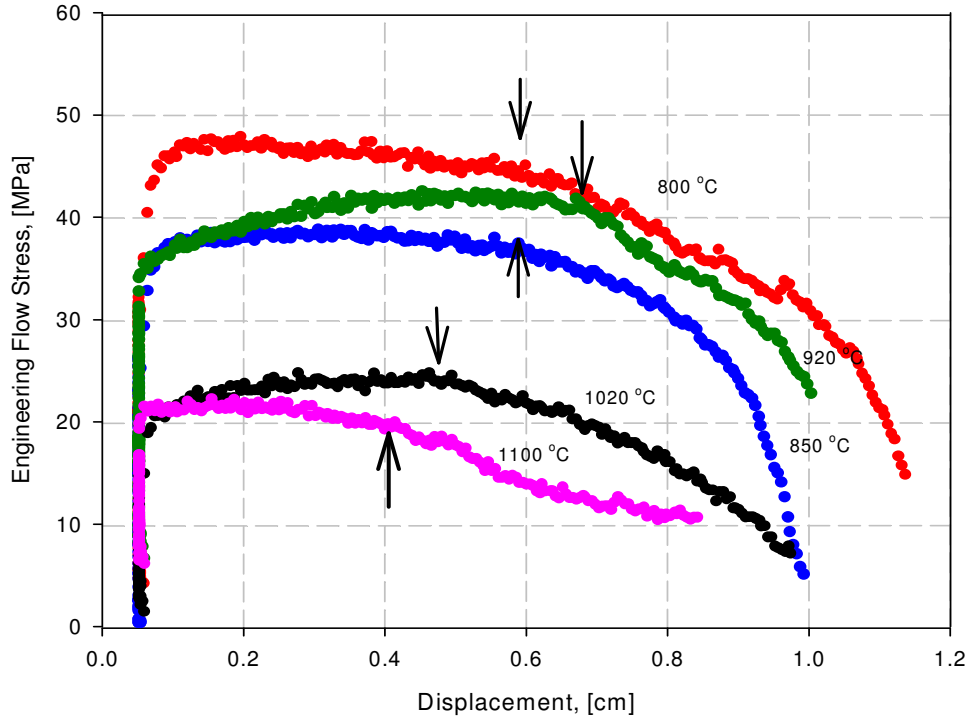**Results and Discussion**

_____

Figure 5.17 - Typical engineering flow stress curves for the hot ductility tests for 3CR12 (heat 3412423) obtained from the Gleeble 1500. The arrows indicate where necking started.
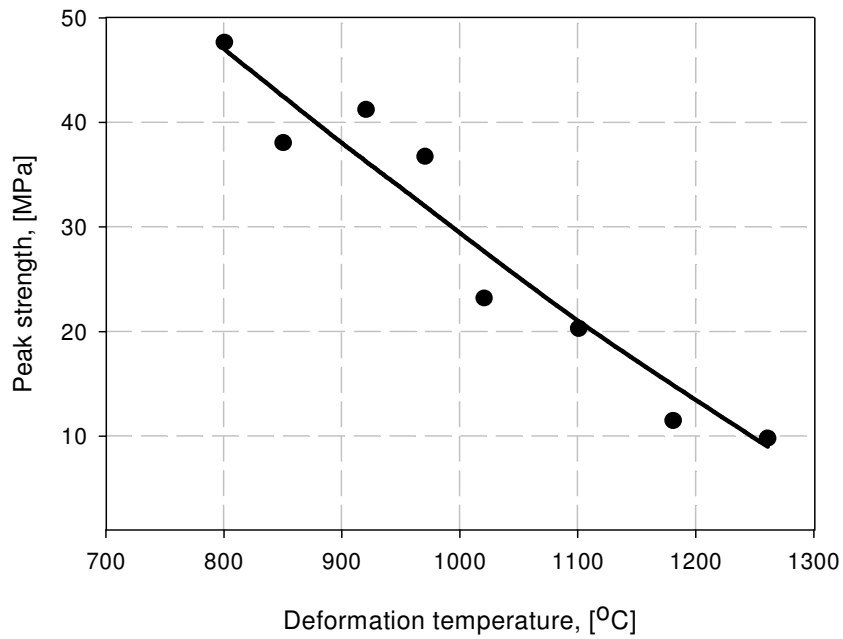

Figure 5.18 - The peak strength variation with temperature for 3CR12 (heat 3412423)

University of Pretoria – Siyasiya C. W. (2004)
Results and Discussion
_____

5.10 Resistance bending moment provided by the solidification shell

Side wall (narrow face) bulging will now be considered as a consequence of a balance between the applied ferrostatic force from the column of the liquid steel exerting a pressure on the side wall of the strand (expressed as the applied bending moment M_A) and the resistance bending moment M_R offered by the strength of the solidification shell. This implies that side wall bulging takes place when the resistance bending moment M_R is less than the applied bending moment M_A.

For this study, the solidification shell growth with respect to time (strand position), has been adopted from the modelled solidus profile obtained from the proprietary software program that is used at Columbus Stainless, figure 2.2 (b) in section 2.2.

To begin with, the following assumptions have been made:

- The ferrostatic pressure exerts a uniformly distributed load on the side walls of the solidifying shell and, therefore, in essence, the unconstrained narrow sides behave like a beam. This is evident from the flat ends of the side bulge i.e. the side bulge profile in figure 2.7 in section 2.4.
- The microstructure is homogeneous across the shell thickness at any given temperature.
- The cyclic compressive and tensile strains in the wider face do not affect the strain in the narrow face.
- The uni-axial yield stress (in this case the steady state flow stress) is considered as the yield criterion in analysing the bulging bending moment. The von Mises' yield criterion for a bi-axial stress condition can be equated to the uni-axial yield strength with at most a deviation from the former of 15.5 per cent. Furthermore, the longitudinal stress in the casting direction of the strand (due to its own mass) is minimised by the supporting rolls and, therefore, a transverse stress due to ferrostatic force is the main cause of side bulging.
- The elastic strain at high temperature is negligible and that creep deformation is governed by the universal hot working equation (equation 5.3 below).

The plastic bending moment M_p, is given by:

$$M_p = \sigma_y Z_p \quad (Nm) \qquad\qquad (5.3)$$

University of Pretoria – Siyasiya C. W. (2004)
Results and Discussion

---

where σ_y is the yield strength and Z_p is the plastic section modulus and for a rectangular section it is given by:

$$Z_p = \left[\frac{bt^2}{4} \right] \quad (m^3) \qquad\qquad (5.4)$$

where t is the solidification shell thickness and b is the length along the strand's casting direction which in this case, is taken as unit length.

Therefore, the resistance bending moment offered by the solidification shell strength, would be given by:

$$M_R = \left[\frac{b\sigma_y t^2}{4} \right] \qquad\qquad (5.5)$$

Since at high temperatures the elastic behaviour of steel diminishes and, therefore, it tends to flow, the flow stress may be used instead of the yield stress, in equation 5.5. The values for the steady state flow stresses at any given temperature were obtained from figure 5.18 and the resistance bending moment M_R has been computed using equation 5.5. Figure 5.19 shows the modelled (for the values of t from the plant's proprietary model) and schematic resistance bending moments M_R for thinner and thicker thicknesses of the solidification shell.
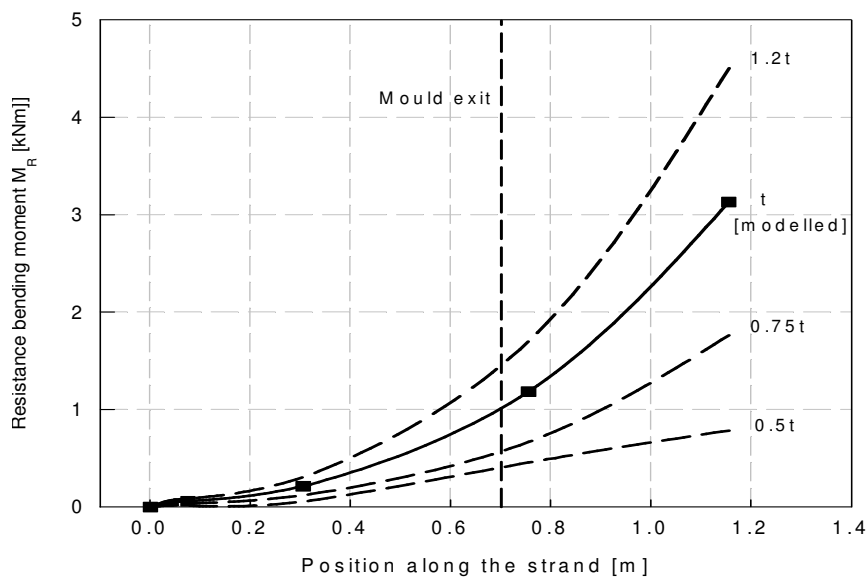

Figure 5.19 - The shell resistance bending moment M_R for the modelled shell thickness curve (solid line) and the schematic thinner and thicker shell thicknesses of t (dashed line).

Results and Discussion
_____

The shell strength increases almost exponentially with the decrease in temperature and increase in shell thickness as the strand moves downwards and is cooled down. This may be seen partly from equation 5.5 above that shows that the resistance bending moment M_R increases with the increase in the square of the solidification shell thickness. Furthermore, as the temperature decreases, there is more δ-ferrite that transforms to austenite and austenite has been proven to be stronger than δ-ferrite in this work, figure 5.22 below and supported by an observation of other workers[30,33].

The strain on the side walls may also be considered bi-axial because the strand is constrained on the top and bottom faces of the strand. A second stress may, therefore, arise in the solidification shell in the strand's casting direction from a longitudinal force exerted by the full column of liquid on the strand at its full point of solidification as well as from the gravitational force exerted by the vertical component of the strand. These forces are, however off-set by the frictional forces from the rollers that support the strand. Therefore, the von Mises' yield criterion for a bi-axial stress condition in the shell that exerts bulging force may have to be considered in a fundamental analysis. However, the longitudinal force is limited to less than 15.5% maximum of the ferrostatic force and, therefore, has been neglected (see figure 2.6A in appendix 2). The uni-axial yield stress (in this case the flow stress) is, therefore, considered as the yield criterion in analysing the bulging bending moment without significantly affecting the results of the analysis, as analysed in appendix 2.

5.11 Applied bending moment M_A due to ferrostatic pressure
The data for the ferrostatic head from which the ferrostatic pressure was calculated, was obtained from the geometry of the continuous caster. The calculations for the applied ferrostatic plastic bending moment M_A are also included in appendix 2. Figure 5.20 below shows how the ferrostatic pressure and the applied bending moment M_A it introduces on the solidification shell vary with position (or time). As expected, the ferrostatic pressure is zero at the meniscus and reaches a maximum value just before the strand fully solidifies. The ferrostatic bending moment increases with the ferrostatic head and decreases with the decrease in the length ab (figure 2.3A) as solidification progresses due to the increase in thickness t. As a result, the plastic bending
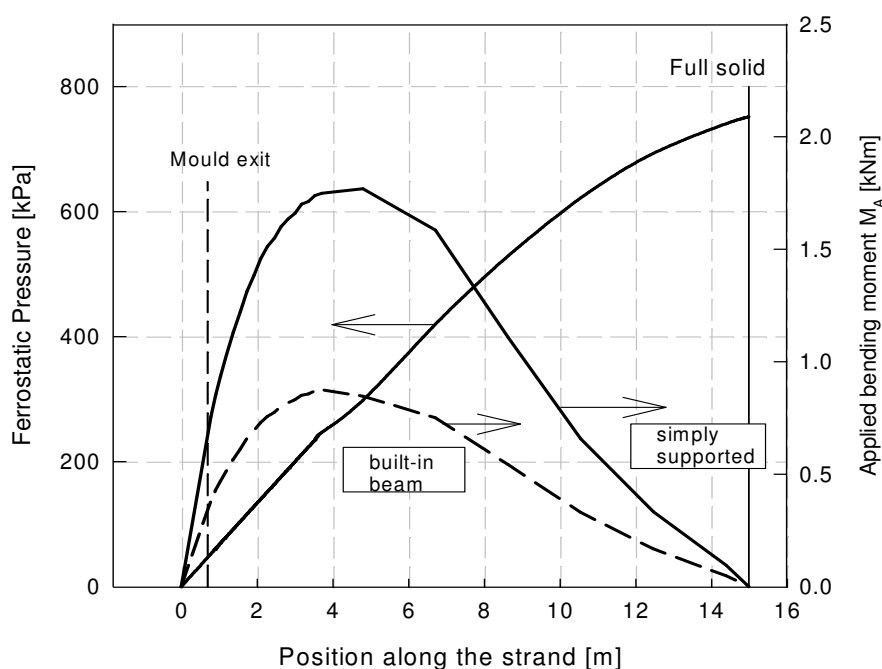
University of Pretoria – Siyasiya C. W. (2004)
Results and Discussion

_____

Figure 5.20 - Variation of ferrostatic pressure and the applied bending moment M_A with position along the strand for the built-in beam model (dashed line) and simply supported beam (solid line). The zero position equals the meniscus of the liquid steel in the mould.

moment reaches a maximum value after which it regresses to zero as the surface area on which it acts diminishes to zero too when the strand is completely solid. There are two curves, one for the simply supported beam model (in a solid line) and the other one for the built-in beam model (dashed line). A detailed analysis of the plastic bending moment due to ferrostatic pressure as a function of the head as well as the solidification shell thickness is given in appendix 2.

5.12 Plastic bending of the side walls (side bulging)

The resistance bending moment M_R and the applied bending moment M_A are plotted against the position of the strand for different values of shell thicknesses t in figure 5.21 below. As may be seen, the strand may be vulnerable to side bulging when the resistance bending moment M_R is almost the same or less than the applied moment M_A, i.e. $M_R \leq M_A$. Figure 5.21 (c) shows that a thicker solidification shell would be favourable for the prevention of the side wall bulging problem. Knowing that 3CR12 has good hot ductility characteristics,

University of Pretoria – Siyasiya C. W. (2004)
Results and Discussion

_____

careful implementation of a faster cooling rate could be done without necessarily risking a transverse cracking problem.

One of the assumptions that were made in this analysis was that the phase distribution of δ-ferrite and austenite was uniform across the solidification shell thickness. This is not true because there is a temperature gradient between the outer and inner faces of the solidification shell, the inner face being close to the liquidus. As expected, the inner region of the solidification shell would be fully δ-ferrite while the outer region δ-ferrite plus austenite. This implies that the experimentally determined shell strength could be more than the actual solidification shell strength during continuous casting.

University of Pretoria – Siyasiya C. W. (2004)
Results and Discussion

_____
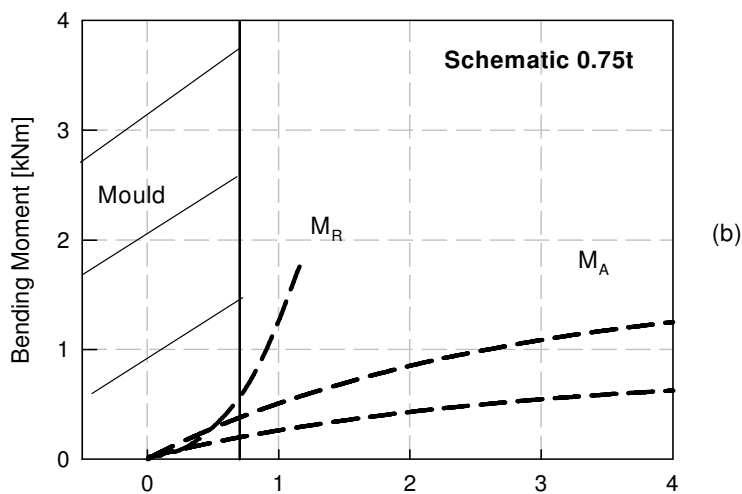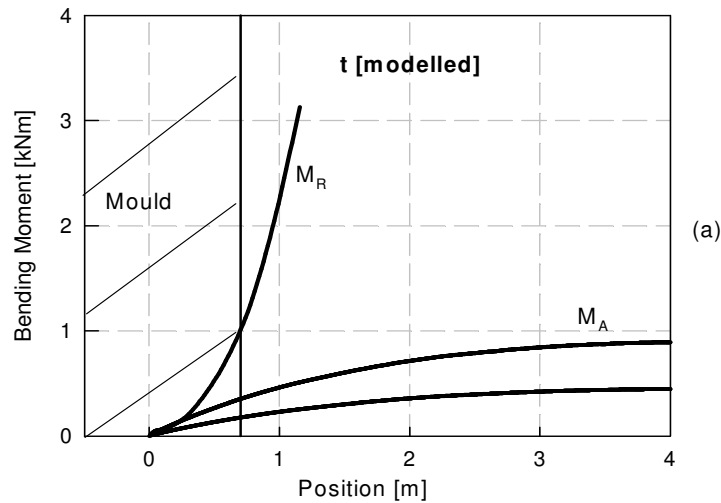
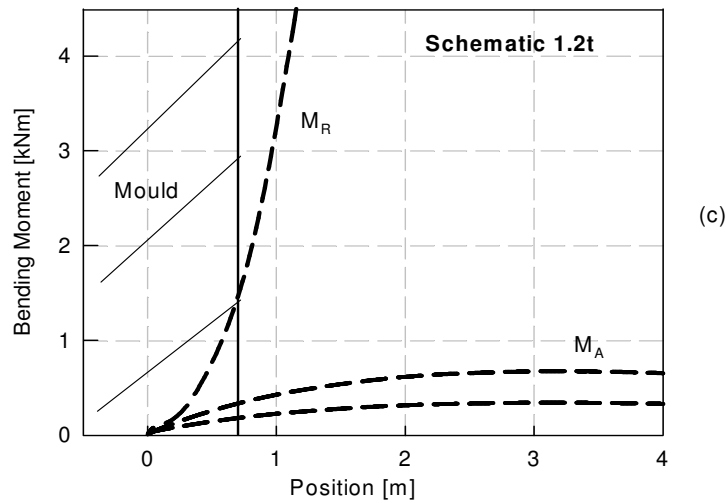Figure 5.21 - Variation of the resistance bending moment M_R and the applied bending moment M_A with the position of the strand during continuous casting of 3CR12, (a) curves using the plant model for shell thickness, (b) and (c) are schematic diagrams for a thinner and a thicker shell respectively

The observation that side wall bulging often takes place more on one side than on the other suggests that the heat extraction from the strand's thickness sides is not uniform. Since during secondary cooling water is sprayed onto the wider faces of the strand and not onto the thickness sides, the uneven heat extraction might be taking place in the mould such that by the time the strand emerges from the mould the shell on the side with more effective heat extraction is already thicker than the other one. Many studies in the past[38,39,40] have related the side bulging effect to the interaction of the strand and the mould vis-à-vis heat transfer during continuous casting. Therefore, part of the solution to the problem bulging lies on the study of the optimisation of the mould flux properties, casting speed, mould taper angle, chemical composition of the steel among other factors.

5.13 Comparison of hot strength of 3CR12 with an austenitic AISI 316

From the above model, a question needs to be addressed why side bulging is generally not found in austenitic stainless steels at Columbus Stainless. For this, firstly, a comparison needs to be made between the hot strength of 3CR12 under continuous casting conditions

University of Pretoria – Siyasiya C. W. (2004)
Results and Discussion

_____

with typically an AISI 316 stainless steel, also from Columbus Stainless. Figure 5.22 shows a comparison of the hot strength for the fully ferritic 3CR12 with an austenitic AISI 316 steel at 1260 ˚C. This gives a reflection of the high temperature strength advantage that austenitic steels have over ferritic steels during continuous casting. In this case, at 1260 ˚C, the hot strength of the 316 austenitic steel is almost twice that of 3CR12 in its fully δ-ferritic condition. This is in agreement with other studies[15,33] that have shown that an austenitic solidification shell is generally stronger than a ferritic one and that side wall bulging is, therefore, generally absent in austenitic stainless steels. This suggests that additions of austenite formers, within the chemical composition specifications of 3CR12, should be favourable for the reduction of side bulging as this would increase the austenite to δ-ferrite ratio in the dual phase region.

The results in figure 5.22 need to be interpreted with the knowledge of the influence of strain rate on the flow stress in different materials as the strain rate used here differs somewhat
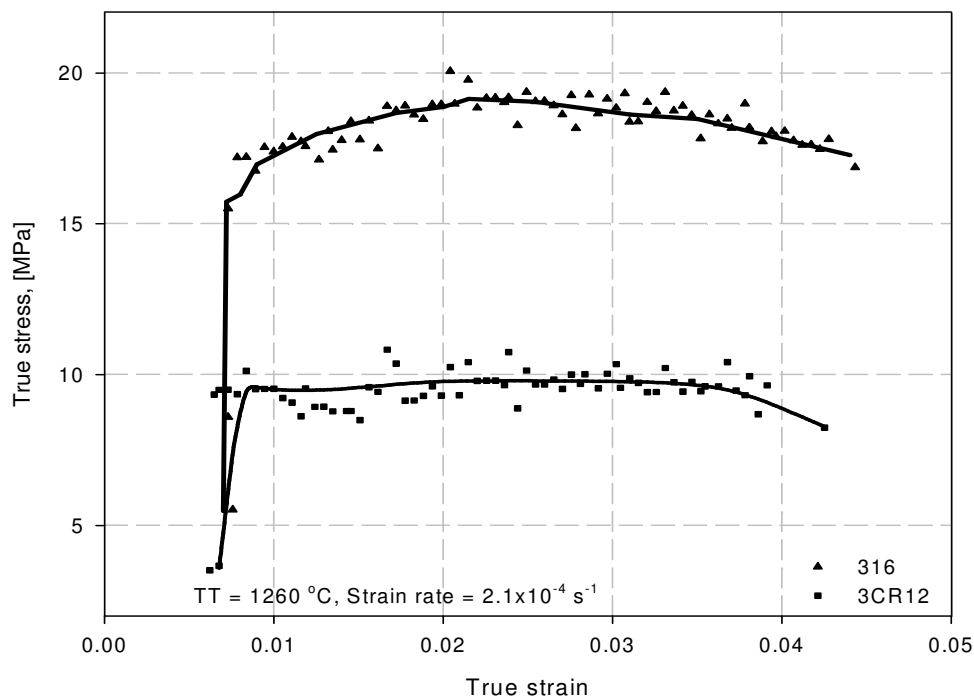

Figure 5.22 - The hot strength of fully ferritic 3CR12 compared to that of AISI 316 austenitic stainless steel, both deformed at 1260 ˚C at a strain rate of 2.1 x10^{-4} s^{-1}.

University of Pretoria – Siyasiya C. W. (2004)
Results and Discussion

_____

from the expected "bulging strain rate" in the plant, 2.1 x10^{-4} s^{-1} and 1.68 x10^{-4} s^{-1} respectively. Therefore, the constitutive hot working constants for 316 and 409C (a ferritic steel similar in chemical composition to 3CR12, table 5.3 below) are given in table 5.2 below[31]. Since all the constitutive constants for the relationship between strain rate, temperature and stress are known for both materials, the steady state flow stress σ_{ss} (MPa) at any test temperature T (K) can be predicted and thereafter compared with the experimental results. The relationship between strain rate, temperature and the steady state flow stress is given by the universal hot working equation 5.3 below[35,36]:

Parameter \ Alloy	n	Q (kJ mol^{-1})	β (MPa^{-1})	A
316C	4.5	402	0.012	3.31x10^{13}
409C	4.27	270	0.0254	$10^{11.2}$

Table 5.2 - The constitutive hot working constants for as-cast 316 and 409 steels

Alloy	C	Mn	Si	Cr	Mo	Ni	N	Ti
409C	0.06	0.49	0.36	10.96	0.01	0.16	0.0007	0.19
3CR12	0.014	0.65	0.65	11.28	0.013	0.4	0.015	0.03

Table 5.3 - Comparison of 3CR12 (used in this study) and typical 409 ferritic steels

$$A\left(\sinh \beta \sigma_{ss}\right)^{n} = \dot{\varepsilon}\exp\left(Q/RT\right) = Z \qquad (5.3)$$

where Q is the activation energy for hot working, R is the universal gas constant which is 8.31 J mol^{-1} K^{-1}, n is the stress sensitivity, T is the temperature in Kelvin, β (MPa^{-1}) is the stress multiplier, Z is the Zener Holloman parameter and A is a material constant.

Therefore, at 1260 °C and at an applied strain rate of 2.1 x10^{-4} s^{-1}, the predicted steady state flow stresses for the AISI 316 and 409C are 17.0 and 13.0 MPa respectively whereas that of 3CR12 has been measured as 10 MPa, figure 5.21. This prediction of the steady state flow

University of Pretoria – Siyasiya C. W. (2004)
Results and Discussion

_____

stress of 409C is within the range of the experimental results given in figure 5.22, considering that the chemical composition of 3CR12 and 409C differ. The predicted higher flow stress for 409C (by 3 MPa) could be attributed to the higher quantities of titanium and carbon. Although the predicted flow stress for 409C is slightly higher than the measured flow stress for 3CR12, this can still serve as a guide that the strain rate might not have significantly affected the steady state flow stresses of the two steels compared in figure 5.22.

Chapter 6

Conclusion

_____

The primary objective of this study was to enhance the understanding of the high temperature metallurgical behaviour of 3CR12 during continuous casting and possibly shed some light on its impact on the common side bulging and width variation problem. The following conclusions can be made from this study:

6.1   The casting conditions in the mould are crucial to ensure that the solidification shell is thick enough to withstand the ferrostatic pressure exerted on the unconstrained narrow sides of the strand as it exits from the mould. Therefore, part of the solution lies in the study of the optimisation of the cooling rate, mould flux properties, casting speed, mould taper angle, chemical composition of this steel among other factors.

6.2   3CR12 has good hot ductility in the strand straightening temperature range and this is attributed to the high volume fraction of ferrite that exhibits excellent hot ductility behaviour. In view of this observation, a careful implementation of a "harder cooling rate" for a thicker and, therefore, stronger solidification shell at the exit from the mould would minimise side bulging.

6.3   Austenite formers (C, N, Ni and Mn) raise the δ-ferrite to austenite transformation start temperature A_{r5} and shift it to earlier transformation start times. Therefore, additions of austenite formers within the 3CR12 specification range would be favourable for a stronger solidification shell since austenite exhibits better hot strength properties than δ-ferrite.

6.4   As long as the δ-ferrite to austenite ratio keeps fluctuating due to variations in chemical composition and cooling rate in the dual phase region from cast to cast, the strand width variation problem will probably persist. This is simply because of the effect these have on the phase ratios between ferrite and austenite through the lattice structure differences. Ferrite being less dense than austenite, occupies more volume than austenite, thereby affecting the slab width.

University of Pretoria – Siyasiya C. W. (2004)
Conclusion
_____

6.5   Hot deformation appears not to affect the kinetics of either the δ-ferrite to austenite phase transformation or the regression of austenite to α-ferrite under continuous casting conditions of 3CR12 and the transformation kinetics in the undeformed state may be applied with confidence to the strand during unbending.

6.6   At faster cooling rates greater than 60 ˚C/min, the δ-ferrite to austenite transformation start temperature during continuous cooling A_{r5} is sensitive to the cooling rate, i.e. the undercooling increases with an increase in cooling rate.

University of Pretoria – Siyasiya C. W. (2004)
References
_____

1.   BAKER, H. (ed.) Alloy Phase Diagrams Volume 3, ASM Handbook, (1992) pp. 1.26.

2   HONEYCOMBE, R. W. K. and BHADESHIA, H. K. D. H., "Steels Microstructure and Properties", 2nd Edition, Edward Arnold, (1995), pp. 252.

3.   Technical Specification Manual, Columbus Stainless, August 1997, pp. 3.1.

4.   HEWITT, J., "High-chromium controlled-hardenability steels" INFACON 6. Proceedings of the 1st International Chromium Steels and Alloys Congress, Cape Town, Vol. 2, Johannesburg, SAIMM, 1992, pp. 71-88.

5.   BALL, A., CHAUHAN, Y., SCHAFFER, G.B. "Microstructure, phase equilibria, and transformations in corrosion resistant dual phase steel designated 3CR12". Materials Science and Technology, Volume 3 (1987), pp 189-196.

6.   PISTORIUS, P.G.H., DE KLERK, H.J., AND VAN ROOYEN G. T. "The austenite-ferrite transformation in 11.5 per cent chromium steels". Proceedings of the 6th International Chromium Steel and Alloy Congress, Cape Town. Vol. 2. Johannesburg, SAIMM, (1992), pp.65-70.

7.   KNUTSEN, R., "Influence of compositional banding on grain anisotropy in 3CR12 steel", Materials Science and Technology, Volume 7, (1992), pp. 621-627.

8.   JUNGBACKE, N., MSc Thesis, University of Cape Town, 1996.

9.   PROZZI, J.M., MSc Thesis, University of Pretoria, 1995.

10.   COCKETT, C. D., and DAVIS, J., J. Iron Steel Inst. Vol. 201, (1963), pp. 110

11.   ONINK, M., BRAKMAN, C.M., TICHELAAR, F.D., MITTEMEIJER, E.J., SWAAG, S., Metallurgica et Materialia, Volume 29, (1993), pp. 1011.

12.   BENJAMIN, B. (ed.), Properties and Selection: Stainless Steels, Tool Steels and Special-Purpose Metals, ASM Metals Handbook Ninth Edition, (1980), Vol.3 pp. 34.

13.   BĖRANGER, G., HENRY, G., and SANZ, G., (Editors) "The Book of Steel" 1996, pp. 93.

14.   OKIMORI, M., FUKUDA, Y., TANAKA, S., HOJO, M., and NAKANO, T., "Improvement of Surface Quality of Austenitic Stainless Steel", Nippon Steel Technical Report No. 87 January 2003. pp. 62-66.

15.   RAY, S. K., MUKHOPSDHYAY, B., DAS, P. C., "Effect of chemistry on solidification and quality of stainless steel", Annual Tech. Mtg. of India Inst. Metals, Jamshedpur, pp. 14-17 Nov. 1999.

University of Pretoria – Siyasiya C. W. (2004)
References

_____

16.   LUBAHN, J. D., and SACHS, G., Transactions ASME, Vol. 72, (1950), pp. 201-208.

17.   MINTZ, B. and ARROWSMITH, J. M., Metal Technology, 1979, Vol. 6, pp. 24.

18.   CARDOSO, G. I. S. L., MINTZ, B. and YUE, S., "Hot ductility of aluminium and titanium containing steels with and without cyclic temperature oscillations", Ironmaking and Steelmaking, 1995, Vol. 22, No. 5, pp. 365-377.

19.   SUZUKI, H. G., NISHIMURA, S., INAMURA, J. AND NAKAMURA, Y. Transaction Iron Steel Institute, Japan, Vol. 24, (1984), pp. 169.

20.   MINTZ, B., SHAKER, M. and CROWTHER, D.N., "Hot ductility of an austenitic and a ferritic stainless steel", Materials Science and Technology, Vol. 13 (1997), pp. 243-249.

21.   COMINELI, O., ABUSHOSHA, R., MINTZ, B., "Influence of titanium and nitrogen on hot ductility of C-Mn-Nb-Al steels", Materials Science and Technology, Vol. 15 (1999), pp. 1058-1068.

22.   MINTZ, B., COWLEY, A., ABUSHOSHA, R., "Importance of columnar grains in dictating hot ductility of steels", Materials Science and Technology, Vol. 16 (2000), pp. 1-5.

23.   MAEHARA, Y., YASUMOTO, K., SUGITANI, Y AND GUNJI, K., "Effect of carbon on hot ductility of as-cast low alloy steel", Transaction Iron Steel Institute, Japan, Vol. 25, (1985), pp. 1o45-1051.

24.   DEMO, J.J., "Structure, constitution, and general characteristics of wrought ferritic stainless steels". Source book on the ferritic stainless steels, LULA, R.A., (ed.). Metals Park, Ohio, American Society for Metals, (1986).

25.   MILLS, K. C., "A Review of ECSC-funded project on mould powders. E (1990) publication EC Luxembourg.

26.   VAN NIEKERK, H., Columbus Stainless, Personal Communication.

27.   G'SELL, C. and JONAS J. J., Journal of Material Science, 1979, Vol. 14, pp. 583-591.

28.   ZAAYMAN, J. J.J., "Improvements to the toughness of the heat affected zone in welds of 11 to 12 per cent chromium steels", PhD Thesis, 1994.

29.   MINTZ, B. and JONAS, J. J., "Influence of strain rate on production of deformation induced ferrite and hot ductility of steels" Material Science and Technology, August 1994, Vol. 10, pp. 721-27.

University of Pretoria – Siyasiya C. W. (2004)
References

_____

30. MAZUMDAR, S. and RAY, K. S., "Solidification control in continuous casting of steel", Sadhana, Vol. 26, Parts 1 & 2, February-April 2001, pp. 179-198.

31. McQUEEN, H. J., and RYAN, N. D., "Constitutive analysis in hot working", Materials Science and Engineering A322 (2002), pp. 43-63.

32. VAN ROOYEN, G. T., University of Pretoria, Personal Communication,

33. RAY, S. K., MUKHOPADHYAY, B. and BHATTACHARYYA, S. K., "Prediction of crack-sensitivity of concast slabs of AISI-430 stainless steel. ISIJ, Vol. 36, (1996), pp. 611-612.

34. ROBERT, C. W., (ed.) CRC Handbook of Chemistry and Physics, 62nd Edition, 1981-1982, pp. B-244.

35. ZENER, C., and HOLLOMAN, J. H., Journal of Applied Physics, Vol. 15, (1944), pp. 22-32.

36. SELLARS C. M., and McG. TEGART, W. J., Mem. Sci. Rev. Metallurgy, Vol. 63, (1966), pp. 731.

37. KALTENHAUSER, R. H., Met. Eng. Q., May (1971), pp. 41-47.

38. SCHWERDTFEDER, K. J., "Heat Withdraw in Continuous casting of Steel" The AISE Steel Foundation, 2003, pp. 1- 41.

39. SCHREWE, H. F., "Continuous casting of steel" Verlag Stahleisen mbH, Dusseldorf, 1987

40. IRVING, W. R., and PERKINS A., "The Influence of Engineering Process and Chemical Factors on Surface and Internal Quality of Continuous Cast Slabs" , Int. Symposium, Durgapur, The Indian Institute of Metals, Oct. 1982, Paper 2.1.

University of Pretoria – Siyasiya C. W. (2004)
Appendix 1 **Strand width variation data from Columbus Stainless**
_____

Slab number	Minimum width [mm]	Maximum width [mm]	Maximum variation from 1210 mm	Ferrite Factor
3373791	1208.25	1218.48	+8.48	11.04
3373792	1209.23	1217.09	+7.09	11.04
3373793	1213.16	1218.07	+8.07	11.04
3373794	1210.65	1217.09	+7.09	11.04
3373795	1214.64	1226.92	+16.92	11.04
3373801	1224.95	1232.81	+22.81	11.71
3373802	1225.93	1232.32	+22.32	11.71
3373803	1225.34	1230.84	+20.84	11.71
3373804	1217.44	1271.83	+61.83	11.71
3373805	1219.22	1233.65	+23.65	11.71

Table 1.1A - Width variation of the slab measured at caster exit

University of Pretoria – Siyasiya C. W. (2004)
Appendix 2   Numerical Analysis of the Ferrostatic Plastic Bending Moment
_____

2.1 Plastic bending moment introduced by the ferrostatic pressure
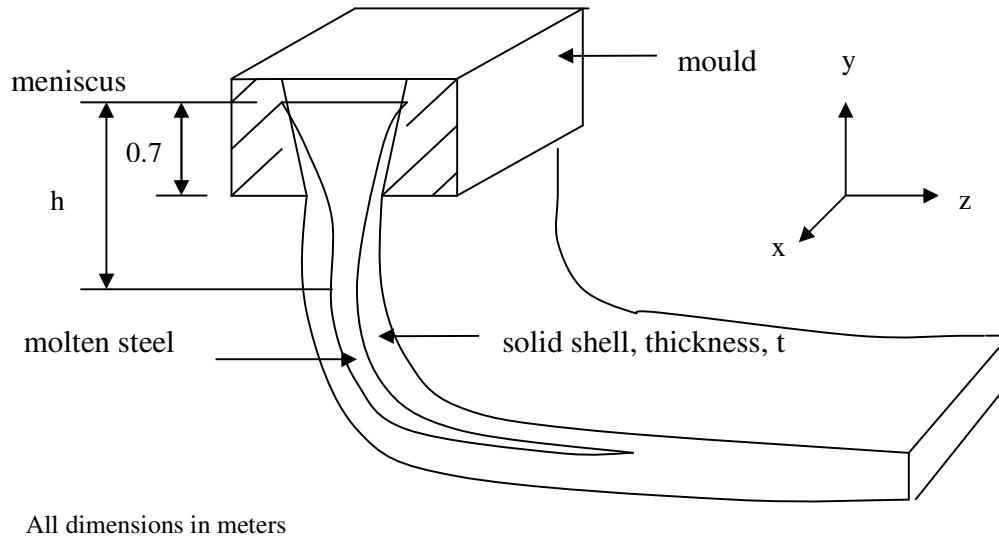

All dimensions in meters

Figure 2.1A - The schematic presentation of the bow-type caster

The ferrostatic pressure P is given by

$$P = g\rho h \quad (Pa) \qquad\qquad (1.1A)$$

where ρ is the density for the molten steel, in this case 6846 kgm^{-3} for 87%Fe and 11.5%Cr and the balance the other alloying elements, h is the ferrostatic head in meters and g is the acceleration due to gravity which is 9.81 ms^{-2}. The densities for liquid iron and chromium are 7015 and 6460 kgm^{-3} respectively[34].

A sketch of a half-section through the strand, perpendicular to the casting direction, is shown in figure 2.2A below. The strand is constrained by the guide rolls in the y-direction perpendicular to the casting direction and it is assumed that plain strain conditions prevail in the casting direction due to the huge down stream mass of the cast strand. Therefore, there is only one degree of freedom, i.e. in the x-direction.
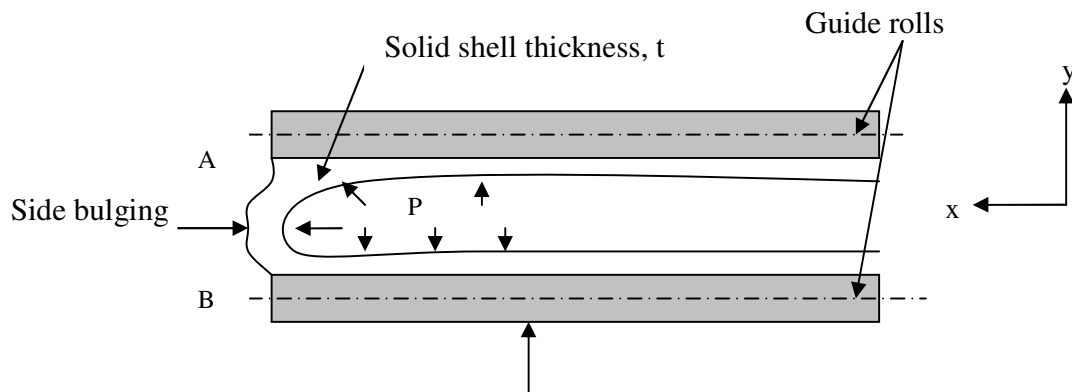
_____

Figure 2.2A - A schematic diagram of a half-section through the strand showing the bulging on the side wall of the strand

Since at high temperatures the elastic strain is much smaller than the plastic strain, it can be assumed that the beam AB undergoes full plastic strain. Therefore, from plastic bending theory, the plastic bending moment M_p is given by:

$$M_p = \sigma_y Z_p \quad (Nm) \qquad\qquad (1.2A)$$

where σ_y is the yield stress and Z_p is the plastic section modulus, and for a rectangular section

$$Z_p = \left[\frac{bt^2}{4}\right] \quad (m^3) \qquad\qquad (1.3A)$$

Consider a cross section of the solidification shell at temperature T, shell thickness t under pressure P, figure 1.3A below, then;

$$L = (0.2 - 2t) \quad (m) \qquad\qquad (1.4A)$$

University of Pretoria – Siyasiya C. W. (2004)
Appendix 2   Numerical Analysis of the Ferrostatic Plastic Bending Moment
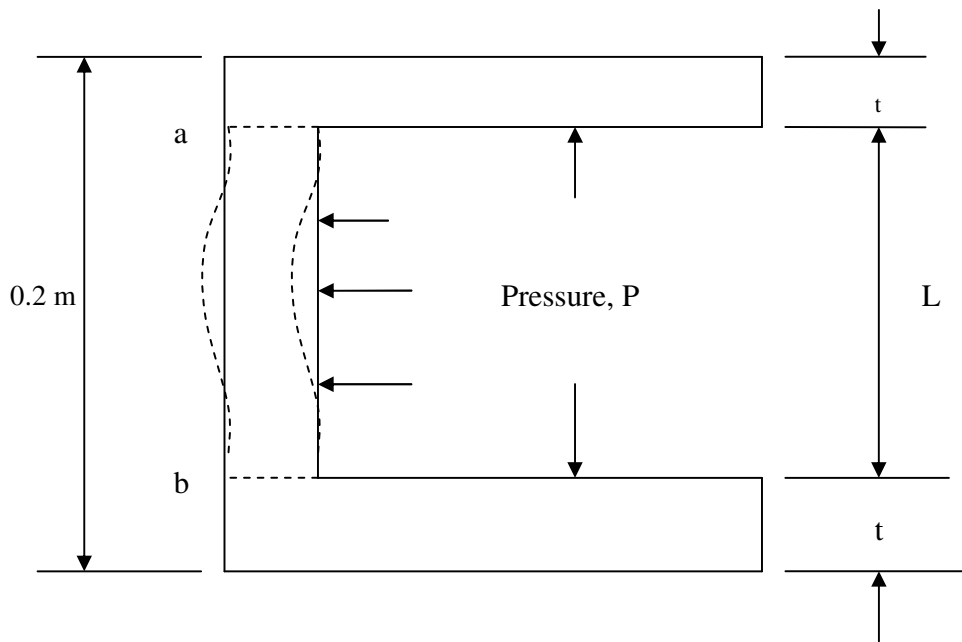
_____

Figure 2.3A - Schematic presentation of the cross section of the solidifying shell at one of the side walls with the side bulging in dotted lines

The portion ab of the solidification shell in figure 2.3A above can be treated as a simply supported beam when the solidification shell for the wider faces is thin and as a built-in beam when it is thick, i.e. able to fully constrain the ends of the perceived beam.

Figure 2.4A below shows a schematic illustration of the resistance bending moment M_R variation with position of the strand as the solidification shell grows to a full solid slab.

_____

M_R ← $\left[\dfrac{wL^2}{8}\right]$

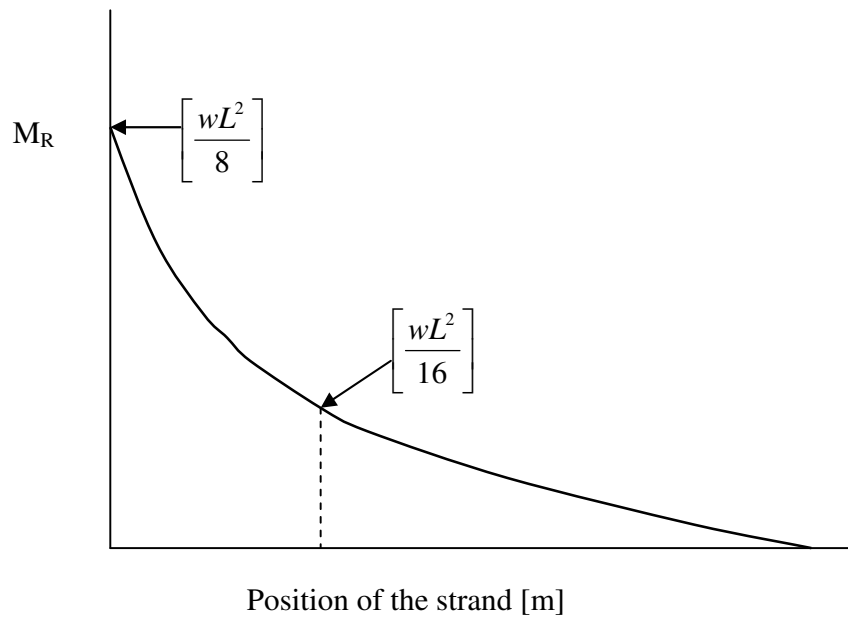$\left[\dfrac{wL^2}{16}\right]$

Position of the strand [m]

Figure 2.4A - Schematic presentation of the resistance bending moment as the solidification shell growth progresses

The plastic bending moments and stresses for both the simply supported and built-in beams are as tabulated in table 2.1A below.

	Simply supported	Built-in	Units
M_p	$\left[\dfrac{wL^2}{8}\right]$	$\left[\dfrac{wL^2}{16}\right]$	Nm
σ_y	$\left[\dfrac{wL^2}{2bt^2}\right]$	$\left[\dfrac{wL^2}{4bt^2}\right]$	Pa
Z_p (rectangular section)	$\left[\dfrac{bt^2}{4}\right]$	$\left[\dfrac{bt^2}{4}\right]$	m^3

Table 2.1A - The plastic bending formulas for the simply supported and built in beams

Since, in this case, the uniformly distributed load is the ferrostatic pressure, then the load per unit length w (Nm^{-1}) is substituted by the pressure P exerted on a unit length of the strand b.

University of Pretoria – Siyasiya C. W. (2004)
Appendix 2   **Numerical Analysis of the Ferrostatic Plastic Bending Moment**
_____

In order to compare the applied bending moment M_A (introduced by the ferrostatic pressure) to the resistance bending moment M_R (provided by the shell), the peak strength (steady state flow stress) of the 3CR12 has been multiplied by $\dfrac{bt^2}{4}$, where t is the solidification shell thickness.   The variables P, t and L (L = 0.2-2t) were obtained from the caster geometry and modelled shell thickness profile. Some data have been attached to this appendix.

2.2 The yield criterion

Applying plane strain conditions to the side walls of the strand, figure 2.1A above, $\varepsilon_y = 0, \varepsilon_z \neq 0, \varepsilon_x \neq 0; \sigma_y = 0, \sigma_z \neq 0, \sigma_x = P$. Hence, the side walls experience a bi-axial load due to the ferrostatic pressure P, refer to figure 2.3A above. However the longitudinal stress σ_z is expected to be minimal since the guide rolls support the strand. It must also be noted that this is a tensile stress and, therefore, the two principal stresses (σ_x and σ_z) can schematically be presented in a Mohr's circle as shown in figure 2.5A below.

The von Mises' yield criterion states that plastic yielding in a multi-axial stress system will take place when the right hand side of the equation 1.6A below is equal to the yield strength of the material σ_o under pure axial testing:

$$\sigma_o = \frac{1}{\sqrt{2}}\left[\left(\sigma_1 - \sigma_2\right)^2 + \left(\sigma_2 - \sigma_3\right)^2 + \left(\sigma_3 - \sigma_1\right)^2 \right]^{\frac{1}{2}} \qquad (1.6A)$$

The von Mises yield locus for a plain stress condition is given in figure 2.6A below. For a bi-axial stress system, the von Mises criterion predicts at most 15.5% yield strength higher than the uniaxial stress system. Therefore, the yield strength obtained from the uniaxial tensile test could be equated to the yield strength of a bi-axial stress system without significantly affecting the accuracy of the results.

University of Pretoria – Siyasiya C. W. (2004)

Appendix 2   Numerical Analysis of the Ferrostatic Plastic Bending Moment

_____
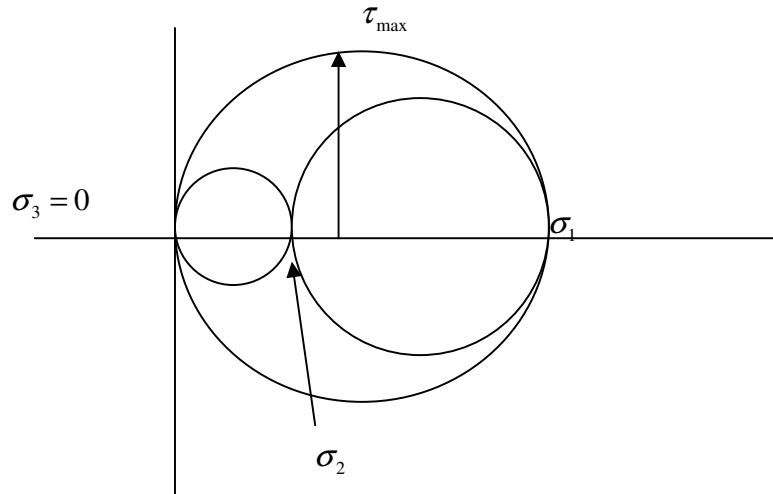
$\sigma_x = \sigma_1$ and $\sigma_z = \sigma_2$

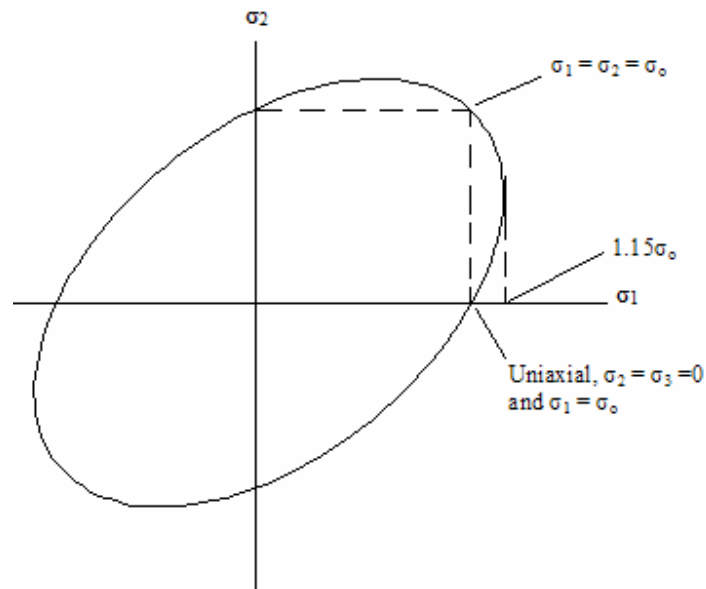Figure 2.5A - The Mohr's circle for multi-axial stress

Figure 2.6A - The von Mises yield locus for a plain stress condition

90

University of Pretoria – Siyasiya C. W. (2004)

Appendix 3   **Estimation of the strain rate during side bulging**
_____

The maximum side wall bulging that was measured on the as-cast slabs at room temperature was 7 mm. However, Columbus Stainless has encountered side wall bulging as high as 10 mm[26]. Based on the indication that side bulging probably takes place at high temperatures and within the first one to one and half meters from the mould exit (figure 5.21), it can be considered that this deformation takes place within 60 to 90 seconds after exiting the mould at an average casting speed of 1.01 m/s. Assuming a symmetrical side bulge as sketched in figure 3.1A:
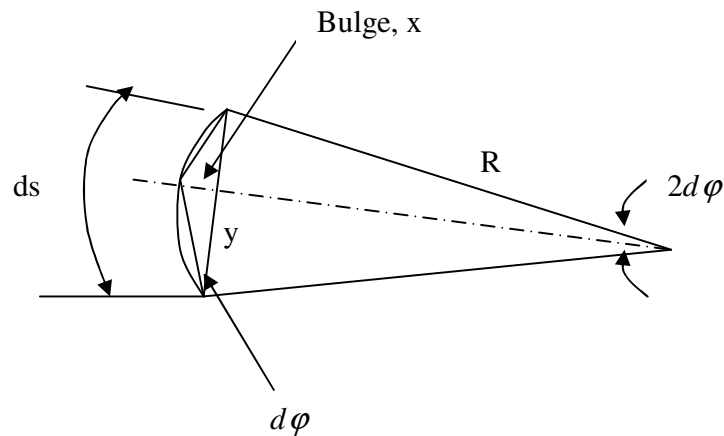

Figure 3.1A - Sketch for the geometry of the side bulging

For small angles in radians:

$$2\,d\varphi = \left(\frac{ds}{R}\right) \qquad (3.1A)$$

For a 200 mm thick slab, y = 100 mm and, therefore, the radius of the arc R would be given by:

$$R = \left[\frac{y}{\sin(d\varphi)}\right] \qquad (3.2A)$$

91

University of Pretoria – Siyasiya C. W. (2004)

Appendix 3   **Estimation of the strain rate during side bulging**

_____

$$x = y \tan(d\varphi) \qquad\qquad (3.3A)$$

Consider the worst bulge of 10 mm i.e. x = 10 mm, then:

$$R = \left[\frac{100}{\sin 5.7^{\circ}} \right] = 1004 mm \qquad\qquad (3.4A)$$

The strain $\quad e = {x}\!/\!{R} = {10}\!/\!{1004} = 0.00996 \qquad\qquad (3.5A)$

If the side bulging takes place within 1 m from mould exit, at an average casting speed of 1.01 m/s then the strain rate becomes:

$$\dot{e} = {0.00996}\!/\!{59.4} = 1.68 \times 10^{-4} \text{s}^{-1} \qquad\qquad (3.6A)$$